2013

Optimization of Donor-Acceptor Substitution for Large Optical Non-linearities in Small Organic Molecules

Marten Beels
Lehigh University

Optimization of Donor-Acceptor Substitution for Large Optical Non-linearities in Small Organic Molecules

by

Marten Beels

A Dissertation
Presented to the Graduate Committee
of Lehigh University
in Candidacy for the Degree of
Doctor of Philosophy
in
Physics

Lehigh University
September 2013

Approved and recommended for acceptance as a dissertation in partial fulfillment of the requirements for the degree of Doctor of Philosophy.

Marten Beels
Optimization of Donor-Acceptor Substitution for Large Optical Non-linearities in Small Organic Molecules

---

Date

Ivan Biaggio, Dissertation Director, Chair

Accepted Date

Committee Members

Dr. Michael Stavola

Dr. Slava Rotkin

Dr. Filbert Bartoli

Dr. Gregory Ferguson

For Becca, who continuously reminded me of the things that were truly important.
We make quite a team.

Contents

List of Tables

List of Figures

Abstract

The determination of the wavelength dependence of the complex third-order polarizability of organic molecules delivers information on the mechanisms of resonance enhancement and allows for comparison of the two-photon absorption cross sections on their peak to the off-resonant third-order polarizabilities. The experimental technique of degenerate four-wave mixing offers several advantages over other comparable techniques, including sensitivity, background-free signal, automatization, and information on excited state lifetimes. This work uses experimental data, computational chemistry, and analysis of the relevant terms in the sum-over-states quantum mechanics expression to analyze the significant contributions to the third-order polarizability, mechanisms of resonance enhancement, and comparison of the off resonant values, to peak resonant values. This information provides insight into the structure-property relationships for the third-order polarizability, allows for comparison to fundamental limits, and assessment of the potential for molecules to form solid state materials with a large third-order susceptibility.

The use of donor-acceptor (D/A) substitution allows for the realization of small molecules with large third-order polarizabilities. However, in contrast to symmetric non-D/A oligomers that have third-order polarizabilities which scale by a power law as the molecule is made larger, D/A substituted molecules only scale up to a certain length, beyond which the molecule is over-extended and the third-order polarizability does not increase further. This work will analyze the scaling of non-D/A and D/A substituted molecules, determine the optimum length for D/A substituted molecules, and explain the physics of the saturation.

Chapter 1

Introduction

The physics of light and matter interaction include an extremely wide range of observable effects, relevant to many aspects of physics beyond optics. This interaction can be extremely strong (total absorption, for example) or very weak (refraction). It is also possible to classify light and matter interaction over a range of energies, from low-energy phenomena like the photoelectric effect, to very high-energy phenomena like pair production (nuclear physics). In these examples, energy is conserved and transferred between light and matter, resulting in the annihilation, modification, or creation of light (or even the creation of matter!).

The relatively modern field of non-linear optics is concerned with the higher order effects possible with light in the presence of a non-linear material. This means that *light-light* interaction is possible. Many new possibilities exist for interesting physics, useful devices, and novel experimental techniques. Non-linear optics allows for exotic imaging methods useful for a wide range of applications, from the microscopy of live biological cells, to explosion dynamics. Useful devices for applications like optical limiting, "optical transistors", optical data storage, and even some cancer therapies [5] work on the principles of non-linear optics.

As a non-linear medium, organic molecules provide a flexible basis for the investigation and realization of these physical effects and devices. Their structure and chemistry can be engineered by skillful chemists to realize novel molecules, or tweak existing ones. This approach allows for the development of materials suitable

for applications, as well as systematic variations to better study the influence of molecular parameters on the non-linear optical properties.

The molecular origins of the non-linear response are well understood, however there is much to be learned on the subject of optimizing the structure of molecules for the best non-linear response. As a relative figure of merit (FOM) we use several metrics to assess how well a particular molecule performs. The two most common metrics published in the literature so far provide a measure of a molecule's off-resonant third order polarizability *per size of molecule* ($\tilde{\gamma}$), and with respect to it's *fundamental limit* (γ_I). The former reflects a molecule's potential to form solid state materials with a large third order susceptibility, and the latter indicates how efficient the molecular design is, given a number of polarizable π-electrons, and first excited-state transition energy.

This work introduces two additional metrics, the specific $\tilde{\gamma}^{\text{res}}$ and intrinsic γ_I^{res} for the imaginary part of the third-order polarizability on resonance. Because it is related to the two-photon absorption (TPA) cross section, these metrics provide a measure of the molecule's potential to form solid state materials suitable for devices such as optical limiting, and a similar measure of how efficient the molecular parameters are chosen for such an application.

This thesis will present studies into the non-linear spectroscopy of small organic molecules, using systematic variations in the structure to study their effect on the non-linear optical response, relating these properties to fundamental limits, and assessing the potential for devices suitable for applications.

The use of these molecules in applications requires assembling them into the solid state. We choose to study the third-order polarizability of molecules in solution for experimental convience in order to control the number density, but it has been shown that the third-order polarizability is a good predictor of the third-order susceptibility of the solid-state. In fact, we can calculate the third-order susceptibility of the solid-state from the molecular third-order polarizability using a gas model, and it works [6].

The determination of the wavelength dependence of the complex third-order polarizability of organic molecules delivers information on the mechanisms of resonance

enhancement and allows one to compare the two-photon absorption cross sections on their peak to the off-resonant third-order polarizabilities. Computational chemistry and an analysis of the quantum mechanical sum-over-states (SoS) expression provide additional support to the experimental data.

Chapter 2

Non-Linear Optics

The physics of non-linear light and matter interaction can be explained via several analogies, or with the development of different physical descriptions. Fundamentally, the most correct is the quantum explanation, but to reduce the level of abstraction, some classical analogs are still useful in their descriptive ability, to help illuminate the physical processes in terms that are more relatable to our common experiences.

2.1 Polarization

For the purposes of this chapter, and within the scope of non-linear optics, the mechanism by which light and matter interact can be stated as the perturbation of the equilibrium positions of the constituent charged particles that make up matter. Because light (in the same reference frame as the material) consists of both an electric field and a magnetic field, and matter contains atoms with positively charged nuclei and negatively charged electrons, the electric field will exert a force on the nuclei and electrons. The light is an electromagnetic wave at some frequency ω so the system can be described as a driven oscillator. A special case exists at zero frequency in which there need not be a magnetic field, but a constant electric field still applies a constant force to the charged particles.

The quantum description is similar, except the atoms have discrete energy levels, and the incident light contains photons at a certain energy, so it is necessary to

consider a certain level of interaction with all possible states. Therefore there is a sum over all accessible states to take into account all possible paths in which a system can develop in time. This is the sum-over-states (SoS) approach.

When a bound charge q is displaced from its equilibrium position a distance d, a dipole $p = qd$ is induced. In the macroscopic definition, the polarization of a medium of bound charges is defined as a dipole density, in units of dipole moment per unit volume.

The relationship between an externally applied electric field and the polarization induced in matter is given by the susceptibility χ, which is a measure of how polarizable a material is,

$$\vec{P} = \epsilon_0 \chi \vec{E}, \tag{2.1}$$

where $\vec{E}$ is the electric field, $\vec{P}$ is the polarization, ϵ_0 is the permittivity of free space, defined to be $\epsilon_0 = 8.85 \times 10^{-12}$ with units of $\mathrm{CV^{-1}m^{-1}}$ in the SI system. The susceptibility (χ) is unitless in the linear case. Multiplying the units of ϵ_0 by the units of the electric field ($\mathrm{Vm^{-1}}$) gives $\mathrm{Cm^{-2}}$ which is equal to the units of dipole per unit volume (Cm / $\mathrm{m^3}$).

In a polarizable medium, the response is generally not instantaneous, and depends on the frequency of the electric field. For this reason, χ is a complex valued function of the applied frequency. In a causal system, the polarization at some point in time depends only on the electric fields applied up to that point in time, and Kramers-Kronig relations hold.

In general, the polarization of a material does not consist of only the linear response, so it can be described as a power series of the field strength.

$$\vec{P} = \vec{P}^{(0)} + \epsilon_0 \vec{\chi}^{(1)} \otimes \vec{E} + \epsilon_0 \vec{\vec{\chi}}^{(2)} \otimes \vec{E} \otimes \vec{E} + \epsilon_0 \vec{\vec{\vec{\chi}}}^{(3)} \otimes \vec{E} \otimes \vec{E} \otimes \vec{E} \tag{2.2}$$

where $\vec{P}$ is the total macroscopic polarization that can be expressed as a sum of contributions, $\vec{P}^{(0)}$ is a permanent polarization that may be present in some materials, $\vec{E}$ is the electric field, and $\chi^{(n)}$ is the n^{th} order nonlinear susceptibility, which is a $(n+1)^{\text{th}}$ rank tensor.

2.2 Linear Optics

In a harmonic potential, the solution to a driven, damped harmonic oscillator is a good description of the linear susceptibility ($\chi^{(1)}$). The motion of the negatively charged electrons around their equilibrium can be described by the differential equation

$$-eE(t) - \xi\dot{x} = m\ddot{x}, \tag{2.3}$$

where e is the charge of the electron, $E(t)$ is the time-varying electric field, ξ is the damping term, m is the mass of the electron, and $\dot{x}$ and $\ddot{x}$ represent the first and second time derivatives of the coordinate of the electron, respectively. If we assume a sinusoidal time dependence for the electric field at a frequency ω so that $E(t) = E_0 e^{-i\omega t}$, and therefore a sinusoidal time dependence for the response also at the same frequency ω, ($x(t) = x_0 e^{-i\omega t}$), then this equation can be solved to give:

$$x_0 = \frac{E_0 e}{i\xi\omega + m\omega_0^2 - m\omega^2} \tag{2.4}$$

where the real part of E_0 and x_0 are the amplitudes of the driving electric field and response respectively, and ω_0 is the resonant frequency of the system. The observable physical effect of these electrons shaking back and forth is that a new electric field is radiated by these induced dipoles, which combines with the incident electric field. This leads to a change in the phase velocity of the light which is a sum of these two electric fields.

The index of refraction for a medium is defined as the ratio of the velocity of light in the medium to the velocity of light in a vacuum, $n = \frac{c}{v}$, and the phase velocity of a wave is given by $v = \frac{\omega}{k}$. In the linear case, the electric field (E) and polarization (P) have the same frequency (ω) and wavevector (k).

In a polarizable medium, the wave vector of light will be shorter compared to the wave vector in vacuum. This can be most clearly seen by solving the wave equation for an electric field and induced polarization in a polarizable medium. Starting with Maxwell's equations in matter:

$$\nabla \times \vec{E} = -\frac{\partial}{\partial t}\vec{B}, \tag{2.5}$$

$$\nabla \cdot \vec{D} = \rho_f, \tag{2.6}$$

$$\nabla \times \vec{H} = \frac{\partial}{\partial t}\vec{D} + \vec{j}, \tag{2.7}$$

$$\nabla \times \vec{B} = 0, \tag{2.8}$$

where $\vec{H} = \frac{1}{\mu}\vec{B}$, ρ_f is the density of free charges, and $\vec{j}$ is the current density. Including the effect of material polarization in the electric displacement,

$$\vec{D} = \epsilon_0 \vec{E} + \vec{P} \tag{2.9}$$

provides a set of equations that can be solved for wave solutions in a polarizable medium. To simplify them, consider the case with no free charges, so $\rho_f = 0$ and $\vec{j} = 0$. In the usual way, we take the curl of Eq. 2.5 and combine the results to get the wave equation:

$$\nabla \times \nabla \times \vec{E} + \frac{1}{c^2}\frac{\partial^2}{\partial t^2}\vec{E} = -\frac{1}{c^2}\frac{\partial^2}{\partial t^2}\frac{1}{\epsilon_0}\vec{P}. \tag{2.10}$$

In the simplest case when the polarization depends linearly on the applied electric field, we can insert equation 2.1 into the wave equation 2.10. This results in a differential equation with $\vec{E}$

$$\nabla \times \nabla \times \vec{E} + \frac{1}{c^2}\frac{\partial^2}{\partial t^2}\vec{E} = -\frac{1}{c^2}\frac{\partial^2}{\partial t^2}\chi\vec{E} \tag{2.11}$$

which simplifies to

$$\nabla \times \nabla \times \vec{E} + \frac{1}{c^2}\left(1+\chi\right)\frac{\partial^2}{\partial t^2}\vec{E} = 0. \tag{2.12}$$

and after taking the time and space derivatives, there are three seperate equations for each component of the electric field ($\vec{\mathcal{E}} = \mathcal{E}_x\hat{\imath} + \mathcal{E}_y\hat{\jmath} + \mathcal{E}_z\hat{k}$). If an optical field with a transverse electric field traveling in the x direction is assumed, equation 2.12 can

be simplified to yield,

$$-\frac{\partial^2}{\partial x^2}E + \frac{1+\chi}{c^2}E = 0. \tag{2.13}$$

At this point, we can assume a harmonic plane wave solution in the form of

$$E(x,t) = \mathcal{E}\exp\left(i(kx - \omega t)\right) \tag{2.14}$$

which results in the expression

$$k^2\mathcal{E} - \frac{\omega^2}{c^2}(1+\chi)\mathcal{E} = 0. \tag{2.15}$$

Only certain values for the wavevector k and frequency ω can satisfy this equation.

$$k^2 - \frac{\omega^2}{c^2}(1+\chi) = 0 \tag{2.16}$$

$$k = \frac{\omega}{c}\sqrt{1+\chi} \tag{2.17}$$

So one effect of the induced linear polarization P is to increase the wavevector by a factor of $\sqrt{1+\chi}$, which means that the wavelength of the electric field in a polarizable medium is shorter then it would be in a vacuum. This factor is the index of refraction

$$n = \sqrt{1+\chi} \tag{2.18}$$

which is also responsible for the modification of the phase velocity of light.

Because of the assumption that the polarization P is linearly proportional to the applied electric field E (2.1), any superposition of solutions to the wave equation (2.10) is also a solution, and optical waves cannot influence each other. However, many interesting things happen if we consider higher order effects.

2.3 Non-linear Optics, Classical Description

The previous section shows that the principle effect of a polarizable, linear medium without free charges (and therefore absorption) on a propagating electromagnetic

field is the modification of its phase velocity. An assumption was made that the polarization P was simply linearly proportional to the applied electric field E. When the polarization is allowed to depend on the electric field in a non-linear way, many other effects can occur. One significant consequence is that it is then possible for the presence of one (or more) electric field(s) to influence the propagation of another electric field. *Light-light* interaction becomes possible.

To quantify this behavior, we assume that that the polarization can be written as a linear part plus a non-linear part, and that the non-linear part is a small correction. Thus, we can write:

$$\vec{P}(\vec{x},t) = \epsilon_0 \vec{\chi} \cdot \vec{E}(\vec{x},t) + \vec{P}^{(NL)}(\vec{x},t) \tag{2.19}$$

where $\epsilon_0 \vec{\chi} \cdot \vec{E}(\vec{x},t)$ is the linear polarization discussed in the previous section, and $\vec{P}^{(NL)}(\vec{x},t)$ is the additional non-linear polarization, which depends on higher orders of $\vec{E}$.

Generally, the assumption that the non-linear polarization is a small correction to the total polarization holds true for electric fields that apply forces to electrons that are much smaller than the forces holding the bound electrons to their respective nuclei.

We can express $\vec{P}^{(NL)}$ as a series expansion

$$\vec{P}^{(NL)} = \vec{P}^{(2)} + \vec{P}^{(3)} + \vec{P}^{(4)} + \cdots + \vec{P}^{(n)} \tag{2.20}$$

where $\vec{P}^{(2)}$ is the second-order component, $\vec{P}^{(3)}$ is the third-order component, and $\vec{P}^{(n)}$ is the n^{th} component.

For clarity, and to simplify the notation, let us consider a scalar version of equation 2.19 and a material that has a non-zero $\chi^{(3)}$ so that it generates a non-linear polarization proportional to E^3 (see equation 2.21). For the interaction of three separate beams, we allow each optical field to have a different wave vector $\vec{k}_n$, but will keep each frequency ω the same (and therefore the length of each $\vec{k}_n$ is the

same),

$$P^{(3)}(\vec{x},t) = \epsilon_0 \chi^{(3)} \left[E(\vec{x},t)\right]^3 \tag{2.21}$$

and the total electric field from three optical waves E with wave vectors k_n can be written as:

$$E(\vec{x},t) = \frac{1}{2}\sum_{n=1}^{3}\left(\mathcal{E}_n e^{i[\vec{k}_n\cdot\vec{x}-\omega t]} + \mathcal{E}_n^* e^{-i[\vec{k}_n\cdot\vec{x}-\omega t]}\right) \tag{2.22}$$

where $\mathcal{E}_n$ is the complex amplitude of the field with wave vector $\vec{k}_n$.

If we then insert the sum of three incident optical waves with three different wave vectors into equation 2.21 we get a result with many mixing terms (see Appendix A). We can regroup the result into like terms with their respective complex conjugates to determine the complex amplitudes of various third-order processes. A polarization is generated at 3ω which is third-harmonic generation (THG) and other combinations of the fields interact to produce other non-linear polarizations. Of primary interest here is the one that is phase matched in a homogenous, isotropic material.

There are three polarization waves with a frequency of ω, one with a wave vector of $\vec{k}_1 + \vec{k}_2 - \vec{k}_3$, another with a wave vector of $\vec{k}_1 - \vec{k}_2 + \vec{k}_3$, and the third with $-\vec{k}_1 + \vec{k}_2 + \vec{k}_3$. However, in general for three non-collinear beams, only one of these polarizations can be phase matched. In the geometry defined in Fig. 2.1 and Fig. 2.2, only the polarization with a wave vector of $\vec{k}_1 + \vec{k}_2 - \vec{k}_3$ will radiate a phase-matched optical beam. This optical wave is

$$\frac{3}{4}\epsilon_0 \chi^{(3)}\left(\mathcal{E}_1\mathcal{E}_2\mathcal{E}_3^* e^{i[(\vec{k}_1+\vec{k}_2-\vec{k}_3)\cdot\vec{x}-\omega t]} + c.c.\right) \tag{2.23}$$

and therefore has a complex amplitude of

$$\frac{3}{2}\epsilon_0 \chi^{(3)}\mathcal{E}_1\mathcal{E}_2\mathcal{E}_3^*. \tag{2.24}$$

Because the wave vector has the correct length to satisfy the wave equation, the dipole radiation from the polarization sums coherently (in-phase) and it can be inserted as a source term into the wave equation. The radiated wave is further analyzed in Chapter 3.

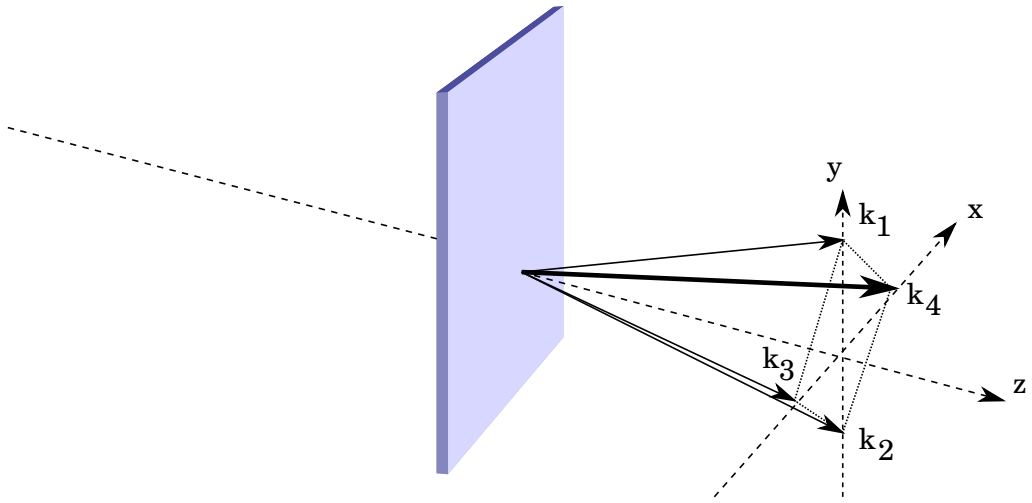

Figure 2.1: A perspective illustration of the forward DFWM geometry, showing the incident beams (k_1, k_2, k_3) overlapping in the sample and the wave radiated from the non-linear polarization ($k_4 = k_1 + k_2 - k_3$).

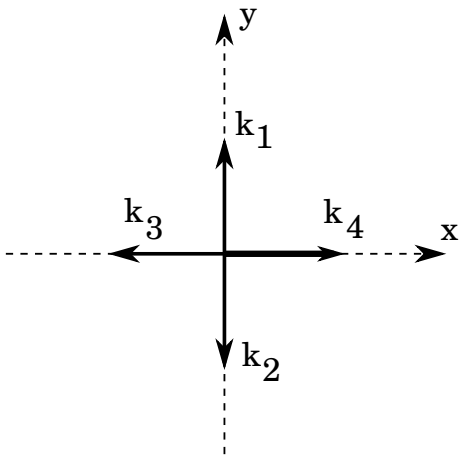

Figure 2.2: End view of the DFWM geometry, looking down the negative z-axis (opposite the direction of propagation).

2.4 Non-linear Optics, Third-order Molecular Polarizability

In 1962, Armstrong et al published a SoS expression for the non-linear optical polarization of an isolated system using perturbation theory [7]. Nine years later, Orr and

Ward published the same expression, but written a different way [8]. In summary, they start with a perturbation to the Hamiltonian (which may be time-dependent) and express that additional energy as a dipole interaction with an electric field as

$$H(t) = H(0) + \epsilon H^{'}(t) \tag{2.25}$$

where

$$\epsilon H^{'}(t) = -e\mathbf{E}(t) \cdot \mathbf{r}. \tag{2.26}$$

$\mathbf{E}$(t) is the externally applied electric field, and e is the charge of the electron. This can be expressed as a series expansion in electric field, using linear combinations of solutions to the unperturbed Hamiltonian. For further details, see Appendix B.

We can relate the molecular third-order polarizability (γ) of a molecule to the third-order susceptibility $\chi^{(3)}$ of a solution of those molecules by

$$\chi^{(3)}_{1111}(N_d) = \chi^{(3)}_{1111}(0) + f^4 N_d \gamma_{rot} \tag{2.27}$$

where $f = (n^2 + 2)/3$ is a Lorentz local field factor, n is the refractive index of the solvent ($n = 1.42$ for the solvent we will use, CH_2Cl_2), N_d is the number density of molecules in solution, and γ_{rot} is the effective scalar third-order polarizability that is obtained from a rotational average of the corresponding molecular tensor [9]. The number density can be expressed in terms of wt% concentration (C), as mass of molecule divided by mass of solute, which is more convenient experimentally,

$$N_d = (C/100)\rho \frac{N_A}{M}, \tag{2.28}$$

where ρ is the mass density of the solution, N_A is Avogadro's number, and M is the molar mass. We assume that the concentration is small ($C < 2.0$ wt%).

The SoS expression by Orr and Ward for the third-order polarizability is

$$\gamma_{xxxx}(-\omega_\sigma; \omega_1, \omega_2, \omega_3) = \frac{1}{\epsilon_0 \hbar^3} \left(\sum_{lmn}^{\infty} \frac{x_{0l} x_{lm} x_{mn} x_{n0}}{D^{-1}_{lmn}(\omega_1, \omega_2, \omega_3)} - \sum_{mn}^{\infty} \frac{x_{0m} x_{m0} x_{0n} x_{n0}}{D^{-1}_{mn}(\omega_1, \omega_2, \omega_3)} \right) \tag{2.29}$$

as derived by Ref. [8] and rewritten by Ref. [10]. In this expression, the dispersion terms are:

$$
\begin{aligned}
D_{lmn}(\omega_1,\omega_2,\omega_3) = \Bigg(& \frac{1}{(\hbar\Omega_{lg}-\hbar\omega_\sigma)(\hbar\Omega_{mg}-\hbar\omega_1-\hbar\omega_2)(\hbar\Omega_{ng}-\hbar\omega_1)} \\
& + \frac{1}{(\hbar\Omega^*_{lg}+\hbar\omega_3)(\hbar\Omega_{mg}-\hbar\omega_1-\hbar\omega_2)(\hbar\Omega_{ng}-\hbar\omega_1)} \\
& + \frac{1}{(\hbar\Omega^*_{lg}-\hbar\omega_1)(\hbar\Omega^*_{mg}+\hbar\omega_1+\hbar\omega_2)(\hbar\Omega_{ng}-\hbar\omega_3)} \\
& + \frac{1}{(\hbar\Omega^*_{lg}+\hbar\omega_1)(\hbar\Omega_{mg}+\hbar\omega_1+\hbar\omega_2)(\hbar\Omega^*_{ng}+\hbar\omega_\sigma)} \\
& + \text{all six permutations of } (\omega_1,\omega_2,\omega_3) \text{ the above terms} \Bigg)
\end{aligned}
\tag{2.30}
$$

and

$$
\begin{aligned}
D_{mn}(\omega_1,\omega_2,\omega_3) = \Bigg(& \frac{1}{(\hbar\Omega_{mg}-\hbar\omega_\sigma)(\hbar\Omega_{mg}-\hbar\omega_3)(\hbar\Omega_{ng}-\hbar\omega_1)} \\
& + \frac{1}{(\hbar\Omega_{mg}-\hbar\omega_3)(\hbar\Omega^*_{ng}+\hbar\omega_2)(\hbar\Omega_{ng}-\hbar\omega_1)} \\
& + \frac{1}{(\hbar\Omega^*_{mg}+\hbar\omega_\sigma)(\hbar\Omega^*_{mg}+\hbar\omega_3)(\hbar\Omega^*_{ng}+\hbar\omega_1)} \\
& + \frac{1}{(\hbar\Omega^*_{mg}+\hbar\omega_3)(\hbar\Omega_{ng}-\hbar\omega_2)(\hbar\Omega^*_{ng}-\hbar\omega_1)} \\
& + \text{all six permutations of } (\omega_1,\omega_2,\omega_3) \text{ of the above terms} \Bigg)
\end{aligned}
\tag{2.31}
$$

In 2008, Moreno, Clays, and Kuzyk derived a new SoS expression using Thomas-Kuhn sum rules to express the third-order polarizability in an equivalent, but different expression to eliminate explicit dependence on dipolar terms. They propose that their version of the SoS expression could "...be used to develop a three-state model of the dispersion of the third-order susceptibility that can be applied to molecules in cases where many more states would have been required" [10]. Their only assumption is that the sum rules hold, which is the case when the unperturbed Hamiltonian describing the system is conservative.

The result of their work is

$$\begin{aligned}\gamma_{xxxx}(\omega_\sigma;\omega_1,\omega_2,\omega_3) = \frac{1}{\epsilon_0\hbar^3}\sum_n^\infty\sum_{m\neq n}^\infty\sum_{l\neq n}^\infty \frac{(2E_{m0}-E_{n0})(2E_{l0}-E_{n0})}{E_{n0}^2}\frac{x_{0m}x_{mn}x_{nl}x_{l0}}{D_{nnn}^{-1}} \\ -\sum_n^\infty\sum_{m\neq n}^\infty\sum_{l\neq n}^\infty \frac{(2E_{l0}-E_{m0})}{E_{m0}}\frac{x_{0l}x_{lm}x_{mn}x_{n0}}{D_{mmm}^{-1}} \\ -\sum_n^\infty\sum_{l\neq n}^\infty\sum_{m\neq n}^\infty \frac{(2E_{m0}-E_{n0})}{E_{n0}}\frac{x_{0l}x_{ln}x_{nm}x_{m0}}{D_{lnn}^{-1}} \\ -\sum_n^\infty\sum_{m\neq n}^\infty\sum_{l\neq m}^\infty \frac{x_{0l}x_{lm}x_{mn}x_{n0}}{D_{lmn}^{-1}} - \sum_{mn}^\infty \frac{x_{0m}x_{m0}x_{0n}x_{n0}}{D_{mn}^{-1}}\end{aligned} \tag{2.32}$$

which is an expression that is useful in that it provides a more direct route to the derivation of fundamental limits of the third-order susceptibility [10].

2.5 Fundamental Limits

From equation 2.32, it is possible to derive expressions for the maximum theoretical third-order polarizability obtainable for a molecule with a given number of π electrons and a certain energetic difference between the ground and first excited state. This is a useful comparison for designing molecules with large third-order polarizabilities to provide a reference of how well a molecule utilizes the available π electrons, and how well suited the first optical transition is for non-linear optics.

Kuzyk uses the fact that near the fundamental limit, only three levels contribute to the non-linear response [11–13]. In the off-resonant limit, equation 2.32 reduces to:

$$\begin{aligned}&\gamma_{xxxx}(-\omega_\sigma;\omega_1,\omega_2,\omega_3) \\ &= \frac{1}{\epsilon_0\hbar^3}\left(\frac{D_{111}(2E_{20}-E_{10})^2}{E_{10}^2}+D_{212}-\frac{(2E_{20}-E_{10})}{E_{10}}(D_{211}+D_{112})\right)|x_{02}|^2|x_{12}|^2 + \\ &e^4\left(\frac{D_{222}(2E_{10}-E_{10}-E_{20})^2}{E_{20}^2}+D_{121}-\frac{(2E_{10}-E_{20})}{E_{20}}(D_{122}+D_{221})\right)|x_{01}|^2|x_{12}|^2 - \\ &e^4\left(D_{11}|x_{01}|^4+(D_{21}+D_{12})|x_{02}|^2|x_{01}|^2+D_{22}|x_{02}|^4\right)\end{aligned} \tag{2.33}$$

where the dispersion terms become

$$D_{lmn}^{\text{off}} = 4\left(\frac{1}{E_{l0}E_{m0}E_{n0}}\right) \tag{2.34}$$

and

$$D_{mn}^{\text{off}} = 2\left(\frac{1}{E_{m0}^2E_{n0}} + \frac{1}{E_{m0}E_{n0}^2}\right) \tag{2.35}$$

when the frequency is zero. This derivation establishes upper bounds on the limits of the third-polarizability.

The limits are derived separately for two different molecular symmetries, centrosymmetric and non-centrosymmetric. The magnitude of the non-centrosymmetric limit is four times larger then the centrosymmetric limit, however the centrosymmetric limit can still be used as a benchmark to compare all molecules, regardless of their symmetry. The magnitude of the zero-frequency limit (for a centrosymmetric molecule) is given by the fourth power of the maximum dipole transition matrix element divided by the third-power of the first optical excitation energy [14]

$$\gamma_k = \frac{1}{\epsilon_0}\left[\frac{e^2\hbar^2N_\pi}{2m^2E_{10}}\right]^2\frac{1}{E_{10}^3} = \frac{e^4\hbar^2}{\epsilon_0 m^2}\frac{N_\pi^2}{E_{10}^5}, \tag{2.36}$$

where ϵ_0 is the electric constant that is part of the definition of the polarizability in the S.I. system, the term in square brackets is the square of the maximum dipole transition matrix element as determined by sum-rules [14], e is the elementary charge, N_π is the number of conjugated electrons, m is the mass of the electron, and E_{10} is the energy difference between the first optically accessible excited state and the ground state.

In addition to the fundamental limit for the off-resonant γ_k (equation 2.36), Kuzyk also derived an expression for the fundamental limit for the magnitude of the third order polarizability on resonance [15].

Kuzyk uses two ratios to derive a resonant limit for the imaginary part of γ from equation 2.36. The first ratio is obtained from the term in SoS expression which

becomes dominant at resonance. It is

$$\gamma \propto \frac{\mu_{02}^2 \mu_{12}^2}{(E_{20} - \hbar\omega - i\Gamma_{20})^2 (E_{10} - 2\hbar\omega - i\Gamma_{10})}. \tag{2.37}$$

Note that we define the energy levels differently from his paper, so that E_{10} is the first optical transition here.

At resonance, when this term dominates the SoS expression, the ratio of the imaginary part to the real part of γ has been worked out in Ref. [15]. Re-written with the alternate definitions of E_{10} and E_{20}, it is

$$\frac{\gamma_I}{\gamma_R} = \frac{\Gamma_{10}}{E_{10}} + 2\frac{\Gamma_{20}}{E_{20}}. \tag{2.38}$$

Kuzyk also works out the ratio for the maximum resonant γ_I^{res} to the maximum off-resonant γ_I [15] which becomes

$$\frac{\gamma_I^{\text{res}}}{\gamma_I^{\text{off}}} = \left[\frac{E_{20}}{E_{20} - \frac{E_{10}}{2}}\right]^2 \left[\frac{1}{\left(\frac{\Gamma_{10}}{E_{10}}\right)\left(2\frac{\Gamma_{20}}{E_{20}} + \frac{\Gamma_{10}}{E_{10}}\right)}\right] \tag{2.39}$$

when written in a consistent way with the above equations. The combination of these two ratios, with γ_k, results in an expression for the maximum γ_k^{res} that could be theoretically achieved, derived from sum rules, and in terms of physical quantities that can be measured for a molecule.

The result is

$$\gamma_k^{\text{res}} = \gamma_k \frac{E_{10}^2 E_{20}}{\left(E_{20} - E_{10}/2\right)^2 \Gamma_{10}} \tag{2.40}$$

in units of γ_k.

It is important to note that with our definition of E_{10} and E_{20}, there is no double resonance, which would occur when $E_{20} = E_{10}/2$. Written this way, E_{10} is the lowest optical energy transition, therefore $E_{20} > E_{10}$.

To visualize the influence of molecular parameters E_{10} and E_{20} on this ratio, see Fig. 2.3. In the limit $E_{20} \to \infty$, $\gamma_k^{\text{res}}/\gamma_k \to 0$ because this particular term does not allow two-photon absorption in the case of a two-level system. The limit γ_k is not

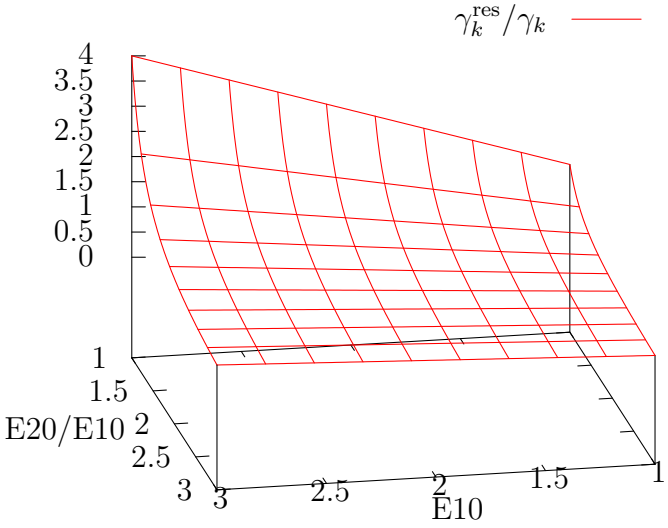

Figure 2.3: Value of the ratio γ_k^{res}/γ_k ploted in terms of E_{10} and E_{20}/E_{10}, confined to the region where $E_{20} > E_{10}$. For this plot, $\Gamma_{10} = 3$.

independent of E_{10} because $\gamma_k \propto E_{10}^{-5}$ (see equation 2.36). See Fig. 2.4 for a plot of the maximum theoretical value γ_k^{res} as a function of E_{10} and E_{20}. When the two states are degenerate, γ_k^{res} is a maximum.

These two fundamental limits (off-resonant and resonant) allow assessment of a molecular design, how well it utilizes the available π electrons, and how well the first (γ_k) or first two (γ_k^{res}) optical transitions are suited for achieving large off-resonant, or on-resonance third-order polarizabilities.

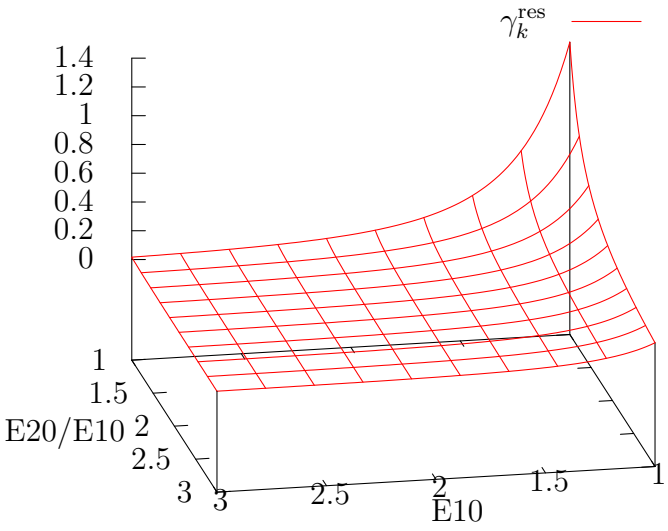

Figure 2.4: Value of the γ_k^{res} as a function of E_{10} and E_{20}/E_{10}. The maximum value occurs where $E_{20} = E_{10}$.

Chapter 3

Experimental Techniques

The invention of the laser caused a figurative explosion (or literal, in some cases [5]) of research into non-linear optical physical effects, materials, and experimental methods. The ability to generate coherent and intense optical beams opened the door for new physics and the investigation of new material properties, including non-linear optics. One of the first demonstrations of non-linear optics was the observation of second-harmonic generation (SHG) in Ref. [16]. In addition to SHG and THG, non-linear optics allows for the transfer of energy from one beam into another (amplification) so that wavelengths other then the laser fundamental (or harmonics thereof) can be generated. This is the basis for tuneable wavelength sources such as used in this research. Pulsed lasers also make achieving extremely peak intensity possible, allowing for the investigation of higher-order non-linear effects that depend on higher orders of the electric field.

This chapter will discuss degenerate four wave mixing as an experimental method for measuring the optical wave radiated by the non-linear polarization.

3.1 DFWM

Of particular interest in this research is the case when three incident optical beams have the same frequency and a fourth beam is generated at the same frequency. This physical process is called degenerate four-wave mixing (DFWM) and provides some

experimental advantages. Compared to third harmonic generation (THG), DFWM is clearly in resonance with one optical transition over a wider spectral range, and is therefore more suitable for non-linear spectroscopy. It also allows the observation of time-dynamics, and is more sensitive at the same intensity than Z-scan. We have the freedom to control the beam polarizations separately, as well as the time-delay of the three incident pulses with respect to each other. The geometry of a DFWM arrangement can be chosen to be phase-matched (which is not generally true for THG) so weak effects can result in strong signals.

Degenerate four-wave mixing measures the non-linear signal radiated by the third-order polarization $\vec{P}^{(3)}$ discussed in Chapter 2; it is a third order process because it depends on a mixing process of three incident beams. In DFWM they have the same frequency (hence degenerate), and the geometry can be chosen so that the non-linear component of the polarization $\vec{P}$ can radiate a fourth beam in a phase matched condition. This beam then satisfies the non-linear wave equation (see Chapter 2).

In the approximation of slowly varying amplitude, and without depletion of the pump-beams, the polarization will radiate a wave with an electric field that increases linearly with propagation distance as

$$E_4(z) = \frac{ik_4}{2\epsilon_0}\epsilon_{4j}^{-1}P_j^{(3)}z. \tag{3.1}$$

In the case of linear absorption, the three incident pump beams will be depleted, and this will impact the DFWM signal radiated by the nonlinear optical polarization. We start analyzing the effect of linear absorption by defining a length-dependent polarization as

$$P^{(3)}(z) = \epsilon_0\chi^{(3)}E_1E_2E_3^*\left[e^{-\frac{\alpha}{2}z}\right]^3 \tag{3.2}$$

which takes into account the linear absorption of the 3 incident pump beams with complex amplitudes E_1, E_2, and E_3 with wave vectors $\mathbf{k}_1, \mathbf{k}_2, \mathbf{k}_3$, respectively. The phase-matched DFWM optical wave with amplitude E_4 has a wave vector $\mathbf{k}_4 = \mathbf{k}_1 + \mathbf{k}_2 - \mathbf{k}_3$. Inserting this polarization as a source term into the wave equation,

and making the approximation of slowly varying amplitude to eliminate second-order space derivatives results in

$$ik_4\frac{\partial}{\partial z}E_4(z) - k^2E_4(z) + \frac{\omega^2n^2}{c^2}E_4(z) = -\frac{\omega^2}{c^2}\chi^{(3)}E_1E_2E_3^*\left[e^{-\frac{\alpha}{2}z}\right]^3 \tag{3.3}$$

which, because it is phase matched, simplifies to

$$\frac{\partial}{\partial z}E_4(z) = \frac{i}{k_4}\frac{\omega^2}{c^2}\chi^{(3)}E_1E_2E_3^*\left[e^{-\frac{\alpha}{2}z}\right]^3. \tag{3.4}$$

The signal radiated by the polarization at the same frequency is also subject to the same linear absorption, so we can add one additional term to this equation

$$\frac{\partial}{\partial z}E_4(z) = \frac{i}{k_4}\frac{\omega^2}{c^2}\chi^{(3)}E_1E_2E_3^*\left[e^{-\frac{\alpha}{2}z}\right]^3 - \frac{\alpha}{2}E_4(z), \tag{3.5}$$

which can be solved for $E_4(z)$. The result is

$$E_4(z) = \left(\frac{1}{\alpha}\frac{i}{k_4}\frac{\omega^2}{c^2}\chi^{(3)}E_1E_2E_3^*(1-e^{-\alpha z})\right)e^{-\frac{\alpha}{2}z} \tag{3.6}$$

which shows that the electric field of the wave radiated by the nonlinear polarization will initially grow linearly with distance z, as

$$E_4(z) = \frac{ik_4}{2\epsilon_0}\epsilon_{4j}^{-1}P_j^{(3)}z, \tag{3.7}$$

but the linear absorption depletes the pump beam, and results in attenuation of the radiated wave (see Fig. 3.1).

The intensity of the radiated signal wave depends on the intensity of the three pump waves and on the interaction distance z, as

$$I_4 \propto \frac{z^2}{n_in_jn_kn_l}I_1I_2I_3\left|\chi^{(3)}\right|^2\left[\frac{1-e^{-\alpha z}}{\alpha z}e^{-\alpha z/2}\right]^2. \tag{3.8}$$

The term in square brackets tends to $(1-2\alpha z)$ as αz goes to zero, and can also be well approximated by $\exp(-2\alpha z)$, which for a sample of thickness z is equivalent to

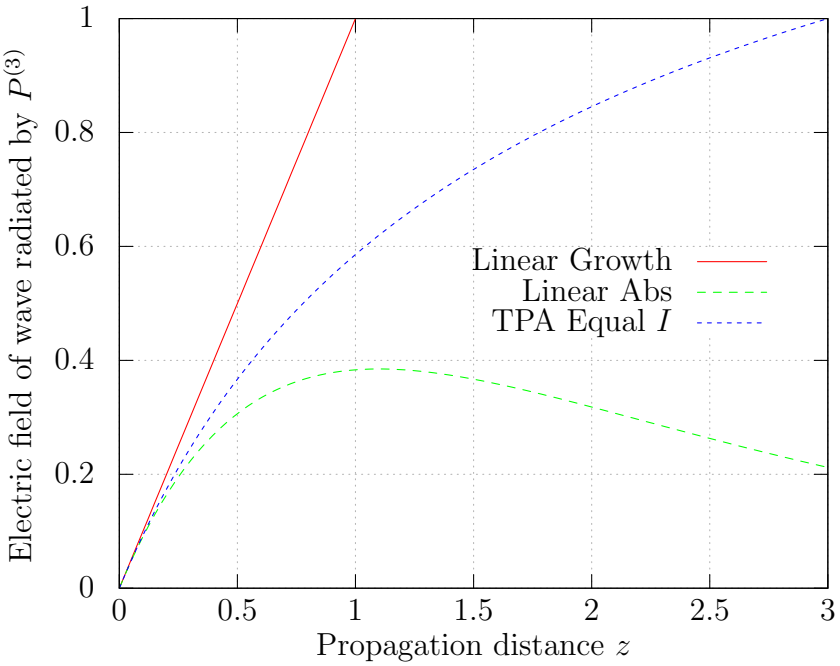

Figure 3.1: Comparison of the relative effects of pump-beam depletion by linear absorption ($\alpha > 0$) and TPA ($\beta > 0$) with arbitrary values.

saying that the signal intensity is given by $I_4 \propto z^2 I_1 I_2 I_3$ with all intensities taken in the middle of the sample.

As long as the pump beams are not depleted by two-photon absorption (TPA) over the thickness of the sample, the imaginary part of the third-order polarizability contributes significantly to the strength of the DFWM signal. Its only effect is an additional phase shift of the generated signal wave. In our experimental configuration, with all interacting beams sharing the same polarization, the signal wave has an intensity proportional to $|\chi^{(3)}_{1111}(C)|^2$. This signal is in contrast to z-scan, in which one observes the transmission of a single optical wave and the imaginary part of the third-order susceptibility can only be detected in the form of an attenuation of the transmitted wave [17].

However, if the pump beams *do* have such an intensity that they are depleted by TPA (or cross-TPA), the effect on the wave radiated by the non-linear polarization

must be considered. In this case, the z dependence of the intensity dependent absorption is described by the so that differential equation $\frac{dI}{dz} = -\beta I^2$ and the solution is: $I(z) = I_0/(1 + \beta I_0 z)$. Taking a similar procedure as above, except neglecting linear absorption, the differential equation for the amplitude of the radiated wave becomes

$$\frac{\partial}{\partial z} E_4(z) = \frac{i}{k_4} \frac{\omega^2}{c^2} \chi^{(3)} E_0 E_0 E_0^* \left[\frac{1}{1 + \beta I_0 z} \right]^{3/2} \tag{3.9}$$

when each incident pump beam has the same intensity I_0. The solution to this equation is

$$E_4(z) = \frac{2}{\beta I_0} \frac{i}{k_4} \frac{\omega^2}{c^2} \chi^{(3)} E_0 E_0 E_0^* \left[1 - \frac{1}{\sqrt{1 + \beta I_0 x}} \right], \tag{3.10}$$

and the corresponding expression for the DFWM signal intensity is

$$I_4 \propto \frac{z^2}{n_i n_j n_k n_l} I_0^3 \left| \chi^{(3)} \right|^2 \left[2 \frac{1 - (1 + \beta I_0 z)^{-1/2}}{\beta I_0 z} \right]^2, \tag{3.11}$$

with the correction term in square brackets tending to $1 - 3\beta I d/2$ in the limit $\beta I d \to 0$. Examples of signal growth with propagation distance are shown in Fig. 3.1. A more complete analysis for the case of different intensities between the interacting beams can be done by numerically integrating equation 3.12,

$$\begin{aligned} \frac{\partial}{\partial z} E_4(z) &= \frac{i}{k_4} \frac{\omega^2}{c^2} \chi^{(3)} E_1 E_2 E_3^* \\ &\quad \times \left[\frac{1}{(1 + \beta I_1 z)(1 + \beta I_2 z)(1 + \beta I_3 z)} \right]^{1/2}, \end{aligned} \tag{3.12}$$

which is a well-behaved function allowing quick convergence.

Another consequence (besides depletion of the pump beams) of TPA is that some energy is deposited in the solution, resulting in some number density of molecules in an excited state. With DFWM, it is possible to determine the impact of this excitation, and measure the time dependence of the DFWM signal to determine the excited-state lifetime.

The experimental setup uses a wavelength-tunable stream of 1-ps light pulses at

a repetition rate of 1 kHz, which is provided by a TOPAS traveling-wave optical parametric amplifying system from Light Conversion, pumped by a Clark-MXR CPA-amplified laser. The DFWM experiment uses a forward configuration, with the coordinates of the interacting wavevectors in the plane of the sample positioned at the opposite corners of a square for waves 1 and 2, and in the remaining corner for wave 3, see Fig. 2.1 and 2.2 on page 12. The arrival time of pulse 1 in the sample is accurately controlled by a translation stage. At longer delay times of pulse 1, the setup is sensitive to any population grating left behind by the interference of pulses 1 and 2, which can be used to study the dynamics of the excited states populated by two-photon absorption.

The molecular third-order polarizabilities of the molecules in Fig. 3.2 are investigated by dissolving the molecules in CH_2Cl_2 (DCM) and studying the nonlinear response of 1-mm-thick solutions prepared in fused-silica spectroscopy cells. Such solutions have a third-order susceptibility given by equation 2.27. From the nonlinear optical response of the solutions as a function of molecular concentration, we determine the rotational average of the third-order polarizability. Absolute values for the third-order susceptibility of the solutions are obtained via DFWM, by comparing to a reference measurement. We established the $\chi^{(3)}_{1111}(0)$ for a 1-mm cell filled with the pure solvent to be 6 ± 1 times larger than for a 1-mm-thick fused-silica sample, for which we used a third-order susceptibility of $1.9 \times 10^{-22}\mathrm{m}^2\mathrm{V}^{-2}$. This value corresponds to the weighted average of the values given in [18–21] taking into account dispersion, as well as the different nonlinear process as in the case of [18]. All values are with 10% of each other.

Fig. 3.3 gives an example of the time dependence of the DFWM signal, when the delay of one beam is varied with respect to the other two beams. A delay of $t = 0$ corresponds to all pulses arriving in the sample at the same time.

Fig. 3.4 gives an example of the concentration dependence of the DFWM signal from a solution, as determined at a wavelength for which the third-order polarizability has a significant imaginary part and a negative real part. At the laser intensities used for this particular experiment, the two-photon absorption is strong enough to

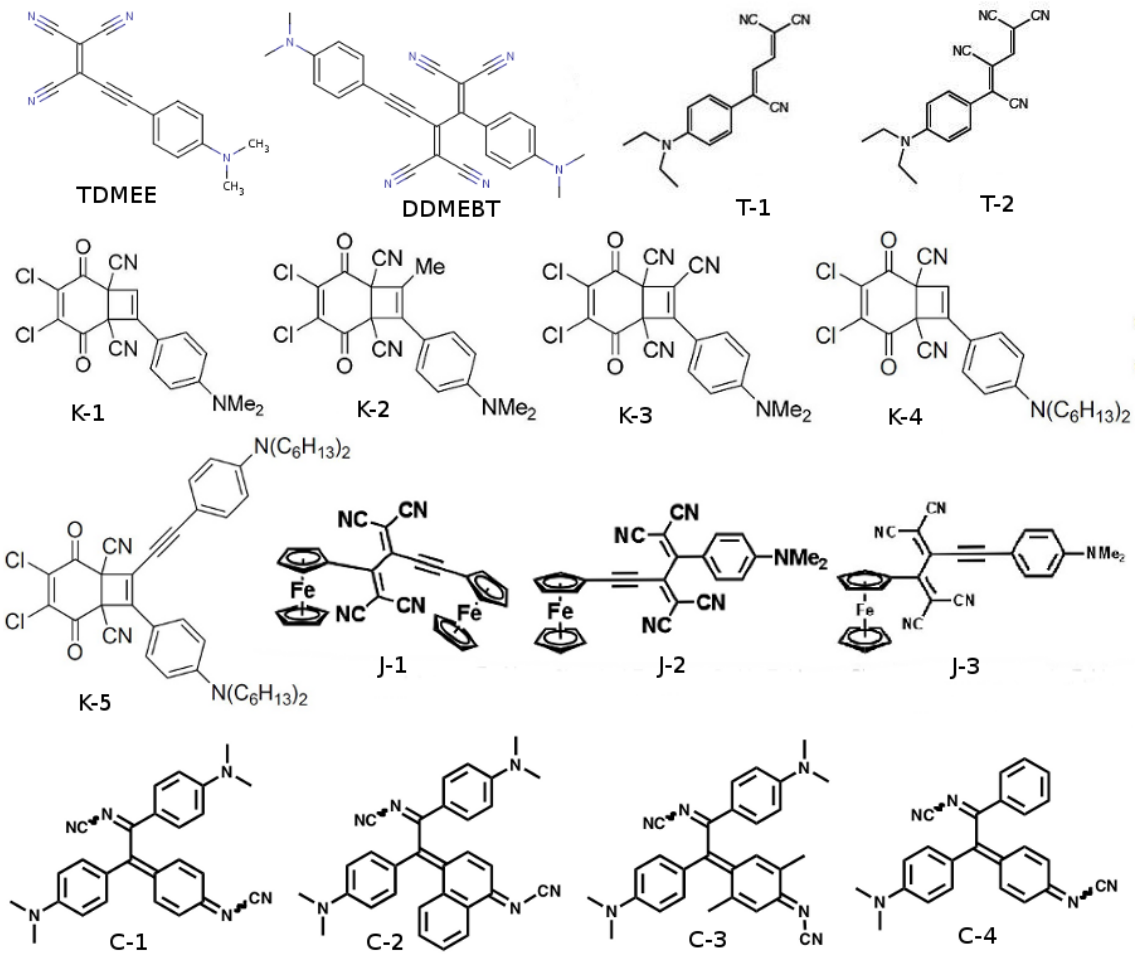

Figure 3.2: The rotational average of the third-order polarizability γ_{rot} was measured for the above molecules at a wavelength of $\lambda = 1500$ nm. This wavelength was chosen because it is commonly used in telecommunication applications, and these molecules are expected to be off-resonant.

deplete the intensities of the incident beams in the DFWM experiment, which results in an additional attenuation of the DFWM signal at higher concentrations and in a detectable nonlinear transmission of one of the incident beams.

A second example detailing the influence of large intensities on the concentration

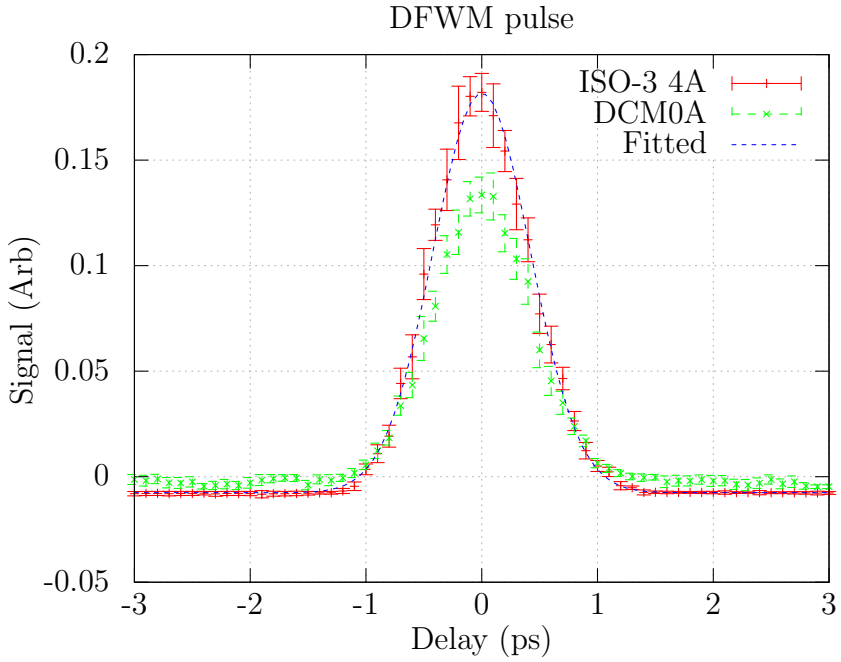

Figure 3.3: A sample of the time dependence of the DFWM signal, when the input beams to not have sufficient energy to excite the molecules in solution, either by linear absorption or TPA. In this case, the DFWM signal can be fitted with a gaussian. The amplitude is proportional to the intensity, and the square root of the amplitude is proportional to $\chi^{(3)}$. The DCM cell with concentration $C = 0$ is shown for comparison. The additional signal is due to the presence of the molecule Iso-3, with a relatively weak concentration of $C = 0.1419\%$. Even at such a low concentration, the additional signal at 1500 nm is clearly quantifiable.

dependence of the DFWM measurement is shown in Fig. 3.5. At the measured wavelength of 1180 nm, the TDMEE molecule is on the lowest two-photon resonance ($\lambda_{\max} = 591$ nm). Four sets of data were collected, at different laser powers, and then simultaneously fit with the intensities of each beam and the real and imaginary parts of γ as fitting parameters. Because the relative intensities of the three incident pump beams is different, numerical integration of equation 3.12 is used. The effect of the partially depleted pump beams is greater at higher intensities, and the fitted values for Re[γ] (-21.0) and Im[γ] (33.7) agree with other measurements.

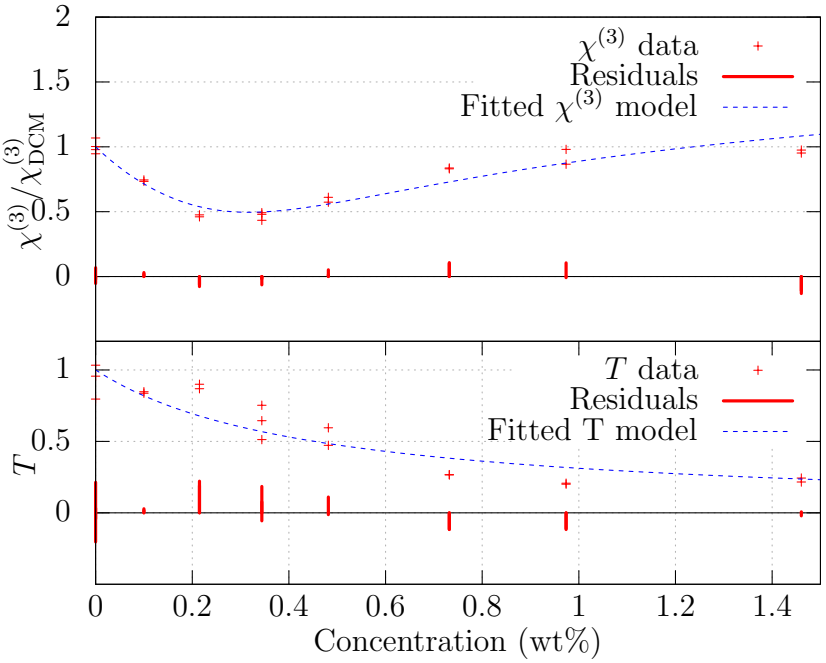

Figure 3.4: A sample of the data for TDMEE taken at 1240 nm, where the imaginary part is significant, and the intensity is large enough to see the effect of TPA. The $\chi^{(3)}$ ratios are shown in the top plot and indicate a negative real part, and imaginary part preventing an intercept with the zero axis, and responsible for non-linear absorption. In the bottom plot, the Transmission (T) data for one of the incident beams showing the non-linear absorption, and can be fit with $T = 1/(1 + \beta IL)$.

When collecting data on the wavelength dependence of γ, the full time-dependence of the DFWM signal was not measured at each wavelength. Instead, the delay tracks which control the arrival time of one beam were programmed to step back and forth between delay $t = 0$ and $t = -1.5$ ps and the difference of the two signal amplitudes is stored as the amplitude of the DFWM signal. The computer control also steps the TOPAS through a range of wavelengths where the signal does not change polarization, allowing one interaction type to be used for the spectral range. Additionally, the intensity of the transmitted beam (k_3) was collected simultaneously to provide transmission data for evidence of linear or two-photon absorption. This approach allows for the automatized collection of DFWM signal amplitudes and transmission

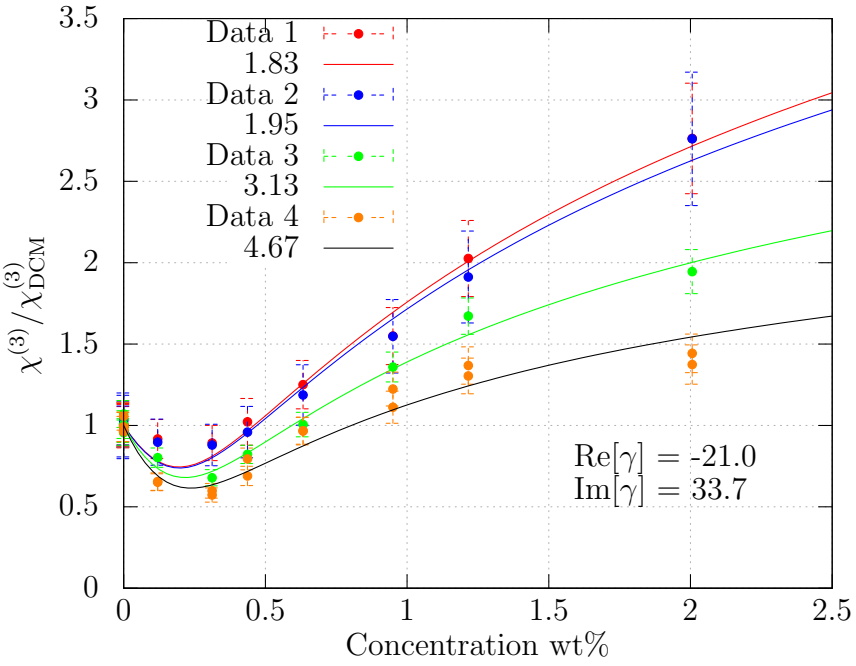

Figure 3.5: The concentration and power dependence of the TDMEE molecule, as measured at a wavelength of 1180 nm, on top of the first two-photon resonance, with 4 different laser intensities. The relative intensities of the three incident beams are different in our experimental setup, so a numerical integration of equation 3.12 was used, and all four data sets were simultaneously fit with 6 fitting parameters, the real and imaginary parts of γ, as well as the relative intensity of the laser used for each data set.

data over the wavelength range of 1050 nm to 1680 nm. For most molecules, this range includes the first TPA transition. The output power from the TOPAS drops off dramatically below 1080 nm, so frequently the data between 1050 and 1080 nm was not useable.

Additionally, the transmission data for a cell with zero concentration $\chi^{(3)}(0)$ contains the relative incident beam intensities because our solvent (DCM) is transparent over this wavelength range. So the input data collected consists of two 2D

data sets

$$\frac{\chi^{(3)}}{\chi^{(3)}_{DCM}}(C,\lambda) \tag{3.13}$$

$$T(C,\lambda) \tag{3.14}$$

and a 1D set of the relative beam intensity as a function of wavelength ($I(\lambda)$). Samples of the input data are shown in Fig. 3.6 and Fig. 3.7.

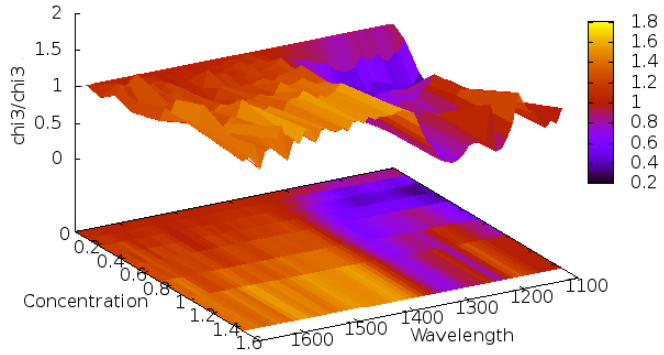

Figure 3.6: The $\chi^{(3)}$ data as a function of concentration and wavelength.

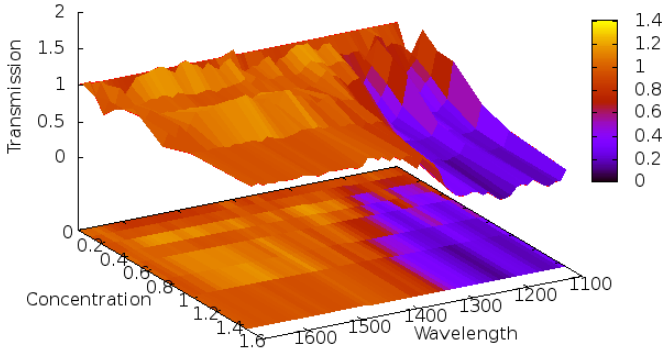

Figure 3.7: The T data as a function of concentration and wavelength.

The relative beam intensities of the three incident pump beams were measured,

and their ratios were found to be constant over the wavelength range used.

In order to allow for a smoothly varying function $\gamma(\lambda)$, a Bezier paramaterization was used. It makes physical sense that $\gamma(\lambda)$ should vary smoothly and not have discontinous jumps. An arbitrary number of control points N can be defined to allow an arbitrary degree of granularity to $\gamma(\lambda)$. When N becomes too large, the model tries to follow noise in the data, and $\gamma(\lambda)$ becomes unphysically wrinkly. If there are insufficient control points, then there is not enough flexibility in the paramaterization to adequately conform to the data.

The quadratic Bezier curve is a parametric function, defined as

$$\mathbf{B}(t) = (1-t)\left[(1-t)\mathbf{P}_0 + t\mathbf{P}_1\right] + t\left[(1-t)\mathbf{P}_1 + t\mathbf{P}_2\right], t \in [0,1], \tag{3.15}$$

which amounts to a linear interpolation between two lines, one connecting $\mathbf{P}_0$ to $\mathbf{P}_1$ and the other connecting $\mathbf{P}_1$ to $\mathbf{P}_2$ (see Fig. 3.8). For each section of the Bezier

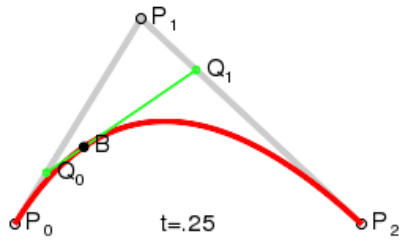

Figure 3.8: Illustration of the Bezier paramaterization. The point P_1 is located at one of the control points, but P_0 and P_2 are located midway between P_1 and the next adjacent control point.

curve in $\gamma(\lambda)$, the point $\mathbf{P}_1$ is set at a control point, and the points $\mathbf{P}_0$ and $\mathbf{P}_2$ are defined to be midway between two adjacent control points. Defined this way, one Bezier curve section will also be smoothly continuous with the next Bezier section, and it will be analytic over the desired range.

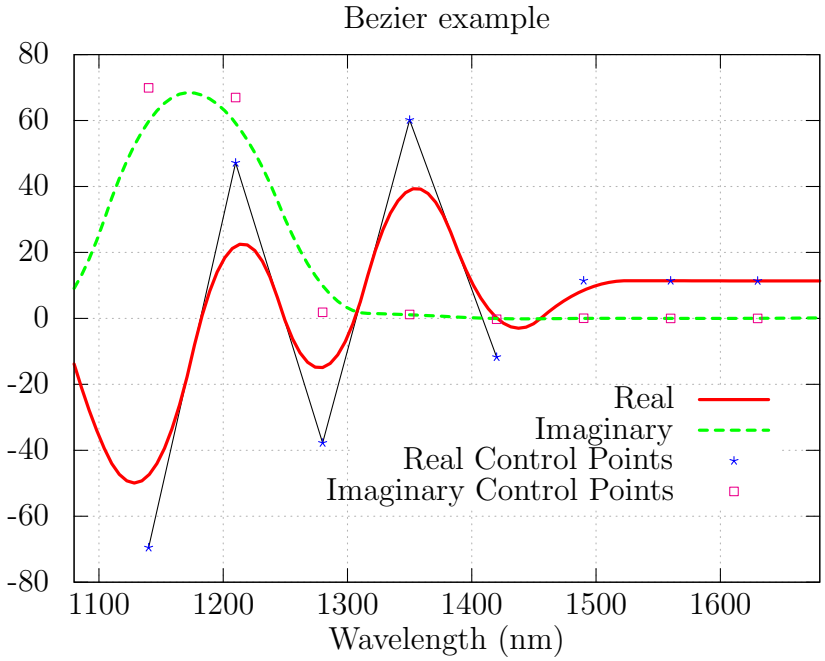

Figure 3.9: Example of the Bezier paramaterization showing the degree of flexibility for $N = 12$ control points located every 70 nm from 1000 nm to 1770 nm. The black lines show that the Bezier will be tangent to a line between two control points, midway between the two.

3.2 Molecular Solutions

A range of seven concentrations were prepared in 1mm thick optical cuvettes purchased from Starna Cells. The highest concentration depends on the solubility of the particular molecule, but is always kept below 2%. A very low concentration is prepared, sufficiently transparent through the optical region to compare the full range of spectral features with the extinction coefficients. This cell allows for the detection of decomposition. It was found that with some molecules, trace amounts of acidity were interacting with the molecules leading to decomposition, and modification of the linear absorbance spectrum. See Fig. 3.10 for an example comparison between the extinction coefficients and an absorbance spectrum showing signs of modification. To eliminate this problem, the DCM was filtered through a 10 cm

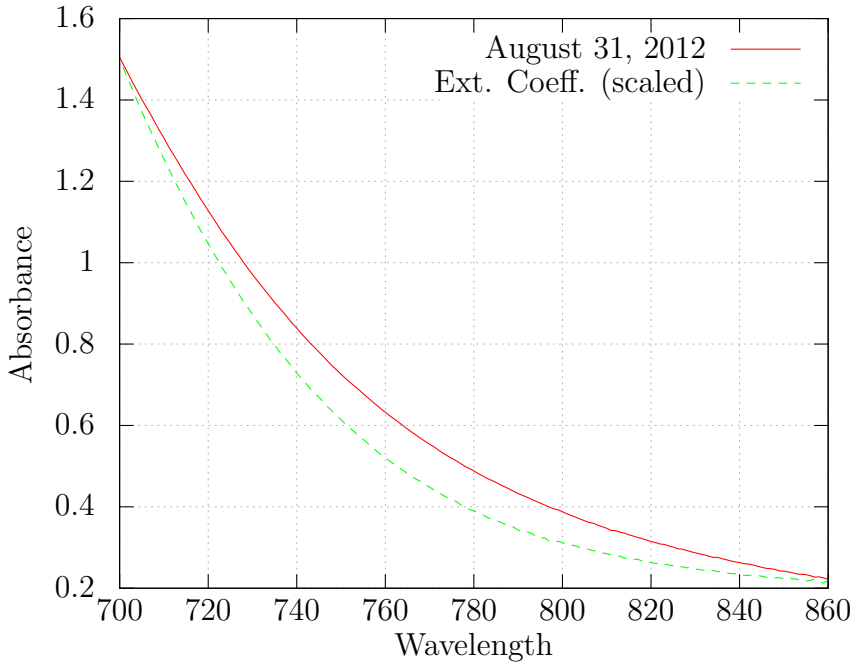

Figure 3.10: Comparison of the absorbance spectrum with the extinction coefficients for molecule ISO-3 between 700 nm and 860 nm, showing in detail the tail of the absorption peak where the mismatch can be observed. The presence of trace amounts of acids in the solvent were interacting negatively with the molecule, which could be observed as a modification of the linear absorbance spectrum.

column of basic Al_2O_3 to remove all traces of acids.

The resulting solvent provided very good solutions, which remained stable over time. The plot in Fig. 3.11 shows a comparision of the extinction coefficients with the linear absorbance spectrum of a very weak concentration of the same molecule, taken over a 2 month period. There is slight evidence of solvent evaporation, leading to a small increase in concentration, but the molecule appears to be quite stable, matching the expected spectrum very well, over a long period of time.

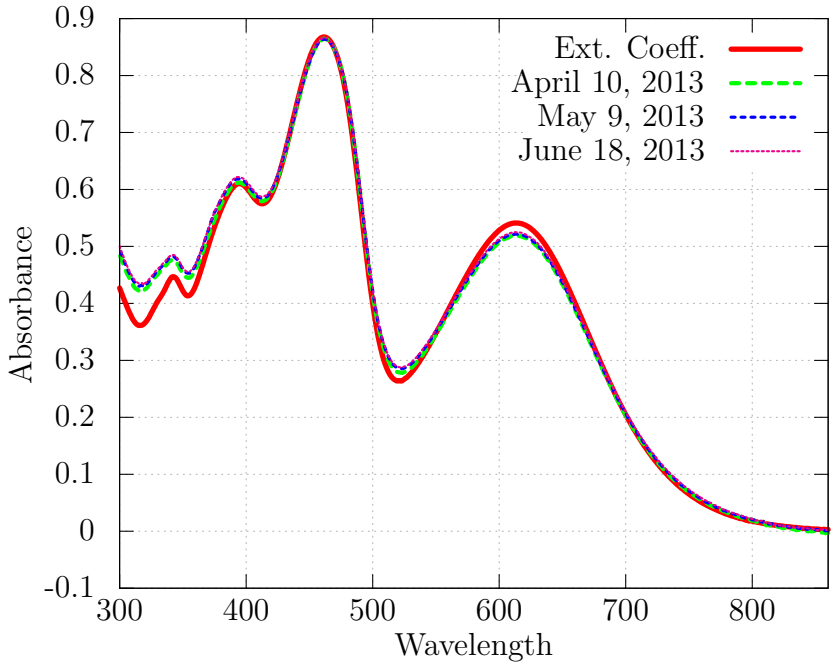

Figure 3.11: Comparison of the absorbance spectrum of a very weak concentration of molecule ISO-3 over a period of 2 months with the extinction coefficients. The important observation in this plot is that the shape of the absorption spectrum remains unchanged over a long period of time, and still closely matches the extinction coefficients.

3.3 Error Analysis

Several sources of error in a DFWM experiment can be eliminated (or their impact on the the experimental accuracy greatly decreased) by measuring quantities as ratios, with respect to a known quantity which eliminates the dependence on laser intensity, reflection losses, pulse timing, and slight geometric misalignments.

This section will analyze the impact of a misalignment of the incident pump beams on the measured DFWM signal. So far, this chapter has assumed that the forward DFWM geometry is such that the electric field amplitude (E_4) radiated by the polarization is built up in a phase matched way, $\mathbf{k}_4 = \mathbf{k}_1 + \mathbf{k}_2 - \mathbf{k}_3$, and $|\mathbf{k}_4| = |\mathbf{k}_1| = |\mathbf{k}_2| = |\mathbf{k}_3|$. However, if the incident beams are slightly misaligned, then the wave vector k_4 will not have the correct magnitude to satisfy the wave equation.

The DFWM signal can only be coherently amplified over a limited length, which is the coherence length (l_c) given by

$$l_c = \frac{\pi}{\Delta k} \tag{3.16}$$

where $\Delta k = \mathbf{k}_1 + \mathbf{k}_2 - \mathbf{k}_3 - \mathbf{k}_4$. When the beams are phase matched, $\Delta k = 0$ and $l_c = \infty$.

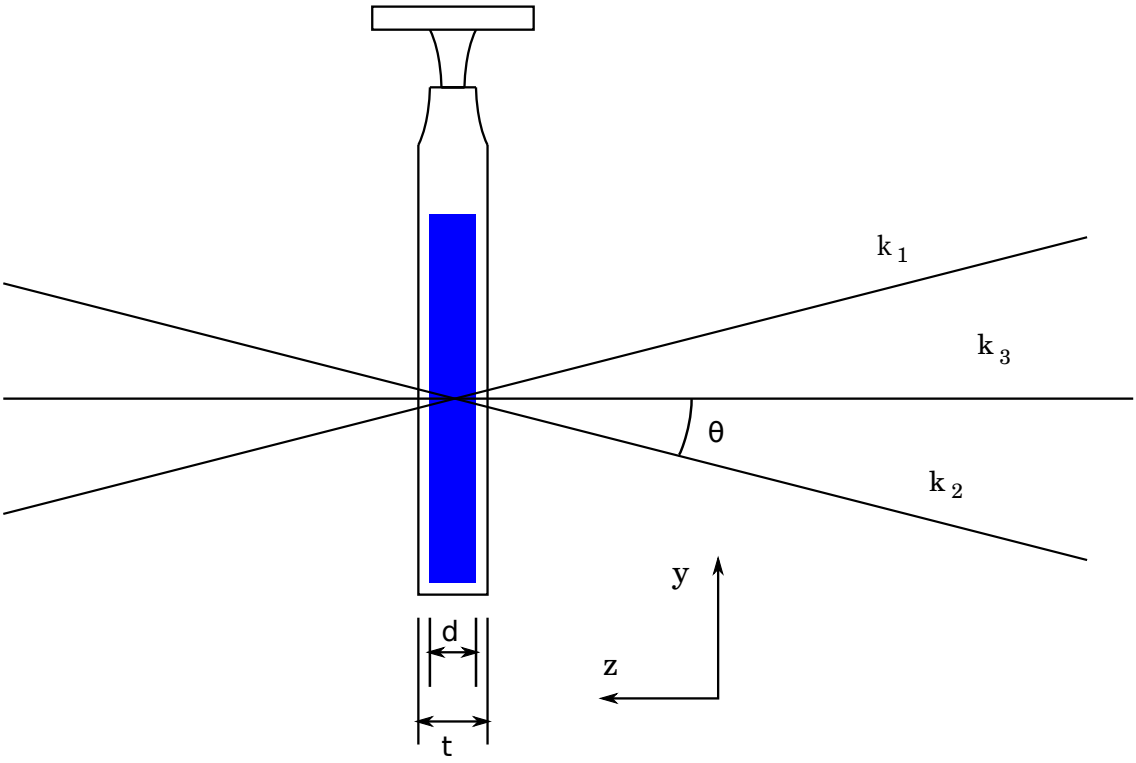

Figure 3.12: Side view of experimental setup, showing three beams crossing in the sample. The solution has a thickness d, but the glass cuvette has a total thickness of t.

When the beam $\mathbf{k}_3$ is misaligned, the components of the mismatch vector $\Delta\mathbf{k}$

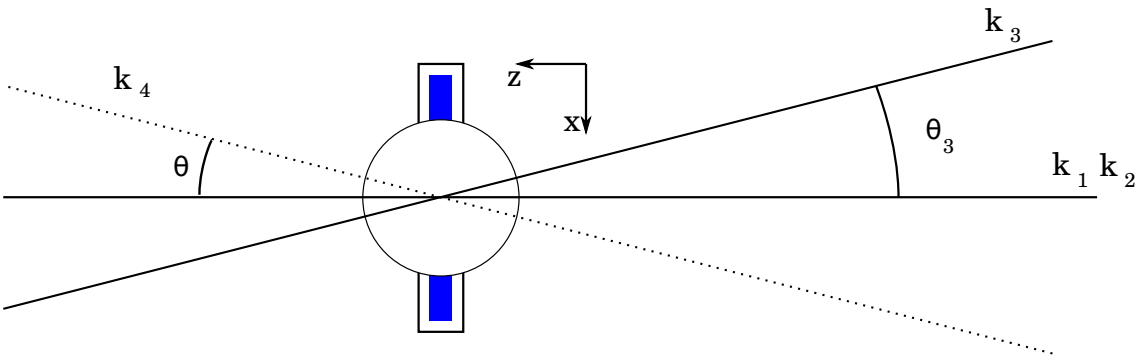

Figure 3.13: Top view of experimental setup, showing three beams crossing in the sample, and the direction of the DFWM signal. When properly aligned, all three incident beams cross at the same angle θ with respect to the z-axis.

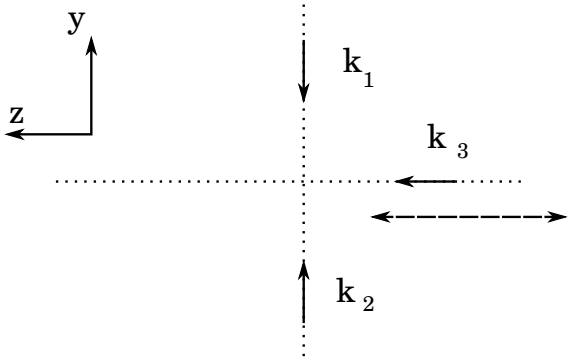

Figure 3.14: End view of experimental setup, showing the misalignment considered when $\mathbf{k}_3$ is at an angle $\theta_3 \neq \theta$.

are:

$$\Delta k_x = k_{1x} + k_{2x} - k_{3x} = 0 + 0 - k \sin\theta_3 \tag{3.17}$$

$$\Delta k_y = k_{1y} + k_{2y} - k_{3y} = -k \sin\theta + k \sin\theta - 0 \tag{3.18}$$

$$\Delta k_z = k_{1z} + k_{2z} - k_{3z} = k \cos\theta + k \cos\theta - k \cos\theta_3 \tag{3.19}$$

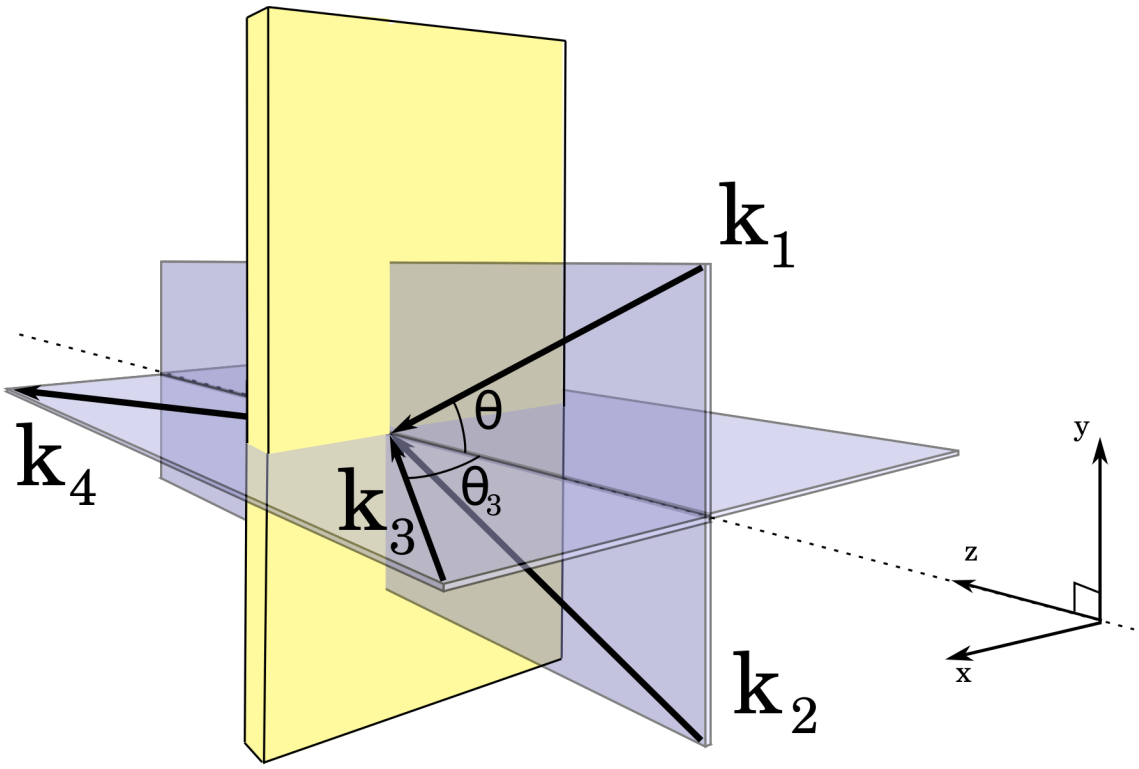

Figure 3.15: Perspective view of the DFWM geometry, showing the angle θ_3 of incident beam with wave vector k_3 in the xz plane.

so the size of this vector is

$$|\Delta\mathbf{k}| = k\left(1 - \sqrt{(\sin^2\theta_3 + (2\cos\theta - \cos\theta_3)^2)}\right) \tag{3.20}$$

If $|\Delta\mathbf{k}| \neq 0$, then $l_c \neq \infty$, and the intensity of the DFWM signal will grow as

$$I_{DFWM} \propto \sin^2\left(\frac{\Delta k z}{2}\right) \tag{3.21}$$

which would not introduce any error if the uknown sample under measurement and known reference have the same optical path length, but if they are different, then there could be error. There will always be error if the l_c is less then the thickness of the sample. The reference used to calibrate the DFWM measurements is a 1 mm

thick piece of fused silica (FS), which is compared to an optical cuvette with a 1 mm thick reservoir for the solution (d in Fig. 3.12), plus the thickness of glass (total thickness t in Fig. 3.12). Numerous measurements over the years have established that this ratio equals 6 when the geometry is correct. The average of the last 6 measurements is 5.963 ± 0.13.

This analysis will estimate the error introduced when the geometry is not correct, resulting in the z dependence of the DFWM signal to be different for the FS sample or the solution (DCM), and those samples have different thickness. Note that $\sqrt{I^{DCM}/I^{FS}} = 6$ is not the same as saying that the $\chi^{(3)}$ of DCM is 6 times greater then the $\chi^{(3)}$ of FS. The cuvette has a 1 mm path length of DCM, plus the walls of fused silica. Their contribution depends on the degree of spatial overlap from the 3 incident beams which makes this a more complicated problem. Consider a slightly simplified version of this experimental comparison, in which the DCM cuvette is simply twice as thick as the FS sample. It should still be possible get a sense of the amount of error introduced for a phase mismatch caused by an angular error in the experimental geometry.

Using measured values of the DFWM experimental setup, $\theta_3 = 0.0354$ rad, at $\lambda = 1500$ nm, and $n = 1.33$, it is possible to calculate the error introduced as a function of angular misalignment, for this slightly slimplified case. The simplification is that the FS sample has a thickness of 1 mm, and the DCM has a thickness of 2 mm.

In Fig. 3.16, the ratio $\sqrt{I^{DCM}/I^{FS}}$ is calculated as a function of angular misalignment. At perfect alignment, the ratio is 6, but the error increases as the deviation angle increases. At an angular error of about 0.009 rad, the mismatch results in no radiated wave from the polarization from the 2 mm DCM cuvette.

This comparison over-estimates the error introduced, because the DCM cuvette is actually 1 mm thick, plus 1 mm thick walls of FS. Since the $\chi^{(3)}$ of FS is less then that of DCM, the actual error should not be as large. This is a worst-case analysis.

For a sense of what misalignment would cause a 20% error which corresponds to an angular error of 0.002435 rad. Over a distance of 120cm, the position of the laser is off by 3mm (see Fig. 3.17). When the beam $\mathbf{k}_3$ was moved horizontally a

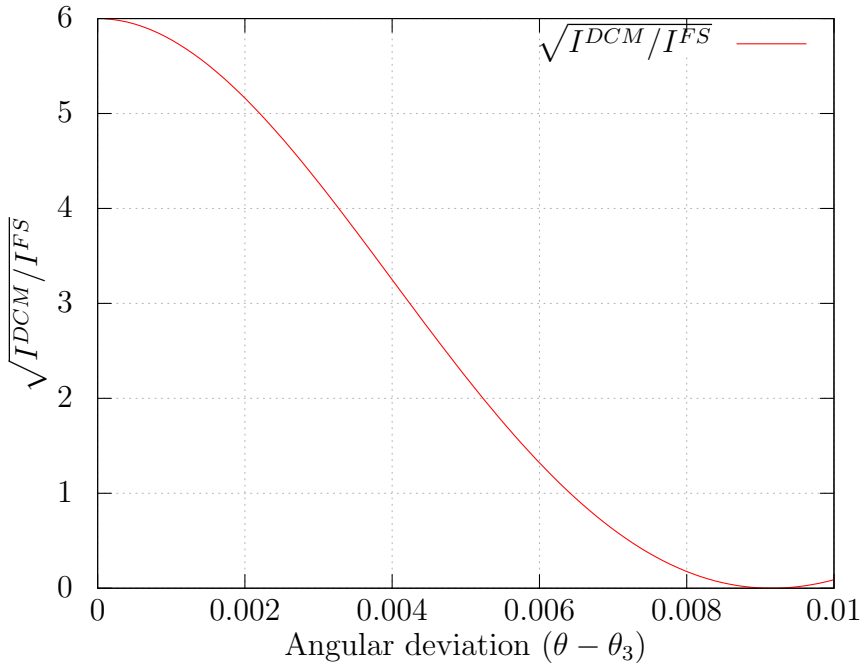

Figure 3.16: Calculated ratio of $\sqrt{I^{DCM}/I^{FS}}$ as a function of angular error of the incident beam $\mathbf{k}_3$.

distance of 6mm, a ratio of 4.7 was measured, or an error of about 22 %. So this analysis over-estimates the error.

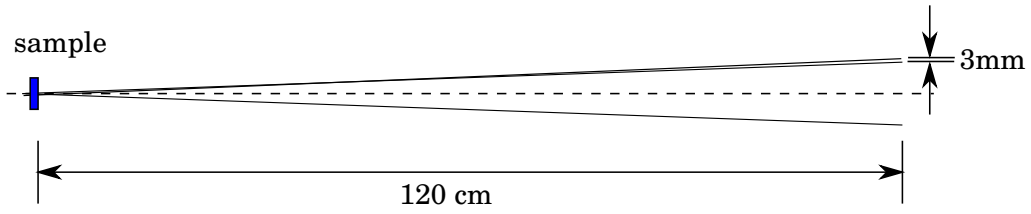

Figure 3.17: Geometry of incident beams, showing the 3 mm postioning error over 120 cm, that results in a 20% error in the worst case, when $t = 2d$ and the cuvette contains only DCM (solvent).

3.4 Spectroscopy of the third-order polarizability

This section presents the results obtained for two of the molecules presented in Fig. 3.2 on page 26. In each case, the linear absorbance spectrum (at twice the wavelength) is presented for comparison. Additionally, results from the time-dependence DFWM measurements at single wavelengths are plotted, usually at 1500 nm for comparison with the values obtained using the spectroscopy described here.

The TDMEE molecule has among the best polarizability per size of molecule ($\tilde{\gamma}$), but tends to form crystals in the solid state and the grain boundaries cause excessive losses due to scattering. However, it is the best example here of a molecule with one dominant absorption band in the optical range ($\lambda_{\max} = 591$ nm), and this makes it interesting to study spectroscopically (see Fig. 3.18). An unusual feature of this spectrum is that the real part reaches a most negative value at a wavelength nearly coincident with the peak imaginary part. This feature has been confirmed by other measurements [22].

The molecule C-3 has among the highest values for the figure of merits $\gamma_{\mathrm{I}} = 0.0045$, and specific $\tilde{\gamma} = 1.209$ which is about 50% better then DDMEBT. Larger values of $\tilde{\gamma}$ indicate that the molecule has a higher potential for forming solid state assemblies with large $\chi^{(3)}$ [6]. The peak TPA cross-section is not particularly high ($\mathrm{Im}[\gamma] \approx 10$), which is common when the linear absorbance spectrum shows two comparable absorption bands (in contrast to TDMEE). In equation 2.4, the maximum value of γ_k^{res} occurs when $E_{20} = E_{10}$.

The real part of γ shows a characterstic shape, which reaches its most negative value at higher photon energies than the maximum in the imaginary part. The data also suggests a mild resonant enhancement of the value measured at 1500 nm, which is at the very edge of the imaginary part that starts to increase sharply below 1500 nm (see Fig. 3.19).

Table 3.1 summarizes on-resonant values for TDMEE, DDMEBT, and C-3, and the two-photon absorption cross-sections and specific TPA cross-sections are compared to AF-50 and **103** from Ref. [23] which have been specifically designed to achieve very large two-photon absorption cross-sections. Note that TDMEE has a

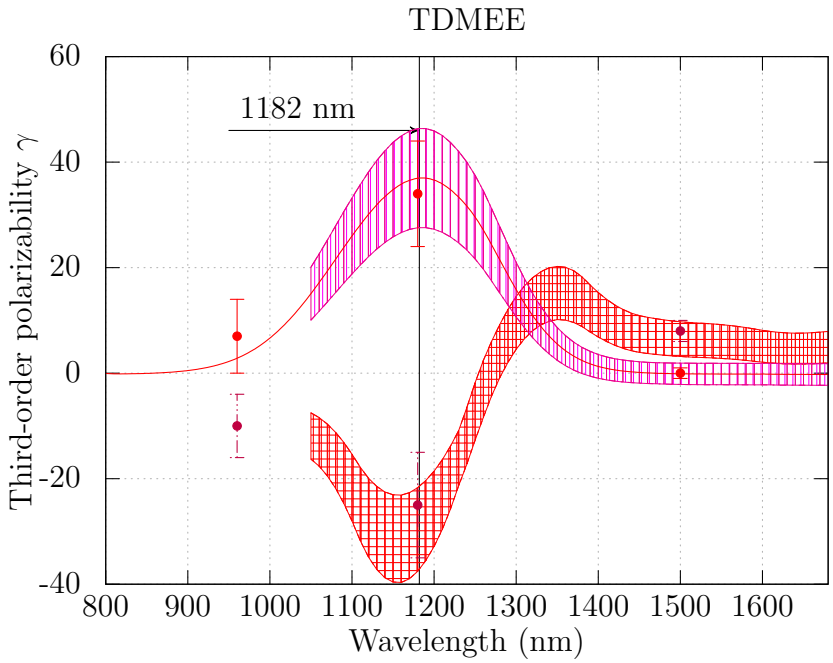

Figure 3.18: Spectroscopy of the first TPA transition of TDMEE. The solid line is the linear absorbance spectrum plotted at twice the wavelength. The band with the vertical stripes is the imaginary part, and the band with the cross-hatches is the real part of γ. In both cases, the thickness of the band represents the approximate error. TDMEE has a linear absorbance peak at 591 nm, and a peak in the imaginary part (which is related to two-photon absorption) is observed at 1182 nm.

very high TPA cross section, comparable to some of the largest in the literature. Most significantly, it achieves this very large TPA cross-section with a much smaller size molecule, leading to an extremely large specific TPA cross-section ($\tilde{\sigma}$), three times larger then molecule **103** from Ref. [23].

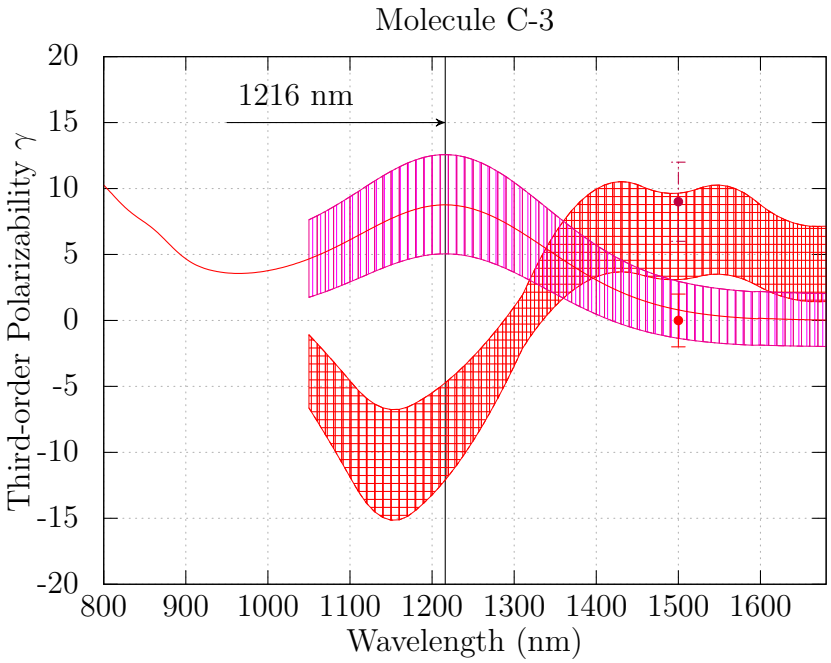

Figure 3.19: Spectroscopy of the first TPA transition of C-3.

Table 3.1: On-resonant properties of TDMEE, DDMEBT, and C-3. The value $\gamma_k^{\text{res}}/\gamma_k$ is from equation 2.40, the ratio of the imaginary part on-resonance to the real part off-resonance, as calculated in the fundamental limit, with estimates for Γ_{10} and values for E_{10} and E_{20} from the linear absorbance spectrum. The value γ_k^{res} is the fundamental limit of the imaginary part, on-resonance. The value γ^{res} is the experimentally determined value of the imaginary part, on-resonance, from the spectroscopic data. The value $\gamma_I^{\text{res}} = \gamma^{\text{res}}/\gamma_k^{\text{res}}$ and gives a relative measure of how close the molecule is to the fundamental limit on resonance. The value σ is given in units of Göppert-Meyer (G.M.). The final value is the specific TPA, which is calculated by σ/M where M is the mass of the molecule in kg, which gives a relative measure of the TPA cross-section per size of molecule.

Molecule	$\gamma_k^{\text{res}}/\gamma_k$ -	γ_k^{res} $[10^{-48}\ \frac{\text{m}^5}{\text{V}^2}]$	γ^{res} $[10^{-48}\ \frac{\text{m}^5}{\text{V}^2}]$	γ_I^{res} -	σ [G.M.]	$\tilde{\sigma}$ [G.M. /kg $*10^{25}$]
TDMEE	8.371	5541	35	0.0063	284	69.5
DDMEBT	6.249	6158	25	0.0041	256	37.1
C-3	7.485	15076	10	0.0007	76	10.3
AF-50	-	-	-	-	30	2.6
103	-	-	-	-	275	22.5

Chapter 4

Donor-Acceptor Substitution: The Influence of Variability in the Donor/Acceptor Groups and Molecular Geometries on the Off-resonant Third-order Polarizabilities

The aim in creating molecules suitable for applications discussed in Chapter 1 involves designing their structure to have good non-linear optical properties, and then translating those desirable characteristics to the solid state. In order for a material to be able to mediate light-light interactions, it must have a large $\chi^{(3)}$, sufficent for one pulse to turn on or off another pulse via refractive-index modification, (cross-phase modulation) for example. Furthermore, it should have good optical quality and low loss, which requires a material free from defects and scattering. Also, it should not absorb energy from the optical waves, as heating of the material would become a problem.

One way to make the off-resonant third order polarizability (γ_{rot}) larger for a molecule is to make the molecule larger. However, because the $\chi^{(3)}$ of a solid state material is related to the γ_{rot} of the constituent molecules through the number density, the optical response of the larger molecules will be diluted because the number density would become smaller. Another problem with larger molecules is that the energy of the first optical transition (E_{10}) becomes lower (particle in a wide box), leading to more linear absorption, and the possibility of more two-photon absorption.

On the other hand, designing smaller molecules with potentially large number density in the solid state also leads to a host of issues. The main problem is that the energy of the first excited state becomes very large, and the third order non-linear optical response decreases dramatically, as the theoretical limit depends inversely on $(E_{10})^5$.

It may seem that we are stuck trying to balance between these two limits, but there is a way to obtain the performance of the large molecules in a small molecules. Donor-acceptor substitution allows for the tuning of the first optical transition independently from the size of the molecule.

Donor-acceptor substitution uses chemical groups with high electron affinity on one end of a system of $\pi - \pi$ conjugated electrons, and low ionization potential on the other. The de-localized π system allows electrons to be pulled easily from the donor, to the acceptor. As a result, the molecule has a permanent dipole moment in the ground state, but more importantly it lowers the HOMO-LUMO energy gap, which is a charge-transfer transition. Examples of donor and acceptor groups are shown in Fig. 4.1 and Fig. 4.2 respectively.

The strength, number, and location of the donor or acceptor groups can be varied, to tune the optical transition and optimize the non-linear optical response. This chapter will review several variations in the structure of donor-acceptor substituted molecules in the zero-frequency limit where the third-order polarizabilities can be properly compared to each other.

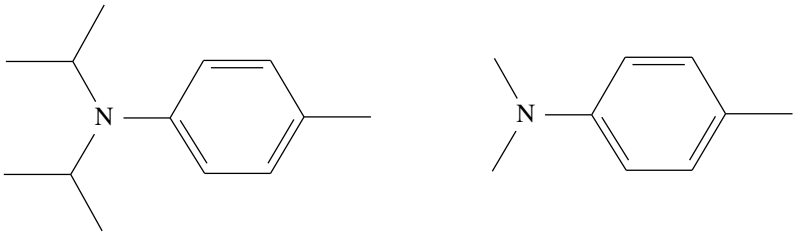

Figure 4.1: Examples of donor groups, diisopropylamino on the left, and dimethylamino on the right.

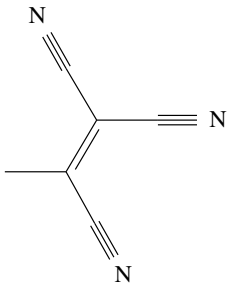

Figure 4.2: Example of three acceptor groups connected together.

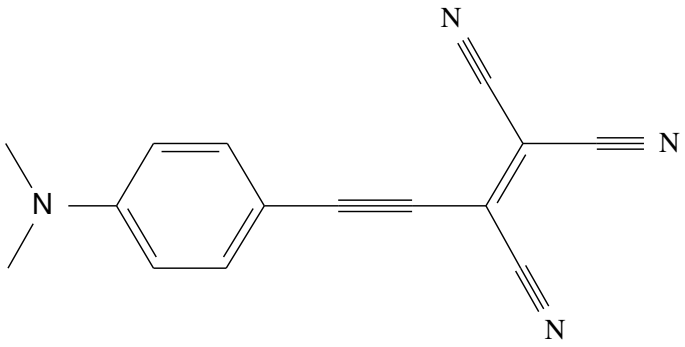

Figure 4.3: The TDMEE molecule, showing the donor and acceptor groups, with a system of conjugated π electrons in between.

4.1 Relevant Figures of Merit

Two good ways to place experimentally determined third-order polarizabilities in context is to compare them to the size of a molecule, as is done by evaluating

the *specific third-order polarizability* [24], and to compare them to the maximum nonlinear response that a molecule could have by using intrinsic hyperpolarizabilities [25].

The specific third-order polarizability is defined as:

$$\tilde{\gamma} = \frac{\gamma_{\text{rot}}}{M} \tag{4.1}$$

where γ_{rot} is the experimentally determined value, and M is the molecular mass that provides an approximate measure of the size of a molecule.

The upper limit to the third-order polarizabilities of a molecule (γ_k) has been discussed in Chapter 2 (see equation 2.36 on page 16).

The intrinsic gamma is a unitless quantity defined as

$$\gamma_I = \frac{\gamma_{\text{rot}}}{\gamma_k}, \tag{4.2}$$

which provides a relative measure of the efficiency of a molecule with respect to the fundamental limit.

4.2 Varying Donor-Acceptor Substitution Around a Compact Conjugated System

The following molecules feature variations in structure including the type and location of the donor and acceptor groups, as well as the conjugated system of π electrons involved in the charge transfer. For example, the K-x molecules are characterized by "homoconjugated push-pull systems" [26]. The C-x molecules are unique in that there are two main charge-transfer transitions between one of the two methylamino donor groups, and one of the CN acceptor groups [27]. These two transitions can be observed as two distinct peaks in the linear absorption spectrum. Notably, C-4 has only one dimethylamino donor group, and the the second highest optical transition is dramatically shifted towards shorter wavelengths. (See Fig. C.3 on page 91 in Appendix C.) Note that some of the C-x molecules form *cis/trans* isomers which is

described in more detail in Ref. [27].

The T-x molecules vary the points of attachment of donor groups along the conjugation. One effect of the additional donor group in T-2 can be observed as a lower energetic first optical transition.

The J-x molecules utilize ferrocenyl groups as donors, and show that different types of donor groups can be used effectively to obtain good values for the third-order polarizability γ.

The third-order polarizability of the molecules in Fig. 3.2 on page 26 were measured with DFWM at a wavelength of 1500 nm. Because the peak of the lowest energetic transition in the optical range ($\lambda_{\max}$) is less then 650 nm, and the tail of the absorption peak is very weak at 750 nm, it is expected that these values for γ_{rot} are not significantly resonantly enhanced. There was no evidence of TPA during the measurements.

There are some observations that can be made from this wide assortment of molecular variations. First the molecules K-1 through K-4 had such small values of γ_{rot} that they were almost not measureable. The molecule K-5 is very similar in structure to K-1 through K-4, except it is has a conjugated π bond between two molecular end groups which is responsible for a much lower $\lambda_{\max}$ and a value for γ_{rot} very close to DDMEBT. However, in terms of $\tilde{\gamma}$, K-5 is only half as high as DDMEBT because the molecule weighs almost twice as much as DDMEBT.

From an efficiency standpoint, the K-5 molecule is not remarkable. It has a relatively weak, low-energy, but very wide optical transition (see Fig. C.2 on page 90) in contrast to an efficient molecule like TDMEE, T-1, or T-2, which features one strong and narrow transition (see Fig. C.1 on page 89).

Both the T-1 and T-2 molecules have the highest values of γ_{rot} at 1500 nm of these molecules. The bond structure of both of these molecules extends somewhat into each dimension, which has been shown to reduce the $\pi - \pi$ interaction between molecules in the solid state, and allow for the formation of good optical quality thin films with low scattering losses [6].

Also, the T-1 and T-2 molecules have a higher γ_{rot} then TDMEE, despite not

Table 4.1: Molecular and non-linear off-resonant properties of the molecules presented in Fig. 3.2.

Molecule	Mass $[\frac{\text{g}}{\text{mol}}]$	N_π -	λ_{max} [nm]	ϵ @ λ_{max} $\frac{1}{\text{mol}\times\text{cm}}$	γ_k $[10^{-48}\ \frac{\text{m}^5}{\text{V}^2}]$	γ_{rot} $[10^{-48}\ \frac{\text{m}^5}{\text{V}^2}]$	γ_{I} -	$\tilde{\gamma}$ $[10^{-23}\ \frac{\text{m}^5}{\text{V}^2\text{kg}}]$
TDMEE	246.3	16	591	36990	662	8±1	0.0121	1.956
DDMEBT	416.5	26	527	44856	985	6±1	0.0061	0.868
T-1	276.4	16	567	54077	538	11±2	0.0204	2.397
T-2	301.3	18	610	63998	981	11±2	0.0112	2.198
K-1	372.2	18	529	2555	481	1±1	0.0021	0.162
K-2	386.2	18	541	1567	538	1±1	0.0015	0.125
K-3	397.2	20	528	6945	589	1±2	0.0027	0.243
K-4	512.4	18	539	3671	528	1±2	0.0038	0.235
K-5	795.9	26	625	3070	2311	5±2	0.0024	0.416
C-1	420.2	26	616	37386	2150	6±2	0.0028	0.860
C-2	470.2	30	602	23641	2552	7±2	0.0027	0.896
C-3	448.2	26	608	35065	2014	9±2	0.0045	1.209
C-4	377.2	26	619	47764	2203	5±2	0.0023	0.798
J-1	546.2	38	627	6908	5018	3±2	0.0006	0.331
J-2	481.3	32	612	6817	3153	4±2	0.0013	0.500
J-3	481.3	32	528	33008	1507	5±2	0.0033	0.626

having a triple-bond backbone between the acceptor and donor groups. This indicates that both types of conjugated systems are suitable for non-linear optics. By varying the number of CN acceptor groups, and moving them to slightly different locations on the backbone of the molecule, the authors of Ref. [28] are able to identify multiple charge-transfer (CT) transitions between the donor and acceptor groups.

The λ_{max} for TDMEE (591 nm) lies almost exactly between the λ_{max} for each λ_{max} of T-1 (567 nm) and T-2 (610 nm). The additional CN group in T-2 lowers the energy of the lowest optical transition, as would be expected because it is an additional acceptor group.

These T-x molecules are interesting because they are less planar then TDMEE,

maintain the small size of TDMEE, and still improve on the γ_{rot} by nearly an additional 50%. This increase in non-linearity without an increase in size makes their $\tilde{\gamma}$ remarkable. They possess among the largest non-resonantly enhanced $\tilde{\gamma}$ measured in our lab. Only a few molecules have exceeded 2.0 without aid of resonant enhancement.

The C-1 through C-4 series of molecules are likely the best candidates in this thesis to meet or exceed properties of DDMEBT in the solid state. Each molecule has a $\tilde{\gamma}$ comparable to DDMEBT, and C-3 is notably almost 50% higher. These molecules have produced highly reflective optical thin films, and preliminary investigations indicate that they are also of very good optical quality.

The molecules J-1, J-2, and J-3 incorporating ferrocene as an alternate donor group, but these molecules did not exceed DDMEBT in any metric. The molecules J-1 and J-2 could be vapor deposited into high optical quality thin films [6] [29] with optical qualities such as loss and $\chi^{(3)}$ comparable to the DDMEBT films.

In conclusion, conjugated π electrons are essential to having a molecule with a large non-linear response. Several different strategies for achieving a charge transition across the conjugated π electrons can be effective, including either multiple transitions, or even a broken conjugation (C-x molecules), and the use of triple or double bonds. Different chemical donor and acceptor groups can be used (K-5), in different places on the molecule (T-1 and T-2) to achieve the same effect of relatively large non-linearities in small molecules.

However, in order to better understand the physics of optimized donor-acceptor substituted molecules and quantify the influence of these design choices, a systematic study is needed to modify one parameter in a family of molecules. The next chapter describes how the non-linear response depends on the number of triple bonds in the spacer between the donor and acceptor groups and explains the physics involved.

Chapter 5

The Effect of the Size of the Conjugated System on Third-order Nonlinear Optical Properties: A Systematic Study

The previous chapter showed that donor-acceptor substitution works as a way of achieving a large third-order optical response from small molecules. However, the question still remains of how far this can be scaled to larger molecules, with longer conjugated systems.

Studies of variations of the off-resonant third-order polarizabilities when changing the size of the conjugated system between the donor and acceptor groups have been published in Ref. [30] but in that study both size and geometry of the conjugated system changed, and only over a limited range. To isolate the effect of varying the geometric distance between donors and acceptor groups while keeping the geometry and structure of the conjugated system constant, we decided to concentrate on molecules where the conjugated system consists of just one single linear chain of carbon atoms attached to each other by single and triple bonds. An earlier attempt to extend a one-dimensional conjugated system between a donor and an acceptor

group has been published in Ref. [2] but the results were inconclusive because of difficulties related to the stability of the molecules synthesized for that study. Here, we will discuss the first complete and systematic study of the effects of variations of the length of a one-dimensional conjugated system on the third-order nonlinear optical properties. This study was achieved by (1) developing a new molecular family with the required stability and solubility properties and by (2) complementing third-order polarizability measurements at a single wavelength with a full nonlinear optical spectroscopy encompassing the zero-frequency limit as well as the first two-photon transition.

The molecular families for this study were developed starting with the DDMEBT molecule, whose robustness has been well-proven, and whose conjugated system separating donor and acceptor groups is basically a single triple bond. New molecules have been synthesized by our collaborators [1] with the conjugated system varied between zero triple bonds to 5 triple bonds. An encouraging hint that this could be done came from the fact that a 5-triple-bond compound very similar to this design had already been produced by our collaborators once and has been characterized as part of the studies presented in Ref. [2], showing a very large, mostly real-valued third-order nonlinearity of 60 ± 20 at the 1500 nm wavelength (see Fig. 5.1).

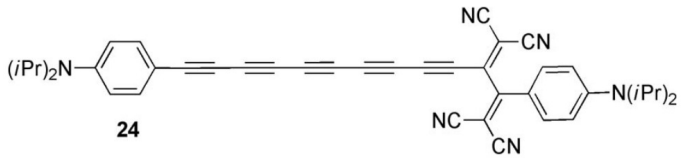

Figure 5.1: The molecule with a measured value of $\gamma_{\text{rot}} = 60 \pm 20$ in Ref. [2].

In combination with measurements of two other molecules similar to DDMEBT, but with 2 and 3 triple bonds (see Ref. [31]) of $\gamma_{\text{rot}} = 12 \pm 4$ and 21 ± 6 respectively, led to an initial conclusion that the donor-acceptor substituted molecules could be scaled up to at least 5 triple bonds, without any saturation due to over-extension.

The experimental spectroscopy in this work will show the on and off-resonant

behavior of the real part of γ, the dispersion of the imaginary part (which is related to the TPA cross section), relation to the linear absorbance spectrum, and connection of the dispersion to the dipole matrix elements of the first excited state transition. From the spectroscopy of the first TPA peak, it is possible to compare the experimental values with the fundamental limit for the imaginary part of γ, and from the off-resonant values of the real part, compare to the fundamental limits in the zero-frequency limit.

5.1 Two Families of Molecules

The successful synthesis and measurement of the 5-triple-bond molecule in Fig. 5.1 indicated that this molecule would be a suitable candidate for a complete study of the number of triple bonds. In August of 2012, a batch of molecules were successfully synthesized for us by the organic chemistry group at ETH-Zürich led by Professor François Diederich based on a similar structure to DDMEBT, but with diisopropylamino donors, and featuring $n = 0$ through $n = 5$ triple bonds in the acetylene spacer. These molecules shown in Fig. 5.2 will be referred to as ISO-0 through ISO-5 respectively.

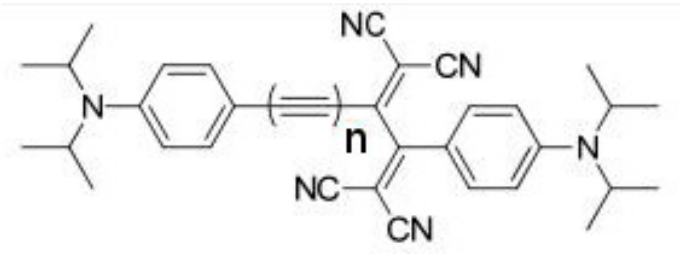

Figure 5.2: The family of molecules synthesized with $n = 0$ to $n = 5$ triple bonds in the acetylene spacer, with diisopropylamino donors, referred to as ISO-0 through ISO-5 respectively.

We also obtained a similar series of four molecules, but with dimethylamino donors featuring a variation of $n = 0$ to $n = 3$ triple bonds. They are shown in Fig.

5.3 and will be referred to as METH-0 through METH-3. We received small amounts of some of the molecules (between 24 mg and 50 mg), and initial measurements were plagued by trace acids in the solvent, but there was enough material to get good data.

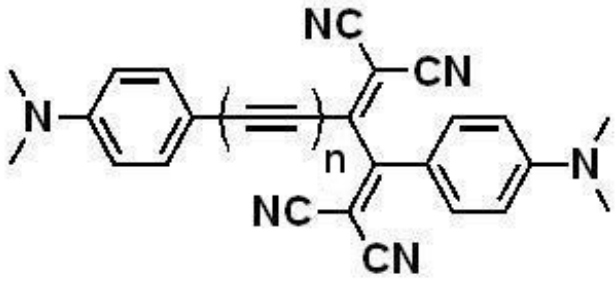

Figure 5.3: The family of molecules synthesized with $n = 0$ to $n = 3$ triple bonds in the acetylene spacer, with dimethylamino donors, referred to as METH-0 through METH-3 respectively.

5.2 Measurements at 1500 nm

The measurements of both families of molecules at 1500 nm is summarized in table 5.1. The results at this wavelength suggest that the molecules can be scaled up to at least to $n = 5$ triple bonds, and at that length the values for γ_{I} are among the highest measured in this study, and $\tilde{\gamma}$ is more than 3 times larger then any other molecule in this study.

Plotting the results in Fig. 5.6 shows that the measured values of γ_{rot} at 1500 nm can be fit with a power law with exponent of 1.8. This exponent is in marked contrast to non-D/A substituted molecules that have been found to scale with a power law of between 4 and 5 [4] [32].

In Ref. [3], the authors describe the synthesis of non-D/A substituted molecules long enough ($n = 22$) to identify a saturation point. Their molecules show a scaling of $\gamma \propto n^{2.46\pm0.1}$ which is a bit less than the polyyene oligomers in Ref. [4]. They

Table 5.1: Molecular and non-linear properties of the molecules presented in Fig. 3.2 as measured at 1500nm.

Molecule	Mass $[\frac{\text{g}}{\text{mol}}]$	N_π -	$\lambda_{\max}$ [nm]	ϵ @ $\lambda_{\max}$ $\frac{1}{\text{mol}\times\text{cm}}$	γ_k $[10^{-48}\ \frac{\text{m}^5}{\text{V}^2}]$	γ_{rot} $[10^{-48}\ \frac{\text{m}^5}{\text{V}^2}]$	γ_{I} -	$\tilde{\gamma}$ $[10^{-23}\ \frac{\text{m}^5}{\text{V}^2\text{kg}}]$
ISO-0	504.67	24	482	67920	537	2±1	0.0037	0.239
ISO-1	528.69	26	541	49759	1123	6±6	0.0053	0.683
ISO-2	552.71	28	586	35613	1943	15±5	0.0077	1.634
ISO-3	576.73	30	614	27053	2817	30±10	0.0107	3.133
ISO-4	600.75	32	628	22596	3587	60±20	0.0167	6.015
ISO-5	624.78	34	631	17112	4147	80±30	0.0193	7.711
Meth-0	392.4	24	470	62114	474	2±1	0.0042	0.307
Meth-1	416.5	26	526	44856	976	6±1	0.0061	0.868
Meth-2	440.5	28	570	33423	1692	12±5	0.0071	1.641
Meth-3	464.5	30	594	25989	2387	20±10	0.0084	2.593

identify a saturation near 60 carbon-carbon bonds, which corresponds to an "effective conjugation length" of 7.5nm. The red shift in linear absorption stops near $n = 10$ [3]. The conjugated system of the poly(triacetylene) molecules is not as similar to the conjugated system of the ISO-n and METH-n series, so the comparison with the polyyene oligomers in Ref. [4] and shown in Fig. 5.5 is more appropriate.

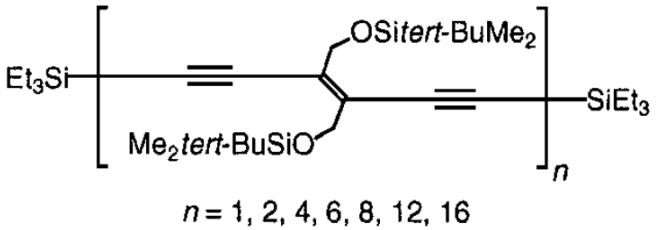

Figure 5.4: The family of poly(triacetylene) oligomers studied in Ref. [3]. Each repeat unit contains 2 triple bonds, and 1 double bond. This is counted as 3 conjugated units in each subsystem.

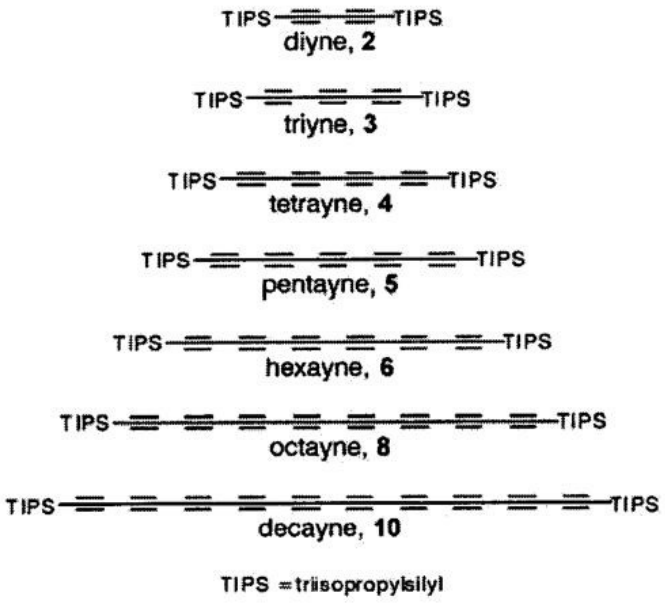

Figure 5.5: The family of polyyene oligomers studied in Ref. [4].

The power-law scaling with an exponent for the polyyne oligomers can be explained by examining the fundamental limit (see equation 2.36 on page 16). The maximum theoretical value for γ is proportional to N_π^2 and E_{10}^{-5} where N_π is the number of conjugated π electrons, and E_{10} is the lowest energy transition. The symmetric non-D/A molecules have a dramatic decrease in this energy with increasing spacer length (n). The authors of Ref. [4] identify a power law relationship of $E_{10} \propto n^{-0.379}$. This is similar to other symmetric polyyenes with power laws of $E_{10} \propto n^{-0.5}$ [33] [34]. Assuming that N_π scales linearly with n, this relationship then predicts a scaling law for non-D/A polyynes of

$$\gamma \propto \frac{N_\pi^2}{E_{10}^5} \propto n^{3.90} \tag{5.1}$$

using the $E_{10} \propto n^{-0.379}$ scaling law found in Ref. [4]. The predicted scaling of $\gamma \propto n^{3.90}$ is close to their measured power law of $\gamma \propto n^{4.28}$. A relationship of $E_{10} \propto n^{-0.5}$ results in $\gamma \propto n^{4.50}$, which is consistent with other studies [32]. This

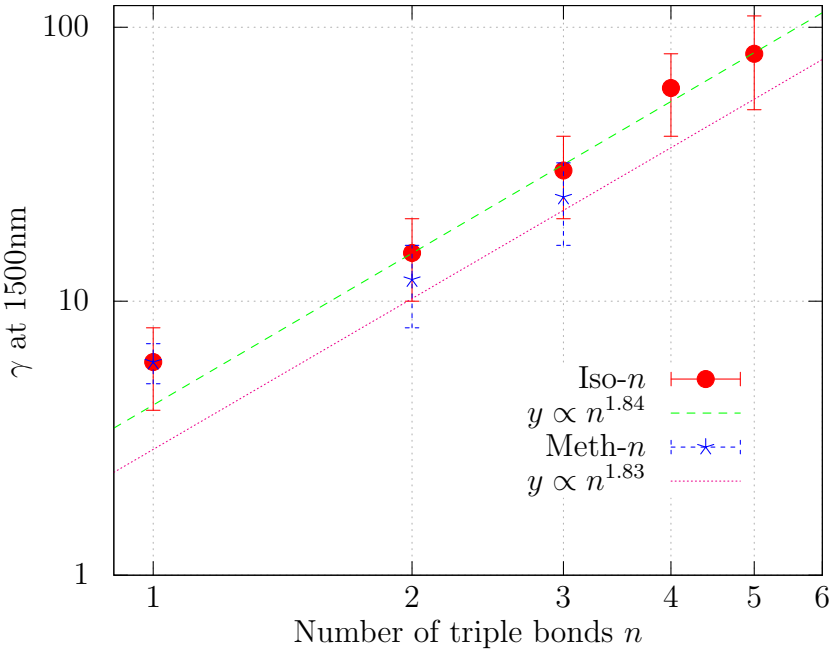

Figure 5.6: The values of γ_{rot} for both families of molecules (ISO-n and METH-n) as measured at 1500 nm plotted on a log-log scale and fit with a power-law function. Independent fits for each family result in virtually identical exponents (1.84 and 1.83). The diisopropylamino donors are slightly stronger than the dimethylamino donors and result in the ISO-n family of molecules having a slightly larger γ_{rot} for the same number of triple bonds.

shows that the experimental studies of the non-D/A substituted polyyenes follow the power law predicted by the fundamental limit of γ and the observed scaling of E_{10}.

This analysis also explains why the D/A substituted molecules do not follow the same power law scaling. For the ISO-n and METH-n molecules, the value for E_{10} does not scale in the same way. Instead, it can be fit with a power law of exponent -0.11 (see Fig. 5.7), resulting in a predicted scaling of $\gamma \propto n^{2.55}$, lower then predicted for the non-D/A substituted polyyenes.

A power law does not fit the the measured values of E_{10} perfectly. This was done to compare trends with the non-D/A substituted polyyenes and explain why the

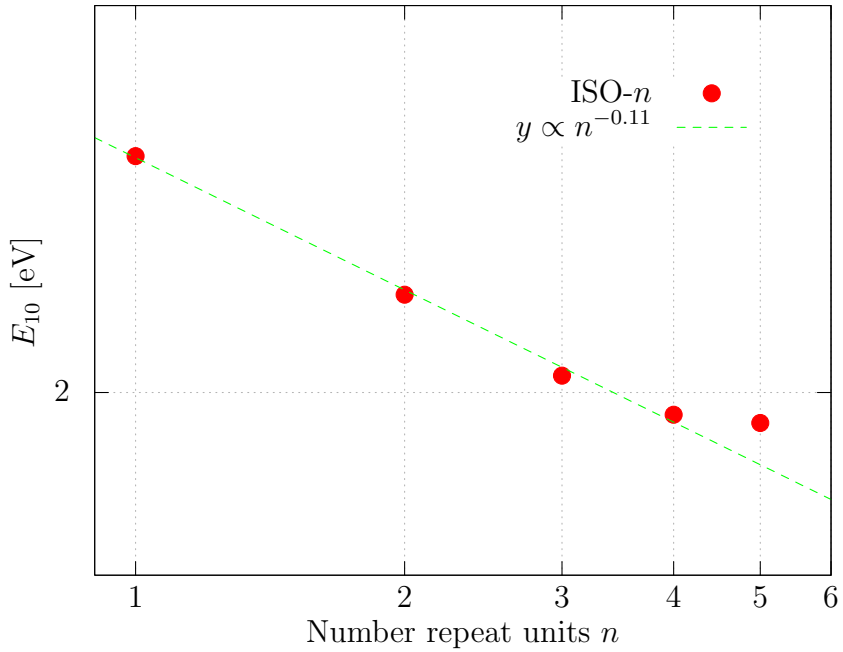

Figure 5.7: The values of E_{10} as a function of number of triple bonds n in the ISO-n series. The trend can be approximately fit with a power law of exponent -0.11. The data point at $n = 5$ was left out of the fit because the molecule is over-extended at this point.

third-order polarizability scales differently between the two, but still in accordance with the fundamental limit. These values for γ_{rot} are based on measurements at one wavelength, 1500 nm and may be resonantly enhanced which means that the fundamental limit for off-resonant values is no longer valid. A spectroscopic study can answer that question, and establish values for γ_{rot} off-resonance.

5.3 Zero-frequency Limit

Establishing the wavelength dependence of γ_{rot} in the range of photon energies from slightly above, to well below the first two-photon resonance allows determination of the mechanisms of resonance enhancement, as well as estimating the values off-resonance. The spectra of γ_{rot} are plotted in Fig. 5.8.

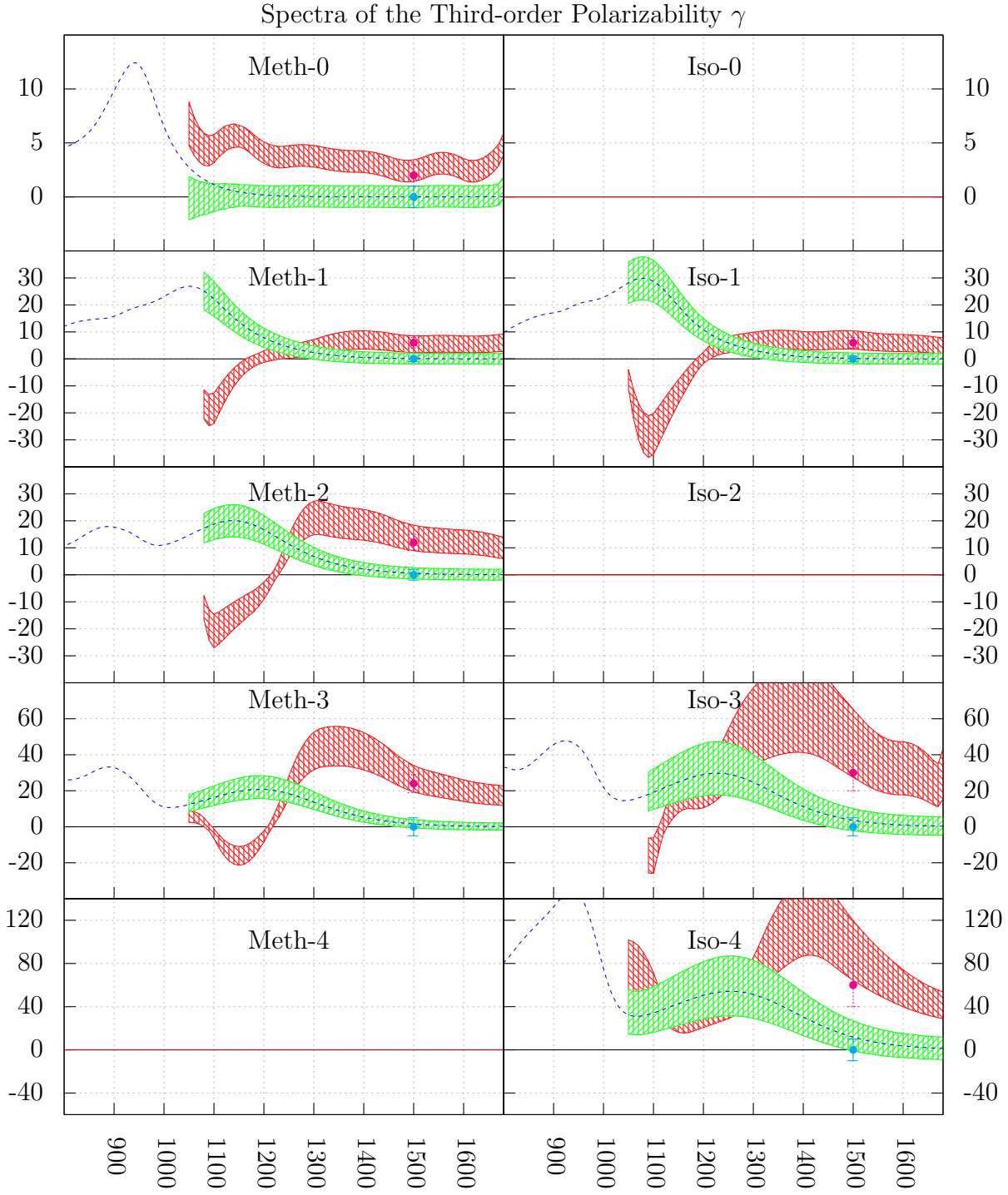

Figure 5.8: Collection of plots showing the wavelength dependence of the third-order polarizability γ for the molecules in Fig. 5.2 and 5.3. The vertical axis is γ in units of 10^{-48} m^5 V^{-2} and the horizontal axis is wavelength in nm.

Table 5.2: Molecular and non-linear off-resonant properties of the ISO-n and METH-n molecules, with values for γ_{rot} as determined to be off-resonant from the spectroscopy data.

Molecule	Mass $[\frac{\text{g}}{\text{mol}}]$	N_π -	λ_{max} [nm]	ϵ @ λ_{max} $\frac{1}{\text{mol}\times\text{cm}}$	γ_k $[10^{-48}\ \frac{\text{m}^5}{\text{V}^2}]$	γ_{rot} $[10^{-48}\ \frac{\text{m}^5}{\text{V}^2}]$	γ_{I} -	$\tilde{\gamma}$ $[10^{-23}\ \frac{\text{m}^5}{\text{V}^2\text{kg}}]$
ISO-0	504.7	24	482	67920	537	2±1	0.0037	0.239
ISO-1	528.7	26	541	49759	1123	6±2	0.0053	0.683
ISO-2	552.7	28	586	35613	1943	15±5	0.0077	1.634
ISO-3	576.7	30	614	27053	2817	24±10	0.0085	2.506
ISO-4	600.8	32	628	22596	3587	24±10	0.0067	2.406
ISO-5	624.8	34	631	17112	4147	20±10	0.0048	1.928
METH-0	392.4	24	470	62114	474	2±1	0.0042	0.307
METH-1	416.5	26	526	44856	976	6±1	0.0061	0.868
METH-2	440.5	28	570	33423	1692	12±5	0.0071	1.641
METH-3	464.5	30	594	25989	2387	20±10	0.0084	2.593

In table 5.2 the same figures of merit in table 5.1 are presented, but instead using values of γ_{rot} estimated to be off-resonant. The most significant result is that beyond three triple bonds, the values of γ_{rot} decrease in size. The values for γ_{rot} off-resonance are plotted in Fig. 5.9.

Table 5.10 provides a comparison of non-D/A substituted molecules, and the D/A molecules from Ref. [1] showing the specific third-order polarizability ($\tilde{\gamma}$) versus n, which gives a measure of how each design approach influences how the molecular third-order polarizability grows with the spacer unit between the donor and acceptor groups.

The physics of the saturation in γ_{rot} observed in these donor-acceptor molecules can be explained qualitatively by examining the frontier molecular orbitals and quantitatively by the dipole-matrix-transition elements.

The lowest energy optical transition is between the highest occupied molecular orbital (HOMO) and lowest un-occupied molecular orbital (LUMO). In these donor-acceptor substituted molecules, this transition is a charge transfer transition between

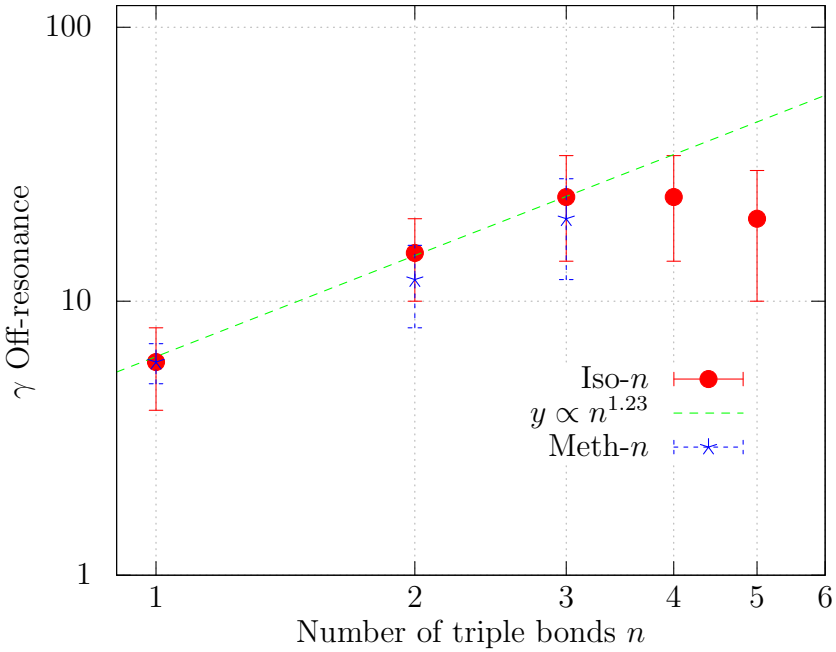

Figure 5.9: The values of γ_{rot} for both families of molecules (ISO-n and METH-n) as estimated to be off-resonant from the spectroscopic data plotted on a log-log scale. Most significant are the lower values for the longest molecules with $n = 4$ and $n = 5$ triple bonds. A power law fit to the ISO-1, ISO-2, and ISO-3 molecules results in an exponent of 1.23.

the acceptor and donor chemical groups. It is also the energy E_{10} that appears in denominator of the fundamental limit for the off-resonant third-order polarizability.

In the numerator of the SoS expression for γ are the dipole transition elements, and the most relevant one for the off-resonant third-order polarizability is the dipole transition element between HOMO and LUMO ($\langle H \mid \hat{p} \mid L \rangle$). In the limit $\langle H \mid \hat{p} \mid L$ tends towards zero, γ goes to zero.

In symmetric (non-D/A substituted) molecules, the electron density of each molecular orbital remains symmetric over the length of the molecule (see Fig. 5.11). The dipole transition elements $\langle H \mid \hat{p} \mid L \rangle$ do not get smaller as the molecule gets larger. The energy difference to the first excited state decreases, and the non-linear optical response (γ) gets larger as the molecule gets larger. The scaling with respect

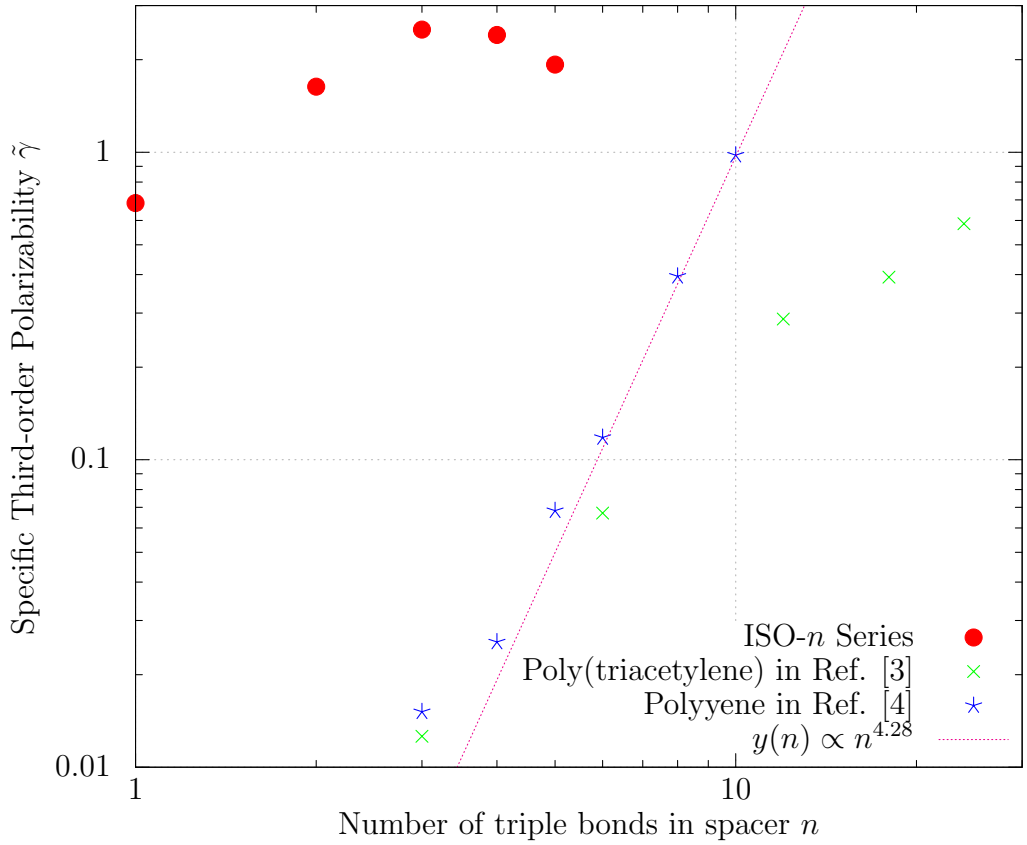

Figure 5.10: Comparison of the specific third-order polarizability ($\tilde{\gamma}$) versus number of repeated units. Note that the power power law for non-D/A substituted molecules is greater then the D/A molecules, but the D/A molecules reach a larger $\tilde{\gamma}$ with a few number of repeat units (n). Note that it is a log-log plot, and the best value for $\tilde{\gamma}$ among the D/A molecules is more then twice as large as the best non-D/A molecule presented here.

to number of repeat units (n) is shown in Fig. 5.10 and typically follows a power law with an exponent between 4 and 5 [4] [32].

In contrast to the symmetric molecules, donor-acceptor (D/A) substituted molecules suffer a reduction in the overlap matrix between the HOMO and LUMO orbitals, as the molecule gets too long. However, the energy difference to the first excited state for a small molecule is less then it would be for a non-D/A molecule, and consequently the non-linear response can be much larger. This design allows for small

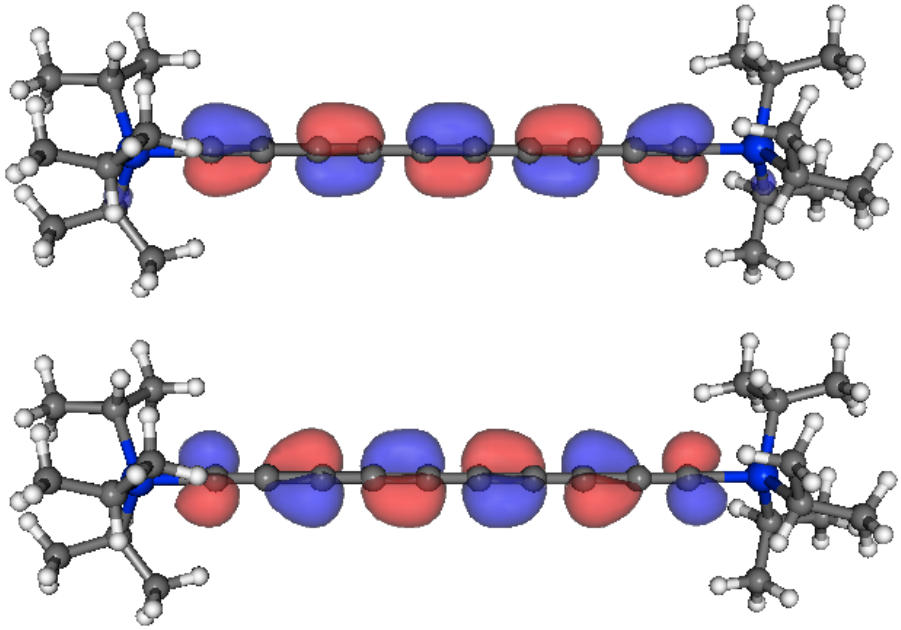

Figure 5.11: A symmetric molecule from the polyyene series studied in Ref. [4]. The HOMO orbital is on top, and LUMO is below. The symmetric molecule maintains a symmetric density of electrons in each orbital, the higher energy levels have additional nodes in the wave function. The orbital is plotted with an isosurface value of 0.040.

molecules, with a large γ, and consequently very large $\tilde{\gamma}$. But D/A substitution prevents the scaling of off-resonant values for γ with the number of repeat units beyond $n = 3$ for this series of donor-acceptor substituted molecules.

The results in table 5.3 are compared to a similar calculation using TD-DFT in [1]. The numbers are slightly different, but the trends are similar (see Figure 5.13). The sudden jump between ISO-2 and ISO-3 as calculated in this work are suspicious, and may possibly be attributed to insufficient geometry optimization or the formation of a different isomer of the molecule.

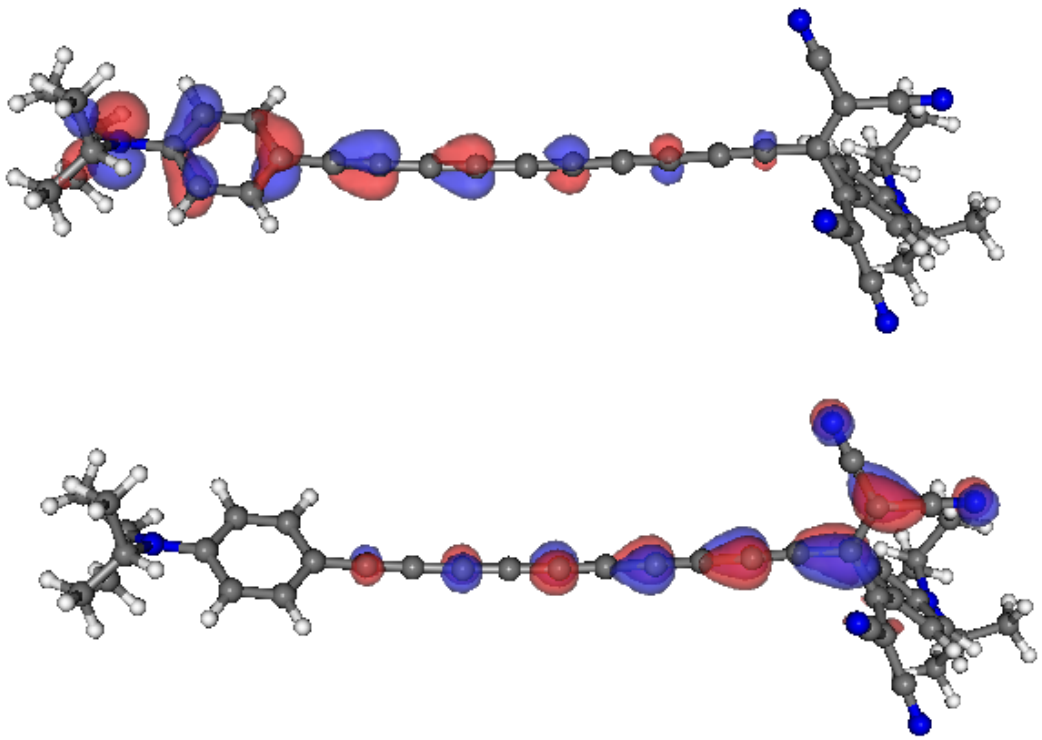

Figure 5.12: The ISO-5 donor-acceptor substituted molecule studied here. The HOMO orbital is on top, and LUMO is below. In the HOMO orbital, most of the electron density is concentrated on the donor group (left side of molecule), and in the LUMO orbital most of the electron density is concentrated towards the acceptor groups (right side here). This is typical of donor-acceptor substituted molecules, in the HOMO-LUMO transition (ground state to first excited state). The orbital is plotted with an isosurface value of 0.040.

5.4 Spectroscopy of the First Two-Photon Transition

The molecules in Fig. 5.2 and 5.3 were measured using the experimental methods and physical models described earlier in this work to determine the wavelength

Table 5.3: The calculated energy using B3LYP DFT for the first optical transition in units of eV, transition dipole norm in units of Debye calculated from a C.I. using B3LYP / 6-31(g,d), and the same as calculated in Ref. [1] using TD-DFT (DFT:CAM-B3LYP/6-31G* in Gaussian09)

Molecule	E_{HL}	$\langle H \mid \hat{p} \mid L \rangle$	$\langle H \mid \hat{p} \mid L \rangle$ from [1]
Iso-0	2.88	8.38	4.60
Iso-1	2.67	10.1	7.19
Iso-2	2.35	11.6	9.63
Iso-3	2.17	7.49	10.96
Iso-4	2.01	7.16	10.80
Iso-5	1.89	7.05	9.87

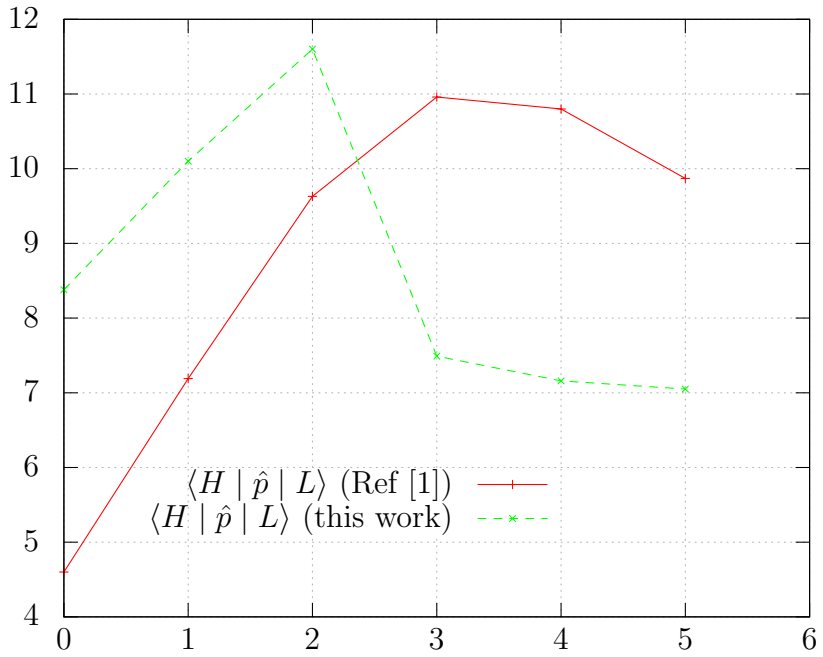

Figure 5.13: Comparison of the dipole transition elements for $\langle H \mid \hat{p} \mid L \rangle$ calculated with two different methods. Both show a maximum around $n = 2$ or $n = 3$, and then a decline with each additional triple bond in the spacer.

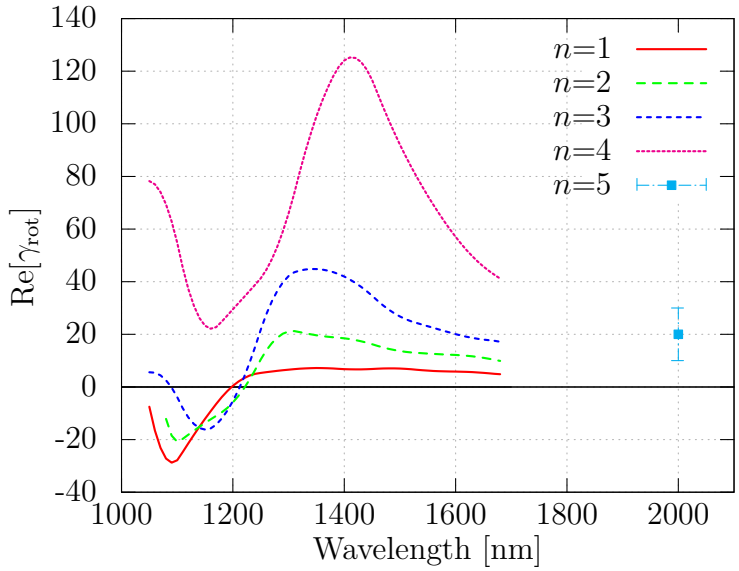

Figure 5.14: Comparison of the wavelength dependence of the real part of γ_{rot} as additional triple bonds (n) are added to the spacer between the donor and acceptor groups. Spectroscopic data was not obtained for the $n = 5$ molecule, so a single data point is plotted at 2000 nm where γ_{rot} was measured by time-dependent DFWM.

dependence of γ_{rot}. This study made the estimation of off-resonant values possible.

A comparison of four molecules is shown in Fig. 5.14 to show the degree to which the real part of γ_{rot} becomes increasingly resonantly enhanced as additional triple bonds are added to the acetylene spacer between the donor and acceptor groups. The spectrum of the METH-4 molecule in Fig. 5.8 shows that the resonant enhancement may be useful in applications. At a wavelength of 1500 nm γ_{rot} is significantly resonantly enhanced, but the imaginary part is still very small, so the resonant enhancement could be utilized in a region where the imaginary part is very small.

The spectroscopy also allows estimation of the peak TPA cross section for each molecule. The progression of the imaginary part of γ_{rot} as additional triple bonds are added is shown in Fig. 5.15. The peak imaginary value (at wavelengths between 1080 and 1680 nm) is smallest for n=2. This ISO-2 molecule also has two absorption

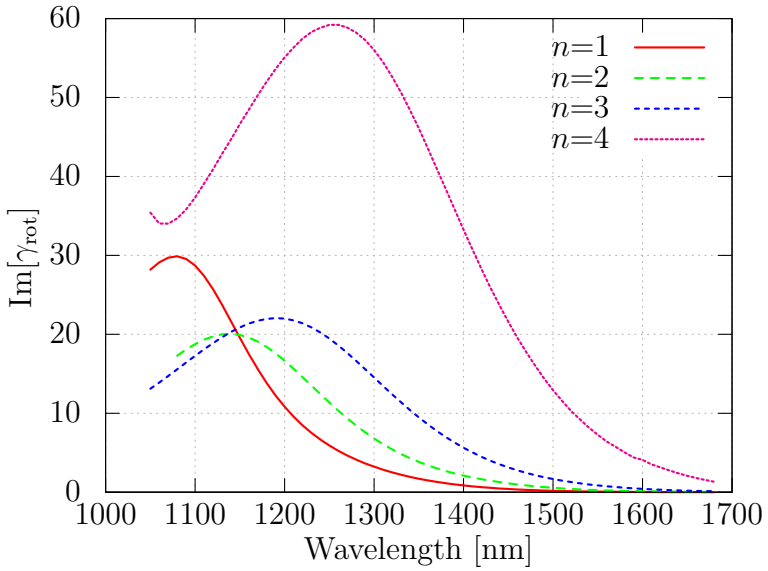

Figure 5.15: Comparison of the wavelength dependence of the imaginary part of γ_{rot} as additional triple bonds (n) are added to the spacer between the donor and acceptor groups.

peaks of approximately equal strength (see Fig. 5.16). Table 5.4 presents a summary of the values on-resonance.

This comparison of the peak TPA cross section to fundamental limits indicates that the longer molecules do not perform as well as the shorter ones, in terms of the figures of merit presented in table 5.4 (γ_I^{res} and $\tilde{\sigma}$). This trend can be related to the fundamental limits derived in Chapter 2. The plot in Fig. 2.4 shows the influence of the first two excited state transitions (E_{10} and E_{20}) on the limit of the imaginary part of γ on resonance, as taken from equation 2.40. It shows that the largest achievable Im[γ] occurs when $E_{10} = E_{20}$, and the width of the first transition (Γ_{10}) is narrow. However, as the ISO-n and METH-n molecules grow in size, a second absorption band becomes larger with the difference in energies ($E_{20} - E_{10}$) becoming larger, The width of the lowest energy absorption band also becomes wider (see Fig. 5.16). These factors may contribute to the reduction in the peak Im[γ]. The reduction in the dipole matrix elements would also be expected to reduce the peak Im[γ] because they appear in the numerator of the relevant terms in the SoS expression.

Table 5.4: On-resonant properties of the two families (ISO and METH) of molecules, compared with TDMEE. The value $\gamma_k^{\text{res}}/\gamma_k$ is from equation 2.40, the ratio of the imaginary part on resonance, to the real part off resonance, as calculated in the fundamental limit, with estimates for Γ_{10} and values for E_{10} and E_{20} from the linear absorbance spectrum. The value γ_k^{res} is the fundamental limit of the imaginary part, on resonance. The value γ^{res} is the experimentally determined value of the imaginary part, on resonance, from the spectroscopic data. The value $\gamma_I^{\text{res}} = \gamma^{\text{res}}/\gamma_k^{\text{res}}$ and gives a relative measure of how close the molecule is to the fundamental limit on resonance. The value σ is given in units of Göppert-Meyer (G.M.). The final value is the specific TPA, which is calculated by σ/M where M is the mass of the molecule in kg, which gives a relative measure of the TPA cross section per size of molecule.

Molecule	$\gamma_k^{\text{res}}/\gamma_k$ -	γ_k^{res} $[10^{-48}\ \frac{\text{m}^5}{\text{V}^2}]$	γ^{res} $[10^{-48}\ \frac{\text{m}^5}{\text{V}^2}]$	γ_I^{res} -	σ [G.M.]	$\tilde{\sigma}$ [G.M. /kg $*10^{25}$]
TDMEE	8.37	5541	35±10	0.0063	284	69.5
Iso-0	13.09	7036	-	-	-	-
Iso-1	5.63	6329	30±10	0.0047	290	33.0
Iso-2	12.17	23652	-	-	-	-
Iso-3	9.45	26628	30±10	0.0011	225	23.5
Iso-4	10.03	35981	50±10	0.0014	358	25.9
Iso-5	10.06	41729	-	-	-	-
Meth-0	12.20	5780	-	-	-	-
Meth-1	6.71	6551	25±10	0.0038	256	37.1
Meth-2	12.23	20691	20±10	0.0010	174	23.8
Meth-3	11.29	26947	20±10	0.0007	160	20.8

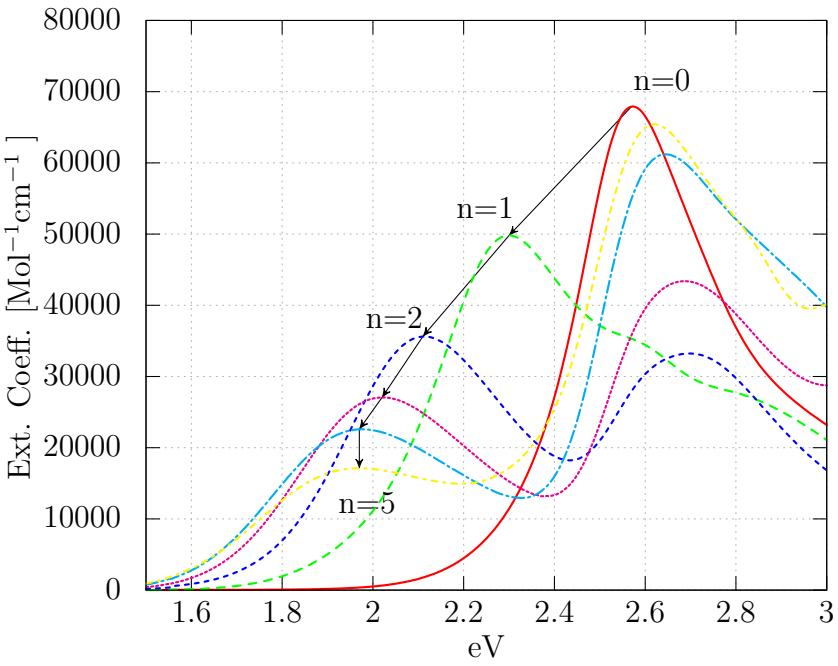

Figure 5.16: Comparison of the linear absorbance spectra for the ISO-n molecules, plotted in eV. Note that the lowest energy transition gets lower with each additional triple bond, until $n = 4$ and $n = 5$ have almost the same energy.

Chapter 6

Computational Chemistry

In theory, quantum mechanics provides the tools for obtaining exact solutions to physical observables, but in practice the expressions become too complex, the matrices become too large, or the differential equations are un-solvable with exact methods. The art of quantum chemistry is knowing which approximations to make, and being able to find more accurate solutions as perturbative corrections to simpler solutions. As computers evolve with larger memories and faster parallel processors, they become tools able to consider larger computations than could be done previously. However, there are still many choices to be made such as the level of theory and size of basis set [35].

In non-linear optics, there are great challenges to getting accurate compuational results, especially for the third-order polarization. Some good results have been obtained for small atomic and molecular systems (such as simple gases), but some theories that work well for some families of molecules, do not work as well for other molecules.

For the calculations presented here, the software package GAMESS was used which stands for General Atomic and Molecular Electronic Structure System [36] [37].

6.1 Geometry Optimization

The geometries of the molecules studied with computational chemistry were first optimized using Density Functional Theory (DFT) with the B3LYP hybrid functional, and the 6-31(g,d) basis set. For small organic molecules, this choice of theory and basis set is common, allowing for comparisons with other computational results of different molecules. Also, in her PhD thesis, Moonen did a very detailed analysis of the effect of these computational choices on the resulting optimized geometry, and found that B3LYP / 6-31(g,d) gave the best *quionoid character*, which is determined by the ratio of some bond lengths in the ring and stick structure of carbon bonds, such as found in the very center of the TDMEE molecule [38]. This geometry optimized value was found to be very close to the experimentally measured values found in the X-ray crystal structure of TDMEE.

There are some other basis sets like MIDI! that are specifically designed for geometry optimzation of small organic molecules, and the mean bond length difference was indeed better for this basis set, but the quinoid character was not better, so if the *shape* of the molecule is more important than the absolute size, then the choice made by Moonen seems to be a better one.

A geometry optimization was always performed before each calculation, except in the case of the molecules with up to 20 triple bonds. The initial coordinates were either obtained from a crystallographic file (if a crystallization was performed and measured by the chemists) or the molecule was drawn in Avogadro [39] [40] and a crude preliminary geometry optmization was performed using force field estimates based on bond lengths, before the final geometry optimization was done in GAMESS.

In the case of starting from coordinates obtained for crystallographic data, the geometry is far from the calculated equilibrium. When starting with manually drawn molecules initially optimized in Avogadro, the optimization in GAMESS would typically be closer to the final geometry, see Figure 6.1 for an example.

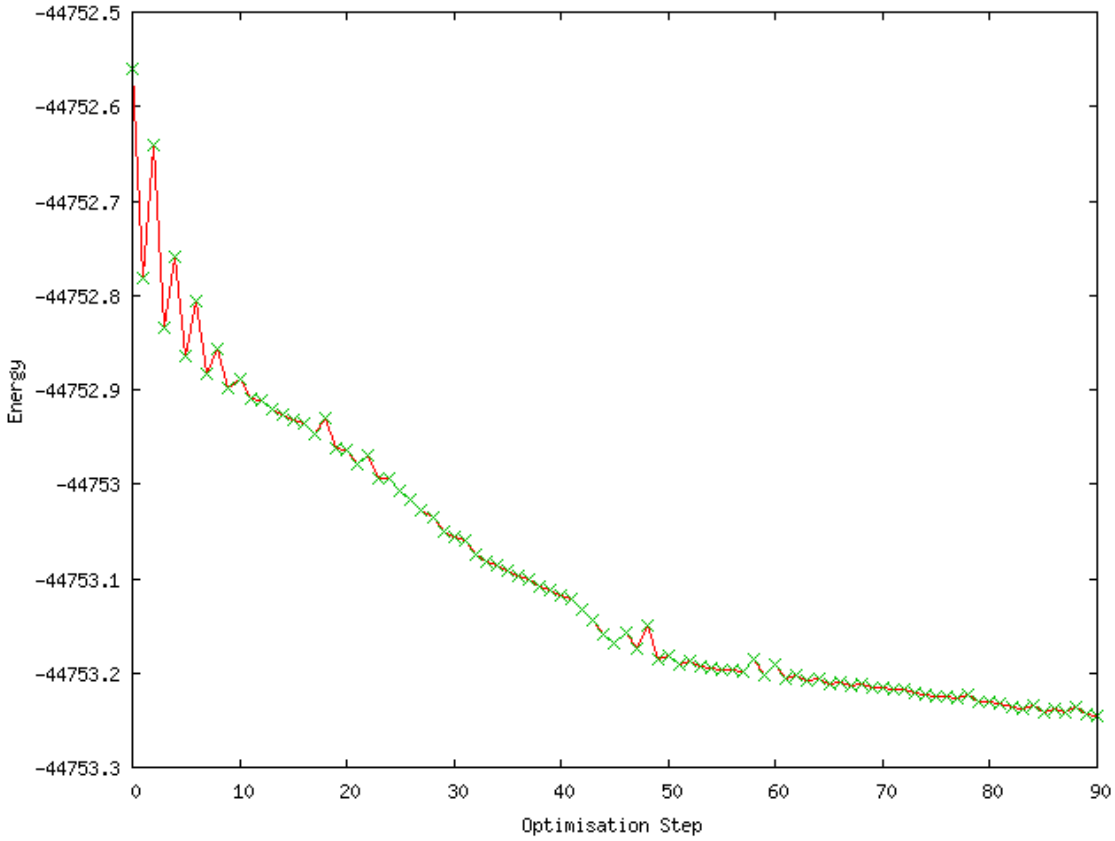

Figure 6.1: Calculated energy of ISO-1 for each iteration of the geometry optimization, starting with coordinates manually entered with the Avogadro software, and initially optimized with a force field estimate between atoms.

6.2 Energy

After the geometry optimization, the molecular orbitals can be determined with an energy calculation. Typically this is done with with the same level of theory and basis set as was used for the geometry optimization. The results of this run contain the energy eigenvalues for the molecular orbitals, and the coefficients of the basis set that can be used to view the 3D orbital surfaces at a selected iso-surface value.

6.3 Finite-Field Calculations of Third-Order Polarizabilities

The finite field method indirectly determines the first, second and third-order polarizabilities using two methods, and the results can be compared to make sure that the calculation has been converged to a tight enough tolerance. The third-order polarizability is significantly more challenging to determine accurately then the linear (α) and second-order polarizability (β) because it is much more sensitive to small differences in the wave function shape and energy. For example, electron correlation has a small effect on the dipole polarizability, but strongly affects the hyperpolarizability [41]. Considering even a small molecule of $CHCl_3$, the authors of Ref. [42] find that very large, diffuse basis sets are necessary to get good convergence. The resulting values are sensitive to the molecular structure, more so for the hyperpolarizability than the linear polarizability. The third-order polarizability would be expected to have even a greater sensitivity. The choice of basis set and convergence criteria are more critical to determine the changes in the energy and dipole moment accurately.

Several specific basis sets have been designed to model the whispy tails of the wave functions with better accuracy, and lead to better results for the second and third-order polarizabilities. Their performance with small molecules (HCN and HCP) has been compared favorably [43], but it is too computationally intensive for the large molecules studied here.

The two methods iteratively apply electric fields of different strengths to the molecule in different directions, and establish a relationship between applied electric field and energy, as well as dipole moment. The dipole moment is expressed as a Taylor expansion to third order as

$$\mu_{i,j} = \mu_{i,j}^{\text{static}} + \sum_k \alpha_{i,jk} E_k + \frac{1}{2!} \sum_{kl} \beta_{i,jkl} E_k E_l + \frac{1}{3!} \sum_{klm} \gamma_{i,jklm} E_k E_l E_m \qquad (6.1)$$

where $\mu_{i,j}^{\text{static}}$ is the permanent dipole moment. A similar expansion in energy

$$U = U_0 + \mu_i E_i + \frac{1}{2!}\alpha_{ij} E_i E_j + \frac{1}{3!}\beta_{ijk} E_i E_j E_k + \frac{1}{4!}\gamma_{ijkl} E_i E_j E_k E_l \qquad (6.2)$$

should give similar quantitative results for α, β, and γ as long as the calculations are converged sufficiently. If the results do not agree, then it is an indication that the convergence criteria should be tightened. To get good results for the polarizabilities, and especially for the higher order of the polarizabilities, it is important to use basis functions that allow for the accurate determination of the tails of the wave functions, so additional diffuse function were included in the basis set.

From these equations, the Finite Field method of GAMESS can determine 9 of the elements of the third-order polarizability.

Two sets of calculations were performed on geometry optimized coordinates of the ISO-n molecules, with $n = 0$ to $n = 5$. One set of calculations used the basic RHF calculations, and the second set used B3LYP DFT. Both used the same 6-31(g,d)++ basis set, with the ++ indicating additional diffuse basis sets. The results are plotted in figure 6.2 and compared to the estimated off-resonant values for each molecule.

Both sets of calculations indicate an increasing trend, beyond the experimental values that were estimated for off-resonant values from the spectroscopy data.

Additional calculations were performed to see if this trend calculated by the finite field method would continue with increasing values for γ as the molecule was made longer. Because geometry optimization would take prohibitively long for very big molecules, and to isolate the effect of the molecule length without allowing for the molecule to bend or twist, a set of synthetic molecules was created with a completely straight backbone, and the end groups were taken from a geometry optimized ISO-1 molecule. The RHF level of theory was used for this series of calculations because it is computationally faster, and the B3LYP level of theory appeared to overestimate the increase in γ with respect to n. Each molecule was aligned so that the acetylene spacer was placed directly on the z-axis, and the bond length alternation established from the Iso-5 geometry optimized molecule was continue up to $n = 20$.

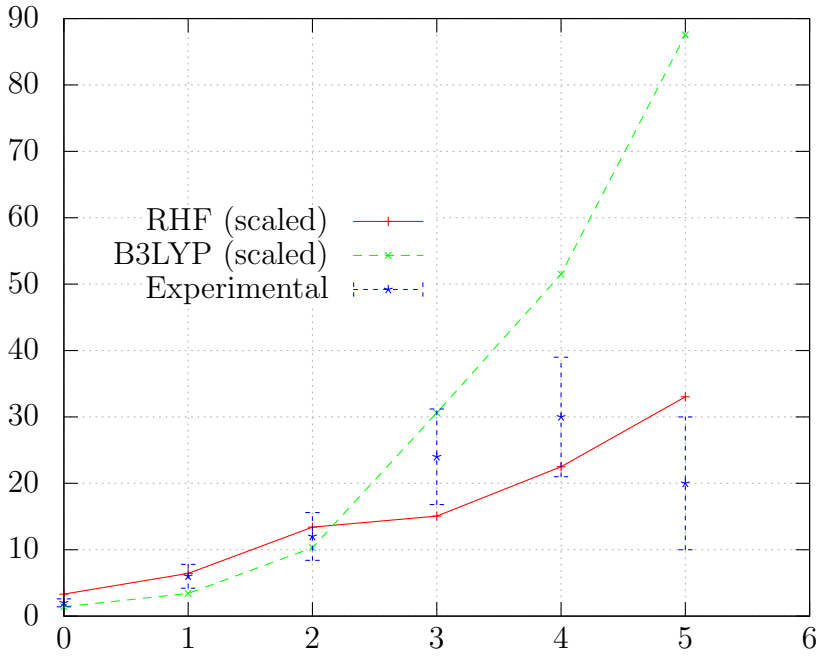

Figure 6.2: Comparison of the calculated third-order polarizabilities with two different levels of theory, and the estimated off-resonant values from the spectroscopy experimental measurements.

In Fig. 6.3 both the rotational average and diagonal tensor component along the axis of the triple bond acetylene spacer are plotted. The power-law increase for small molecules transitions to a linear increase with additional triple bonds in the spacer.

These calculated results do not agree with the experimental results. It is not clear why this calculation method (finite field) is not suited to calculating the third-order polarizabilities of these small molecules. Other methods, like Time-Dependent Hartree-Fock (TDHF) have given better results in the past [22] and it is probably a better choice for these types of calculations.

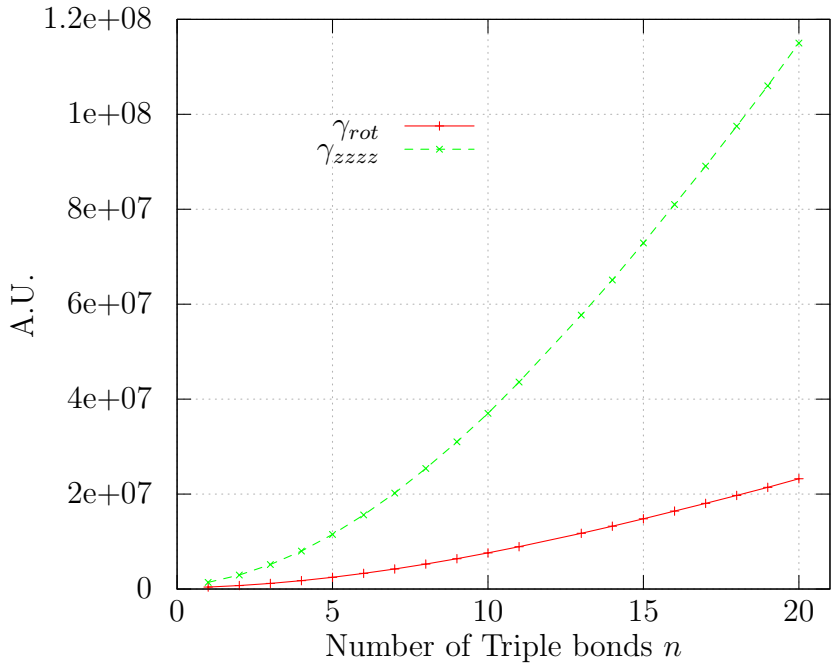

Figure 6.3: Finite field calculation results for a synthetic series of molecules with the acetylene triple bond spacer aligned to the z axis. One point at $n = 12$ is missing, but the trend is well established without it.

Chapter 7

Conclusion and Discussion

Small organic molecules with large off-resonant polarizabilities have been studied extensively because of their great potential for applications involving optical switching [24, 30, 44–53]. The ability to decrease the first excited optical transition by donor-acceptor substitution is a key tool for optimizing the optical response while keeping the size of the molecules small. This design approach is the crucial parameter that allows for the realization of small molecules with a large non-linear response.

In the solid state, for a given density, the $\chi^{(3)}$ of a material is related to the γ_{rot} of the constituent (weakly-interacting) molecules through the number density, so a better measure of a molecule's potential for applications is given by the specific parameter ($\tilde{\gamma} = \gamma_{\text{rot}}/M$, where M is the mass of the molecule in kg) which provides the relative figure of merit for the non-linear response per size of molecule. We have shown that it is possible to calculate the third-order susceptibility of the solid-state from the molecular third-order polarizability using a gas model, and it works [6].

Generally, smaller molecules lead to larger first-excite-state optical transitions, which in turn results in a decrease of the non-linear response. However, with donor-acceptor substitution, it is possible to lower the energy of the first optical transition, allowing small molecules to achieve large non-linearities.

It has been found that non-D/A substituted molecules scale super-linearly with repeated units (n), fit with a power law exponent near 4 or 5. A saturation effect has been identified for the very longest molecules, indicating that there is a maximum

obtainable $\tilde{\gamma}$ for a given molecular chain.

The polyyne molecules in Ref. [4] follow a very similar power law scaling behavior as can be derived from the Kuzyk limit which provides a theoretical upper bound for γ. The scaling of the D/A-substituted ISO-n and METH-n molecules is much less then the non-D/A polyyne molecules, but still consistent with the scaling expected from the fundamental limit because of the reduction on E_{10} by donor-acceptor substitution. This trend suggests that both types of conjugated systems provide a very efficient use of the delocalized π-electrons.

This work investigates the scaling behavior of D/A substituted molecules, and shows that there is a saturation effect caused by a physical mechanism different from non-D/A substituted molecules. The D/A substitution allows for obtaining large off-resonant polarizabilities in small molecules, but then places a corresponding limit on the maximum off-resonant values due to the isolation and physical separation of the HOMO and LUMO electronic states on the acceptor and donor groups respectively which causes saturation of the non-linear response as the molecule is scaled up.

Additional computational chemistry results help support this explanation of the physical mechanism which causes the saturation effect in D/A molecules. We determine that for this class of molecules, the optimal value occurs at $n = 3$ units.

In Fig. 7.1 the trends for the specific third-order polarizability ($\tilde{\gamma}$) of D/A and non-D/A substituted molecules are compared as additional triple bonds (n) are added to the molecule. This plot gives an indication of how $\tilde{\gamma}$ grows with the size of the conjugated π electrons. The significant result is that the D/A substituted molecules achieve large third-order polarizabilities with a very small conjugation size, and reach a maximum specific third-order polarizability better then even the longest non-D/A substituted molecules found in literature [4]. Attempts to scale non-D/A molecules to very large lengths has resulted in reaching a saturation point [3] indicating that they cannot be extended indefinitely.

Experimental spectroscopy identifies the wavelength regime where resonant enhancement is significant, and allows for the determination of off-resonant values. The relationship of the non-linear spectrum of γ_{rot} to the linear absorption spectrum provides a comparison useful for verifying the expected ranges of TPA.

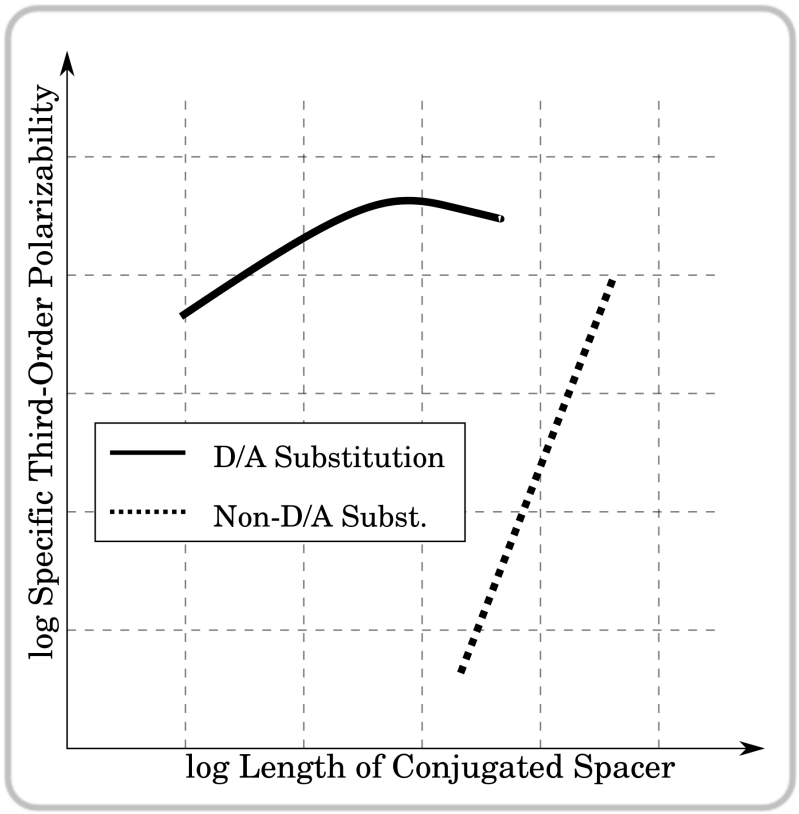

Figure 7.1: Schematic comparison of the specific third-order polarizability $\tilde{\gamma}$ versus number of triple bonds in the spacer n on a log-log plot. This is a metric that predicts the potential for molecules to assemble into solid-state supramolecular assemblies with a large value of $\chi^{(3)}$. The non-D/A substituted molecules scale with a power law of between 4 and 5, while the D/A substituted molecules scale with a power law of about half of that. Both types of molecular systems eventually reach some type of saturation, but the D/A substituted molecules reach a maximum $\tilde{\gamma}$ with much smaller molecules, thanks to donor-acceptor substitution.

Additionally, the spectroscopic data indicate that some degree of resonant enhancement could be utilized to further increase the third-order non-linear response at a wavelength where TPA is still small. The flexibility of the organic molecule platform allows for the fine-tuning of these energies and for obtaining a desired non-linear response at a specfic wavelength.

Appendix A

Expansion of Third-order Polarization

The expansion of equation 2.21 results in terms representing optical waves at 3ω and ω. There are 10 waves with a frequency of 3ω, they are:

$$\begin{aligned}
&\frac{1}{8}\Big(\mathcal{E}_1^3 e^{i[3\vec{k}_1\cdot\vec{x}-3\omega t]} + \mathcal{E}_2^3 e^{i[3\vec{k}_2\cdot\vec{x}-3\omega t]} + \mathcal{E}_3^3 e^{i[3\vec{k}_3\cdot\vec{x}-3\omega t]} \\
&+ 3\mathcal{E}_1^2\mathcal{E}_2 e^{i[(2\vec{k}_1+\vec{k}_2)\cdot\vec{x}-3\omega t]} + 3\mathcal{E}_1^2\mathcal{E}_3 e^{i[(2\vec{k}_1+\vec{k}_3)\cdot\vec{x}-3\omega t]} \\
&+ 3\mathcal{E}_1\mathcal{E}_2^2 e^{i[(\vec{k}_1+2\vec{k}_2)\cdot\vec{x}-3\omega t]} + 3\mathcal{E}_1\mathcal{E}_3^2 e^{i[(\vec{k}_1+2\vec{k}_3)\cdot\vec{x}-3\omega t]} + 3\mathcal{E}_2\mathcal{E}_2^2 e^{i[(\vec{k}_2+2\vec{k}_3)\cdot\vec{x}-3\omega t]} \\
&+ 3\mathcal{E}_2^2\mathcal{E}_3 e^{i[(2\vec{k}_2+\vec{k}_3)\cdot\vec{x}-3\omega t]} + 6\mathcal{E}_1\mathcal{E}_2\mathcal{E}_3 e^{i[(\vec{k}_1+\vec{k}_2+\vec{k}_3)\cdot\vec{x}-3\omega t]} + c.c.\Big)
\end{aligned} \tag{A.1}$$

There are 18 waves with a frequency of ω, they are:

$$
\begin{aligned}
&\frac{1}{8}\Big(3\mathcal{E}_1^2\mathcal{E}_1^* e^{i[(2\vec{k}_1-\vec{k}_1)\cdot\vec{x}-\omega t]} + 3\mathcal{E}_1^2\mathcal{E}_2^* e^{i[(2\vec{k}_1-\vec{k}_2)\cdot\vec{x}-\omega t]} \\
&+ 3\mathcal{E}_1^2\mathcal{E}_3^* e^{i[(2\vec{k}_1-\vec{k}_3)\cdot\vec{x}-\omega t]} + 3\mathcal{E}_2^2\mathcal{E}_1^* e^{i[(2\vec{k}_2-\vec{k}_1)\cdot\vec{x}-\omega t]} \\
&+ 3\mathcal{E}_2^2\mathcal{E}_2^* e^{i[(2\vec{k}_2-\vec{k}_2)\cdot\vec{x}-\omega t]} + 3\mathcal{E}_2^2\mathcal{E}_3^* e^{i[(2\vec{k}_2-\vec{k}_3)\cdot\vec{x}-\omega t]} \\
&+ 3\mathcal{E}_3^2\mathcal{E}_1^* e^{i[(2\vec{k}_3-\vec{k}_1)\cdot\vec{x}-\omega t]} + 3\mathcal{E}_3^2\mathcal{E}_2^* e^{i[(2\vec{k}_3-\vec{k}_2)\cdot\vec{x}-\omega t]} \\
&+ 3\mathcal{E}_3^2\mathcal{E}_3^* e^{i[(2\vec{k}_3-\vec{k}_3)\cdot\vec{x}-\omega t]} \\
&+ 6\mathcal{E}_1\mathcal{E}_1^*\mathcal{E}_2 e^{i[(\vec{k}_1-\vec{k}_1+\vec{k}_2)\cdot\vec{x}-\omega t]} + 6\mathcal{E}_1\mathcal{E}_1^*\mathcal{E}_3 e^{i[(\vec{k}_1-\vec{k}_1+\vec{k}_3)\cdot\vec{x}-\omega t]} \\
&+ 6\mathcal{E}_1\mathcal{E}_2^*\mathcal{E}_2 e^{i[(\vec{k}_1-\vec{k}_2+\vec{k}_2)\cdot\vec{x}-\omega t]} + 6\mathcal{E}_1\mathcal{E}_2^*\mathcal{E}_3 e^{i[(\vec{k}_1-\vec{k}_2+\vec{k}_3)\cdot\vec{x}-\omega t]} \\
&+ 6\mathcal{E}_1\mathcal{E}_3^*\mathcal{E}_2 e^{i[(\vec{k}_1-\vec{k}_3+\vec{k}_2)\cdot\vec{x}-\omega t]} + 6\mathcal{E}_1\mathcal{E}_3^*\mathcal{E}_3 e^{i[(\vec{k}_1-\vec{k}_3+\vec{k}_3)\cdot\vec{x}-\omega t]} \\
&+ 6\mathcal{E}_2\mathcal{E}_2^*\mathcal{E}_3 e^{i[(\vec{k}_2-\vec{k}_2+\vec{k}_3)\cdot\vec{x}-\omega t]} + 6\mathcal{E}_2\mathcal{E}_1^*\mathcal{E}_3 e^{i[(\vec{k}_2-\vec{k}_1+\vec{k}_3)\cdot\vec{x}-\omega t]} \\
&+ 6\mathcal{E}_2\mathcal{E}_3^*\mathcal{E}_3 e^{i[(\vec{k}_2-\vec{k}_3+\vec{k}_3)\cdot\vec{x}-\omega t]} + c.c.\Big)
\end{aligned}
\tag{A.2}
$$

Appendix B

Non-linear Polarization $P^{(3)}$: Quantum Description

A quantum treatment of the non-linear polarization is fundamentally more correct because it properly describes the discrete nature of the allowable electronic energy eigenstates of a molecule, as well as the discrete absorption or emission of a photon with a specific energy. Fundamentally, the origin of light and matter interaction involves electric fields exerting forces on charged particles. This is the mechanism by which energy is transferred between light and matter in which photons are absorbed or emitted, and matter is correspondingly excited or relaxed. We can write the Hamiltonian for an electromagnetic field and a charged particle using the electric dipole operator $\hat{\mu} = -e\vec{x}$ as

$$\hat{H} = \hat{H}_0 - \hat{\mu} \cdot \vec{E}(t) \tag{B.1}$$

where the electric field $E(t)$ may contain oscillating components at different frequencies, so it can be expressed as a sum

$$\vec{E}(t) = \sum_p \frac{1}{2} \mathcal{E}\left(\omega_p\right) e^{-i\omega_p t} \tag{B.2}$$

and $\mathcal{E}\left(\omega_p\right)$ is the complex amplitude of each frequency component ω_p. With the assumption that the wavelength of this optical wave is much longer then the size

of the atom, the electric field is uniform over the space of the atom, so there is no spatial dependence to the electric field.

We now bring in Schrödinger's equation and apply the method of perturbation solution because we cannot solve for externally applied electric fields in general. To this, we introduce a parameter λ in the Hamiltonian

$$\hat{H} = \hat{H}_0 - \lambda\hat{\mu}\cdot\vec{E}(t) \tag{B.3}$$

which varies from 0 to 1, allowing the potential to be introduced into the Hamiltonian as a small perturbation. The unperturbed Hamiltonian $\hat{H}_0$ is the usual Hamiltonian for a free atom. Since λ can be small, we can write the solution to Schrödinger's equation as a power series in λ

$$\psi(\vec{x},t) = \psi^{(0)}(\vec{x},t)+\lambda\psi^{(1)}(\vec{x},t)+\lambda^2\psi^{(2)}(\vec{x},t)+\lambda^3\psi^{(3)}(\vec{x},t)+\cdots+\lambda^N\psi^{(N)}(\vec{x},t) \tag{B.4}$$

where $\psi^{(0)}(\vec{x},t)$ is the solution to the unperturbed hamiltonian ($\hat{H}_0$). By substituting this solution into Schrödinger's equation, and re-arranging to group like powers of λ together, we get

$$\begin{aligned}
&i\hbar\frac{\partial}{\partial t}\psi^{(0)}(\vec{x},t) - \hat{H}_0(\vec{x},t) \\
&+\lambda\left[i\hbar\frac{\partial}{\partial t}\psi^{(1)}(\vec{x},t) - \hat{H}_0(\vec{x},t)\psi^{(1)} + \hat{\mu}\cdot\vec{E}(t)\psi^{(0)}(\vec{x},t)\right] \\
&+\lambda^2\left[i\hbar\frac{\partial}{\partial t}\psi^{(2)}(\vec{x},t) - \hat{H}_0(\vec{x},t)\psi^{(2)} + \hat{\mu}\cdot\vec{E}(t)\psi^{(1)}(\vec{x},t)\right] \\
&+\lambda^3\left[i\hbar\frac{\partial}{\partial t}\psi^{(3)}(\vec{x},t) - \hat{H}_0(\vec{x},t)\psi^{(3)} + \hat{\mu}\cdot\vec{E}(t)\psi^{(2)}(\vec{x},t)\right] + \cdots + \\
&+\lambda^N\left[i\hbar\frac{\partial}{\partial t}\psi^{(N)}(\vec{x},t) - \hat{H}_0(\vec{x},t)\psi^{(N)} + \hat{\mu}\cdot\vec{E}(t)\psi^{(N-1)}(\vec{x},t)\right] = 0.
\end{aligned} \tag{B.5}$$

This can be separated into $N+1$ equations because each term proportional to λ must equal zero independently to satisfy Schrödinger's equation. The solutions to the unperturbed Hamiltonian ($\psi^{(0)}$) are called the stationary states of electrons in a free atom. We can express the set of those solutions as a combination of a

space-dependent part, and a time-dependent part as

$$\psi_k^{(0)}(\vec{x},t) = u_k(\vec{x})e^{-i\omega_k t} \tag{B.6}$$

allowing us to turn the time-dependent Schrödinger's equation into a time-independent one

$$E_k u_k(\vec{x}) = \hat{H}_0 u_k(\vec{x}) \tag{B.7}$$

where $E_k = \hbar\omega_k$ is the energy of the eigenstate $u_k(\vec{x})$. These stationary states form a complete and orthogonal basis set for the electronic states of the free atom defined by $\hat{H}_0$. Because we consider the non-linear portion of the solution to be small, and treat it as a perturbation, we can use linear combinations of the unperturbed basis set to construct solutions to the perturbed hamiltonian. So we can write a solution as

$$\psi^{(N)}(\vec{x},t) = \sum_k a_k^{(N)}(t)\psi_k^{(0)}(\vec{x},t) \tag{B.8}$$

where $a_k^{(N)}(t)$ are the time-dependent coefficients of the k^{th} wavefunctions which construct a solution to the N^{th}-order wavefunction $\psi^{(N)}(\vec{x},t)$.

Each term proportional to λ^N must independently be equal to zero, so B.5 becomes

$$i\hbar\frac{\partial}{\partial t}\left(\sum_k a_k^{(N)}\psi_k^{(0)}\right) = \hat{H}_0\left(\sum_k a_k^{(N)}\psi_k^{(0)}\right) - \hat{\mu}\cdot\vec{E}(t)\left(\sum_k a_k^{(N-1)}\psi_k^{(0)}\right) = 0 \tag{B.9}$$

which we want to solve for the respective coefficients $a_k^{(N)}$. The next step therefore is to substitute the stationary states $\psi_k^{(0)}(\vec{x},t) = u_k(\vec{x})e^{-i\omega t}$, resulting in

$$i\hbar\frac{\partial}{\partial t}\sum_k a_k^{(N)}u_k(\vec{x})e^{-i\omega_k t} = \hat{H}_0\sum_k a^{(N)}u_k(\vec{x})e^{-i\omega_k t} - \hat{\mu}\cdot\vec{E}(t)\sum_k a_k^{(N-1)}u_k(\vec{x})e^{-i\omega_k t} \tag{B.10}$$

and after taking the derivates and evaluating the unperturbed hamiltonian ($\hat{H}_0$)

$$\begin{aligned} &i\hbar \sum_k \dot{a}_k^{(N)} u_k(\vec{x}) e^{-i\omega_k t} + i\hbar \sum_k a_k^{(N)} u_k(\vec{x})(-i\omega_k) e^{-i\omega_k t} \\ &= \sum_k a^{(N)} \hbar \omega_k u_k(\vec{x}) e^{-i\omega_k t} - \hat{\mu} \cdot \vec{E}(t) \sum_k a_k^{(N-1)} u_k(\vec{x}) e^{-i\omega_k t} \end{aligned} \tag{B.11}$$

which simplifies to

$$i\hbar \sum_k \dot{a}_k^{(N)} u_k(\vec{x}) e^{-i\omega_k t} = -\hat{\mu} \cdot \vec{E}(t) \sum_k a_k^{(N-1)} u_k(\vec{x}) e^{-i\omega_k t}. \tag{B.12}$$

Now this equation can be used to determine the coefficients of the N^{th} non-linear states by multiplying each side by $u_l^*(\vec{x}) e^{i\omega_l t}$, and then integrating over space to project out the desired coefficients $\dot{a}_k^{(N)}(t)$.

$$i\hbar \sum_k \dot{a}_k^{(N)}(t) \delta_{l,k} e^{i(\omega_l - \omega_k)t} = \sum_k a_k^{(N-1)}(t) \left(\int u_l^*(\vec{x})(-\hat{\mu} \cdot \vec{E}(t)) u_k(\vec{x}) d\vec{x} \right) e^{i(\omega_l - \omega_k)t} \tag{B.13}$$

which can be directly solved for $\dot{a}_l^{(N)}(t)$ because $\delta_{l,k} = 1$ only when $l = k$. The rest of the terms in the right side of the sum will be zero. Therefore

$$\dot{a}_l^{(N)}(t) = \frac{1}{i\hbar} \sum_k a_k^{(N-1)}(t) \left(\int u_l^*(\vec{x})(-\hat{\mu} \cdot \vec{E}(t)) u_k(\vec{x}) d\vec{x} \right) e^{i(\omega_l - \omega_k)t} \tag{B.14}$$

and then $a_l^{(N)}(t)$ can be obtained by integrating over time from $-\infty$ to t.

$$a_l^{(N)}(t) = \frac{1}{i\hbar} \sum_k \int_{-\infty}^{t} \left[a_k^{(N-1)}(t') \left(\int u_l^*(\vec{x})(-\hat{\mu} \cdot \vec{E}(t')) u_k(\vec{x}) d\vec{x} \right) e^{i(\omega_l - \omega_k)t'} \right] dt' \tag{B.15}$$

This allows for the computation of any of the N^{th} order coefficients from the known lower order coefficients, starting with the coefficients a_k^0 zeroth-order $\psi^{(0)}$ wavefunction.

The dipole transition integrals between two states ψ_1 and ψ_2 can be more neatly

written in Dirac notation as

$$\langle \hat{p} \rangle = \langle \psi_1 \mid \hat{\mu} \mid \psi_2 \rangle. \tag{B.16}$$

Skipping some of the intermediate steps for $N = 1$ and $N = 2$, the result for $N = 3$ is

$$a_n^{(3)}(t) = \frac{1}{8\hbar^3} \sum_{p,q,r} \sum_{l,m} \frac{\langle u_n|\hat{\mu}|u_m\rangle\langle u_m|\hat{\mu}|u_l\rangle\langle u_l|\hat{\mu}|u_g\rangle E(\omega_p)E(\omega_q)E(\omega_r)e^{i(\Delta\omega_{ng}-\omega_p-\omega_q-\omega_r)t}}{(\Delta\omega_{ng}-\omega_p-\omega_q-\omega_r)\,(\Delta\omega_{mg}-\omega_p-\omega_q)\,(\Delta\omega_{lg}-\omega_p)} \tag{B.17}$$

where $\Delta\omega_{ng} = \omega_n - \omega_g$. The summation is over all states, but only some of them are non-zero.

The third-order dipole moment involves transitions between the states $\psi^{(0)}$, $\psi^{(1)}$, $\psi^{(2)}$, and $\psi^{(3)}$ as defined in equation B.8. The expectation value for the third-order polarizability is therefore expressed as

$$\langle \hat{p}^{(3)} \rangle = \langle \psi^{(0)} \mid \hat{\mu} \mid \psi^{(3)} \rangle + \langle \psi^{(1)} \mid \hat{\mu} \mid \psi^{(2)} \rangle + \langle \psi^{(2)} \mid \hat{\mu} \mid \psi^{(1)} \rangle + \langle \psi^{(3)} \mid \hat{\mu} \mid \psi^{(0)} \rangle \tag{B.18}$$

where (as determined above), the states are defined in terms of the unperturbed eigenstates with the coefficients as calculated in equation B.17.

$$\psi^{(0)} = \psi_g^{(0)} = u_g e^{-i\omega_g t} \tag{B.19}$$

$$\psi^{(1)} = \sum_l a_l^{(1)} \psi_l^{(0)} = \sum_l a_l^{(1)} u_l(\vec{x}) e^{-i\omega_l t} \tag{B.20}$$

$$\psi^{(2)} = \sum_m a_m^{(2)} \psi_m^{(0)} = \sum_m a_m^{(2)} u_m(\vec{x}) e^{-i\omega_m t} \tag{B.21}$$

$$\psi^{(3)} = \sum_n a_n^{(3)} \psi_n^{(0)} = \sum_n a_n^{(3)} u_n(\vec{x}) e^{-i\omega_n t} \tag{B.22}$$

Inserting the calculated values for $a_n^{(3)}(t)$ in equation B.17 into equation B.18 with wave functions in equation B.22 gives an expression for the third-order polarization in terms of known quantities which are the spatial wave functions of the unperturbed hamiltonian ($u_l(\vec{x})$), energy differences of those states ($\Delta\omega_{mg}$), energies of

the incident optical waves (ω_k), and amplitudes of those incident fields.

$$\langle \hat{p}^{(3)} \rangle = \frac{1}{\hbar^3} \sum_{p,q,r} \sum_{l,m,n} \left[\left(\frac{\langle u_g \mid \hat{\mu} \mid u_n \rangle \langle u_n \mid \hat{\mu} \mid u_m \rangle \langle u_m \mid \hat{\mu} \mid u_l \rangle \langle u_l \mid \hat{\mu} \mid u_g \rangle}{(\Delta\omega_{ng} - \omega_p - \omega_q - \omega_r)(\Delta\omega_{mg} - \omega_p - \omega_q)(\Delta\omega_{lg} - \omega_p)} \right. \right.$$
$$+ \frac{\langle u_g \mid \hat{\mu} \mid u_n \rangle \langle u_n \mid \hat{\mu} \mid u_m \rangle \langle u_m \mid \hat{\mu} \mid u_l \rangle \langle u_l \mid \hat{\mu} \mid u_g \rangle}{\left(\Delta\omega_{ng}^* + \omega_p\right)(\Delta\omega_{mg} - \omega_q - \omega_r)(\Delta\omega_{lg} - \omega_r)}$$
$$+ \frac{\langle u_g \mid \hat{\mu} \mid u_n \rangle \langle u_n \mid \hat{\mu} \mid u_m \rangle \langle u_m \mid \hat{\mu} \mid u_l \rangle \langle u_l \mid \hat{\mu} \mid u_g \rangle}{\left(\Delta\omega_{ng}^* + \omega_r\right)(\Delta\omega_{mg} + \omega_q + \omega_r)(\Delta\omega_{lg} - \omega_p)}$$
$$\left. + \frac{\langle u_g \mid \hat{\mu} \mid u_n \rangle \langle u_n \mid \hat{\mu} \mid u_m \rangle \langle u_m \mid \hat{\mu} \mid u_l \rangle \langle u_l \mid \hat{\mu} \mid u_g \rangle}{\left(\Delta\omega_{ng}^* + \omega_p\right)\left(\Delta\omega_{mg}^* + \omega_p + \omega_q\right)\left(\Delta\omega_{lg}^* + \omega_p + \omega_q + \omega_r\right)} \right) \times$$
$$\left. \frac{E(\omega_p)}{2} \frac{E(\omega_q)}{2} \frac{E(\omega_r)}{2} e^{-i(\omega_p + \omega_q + \omega_r)t} \right] \tag{B.23}$$

Appendix C

Extinction Coefficients

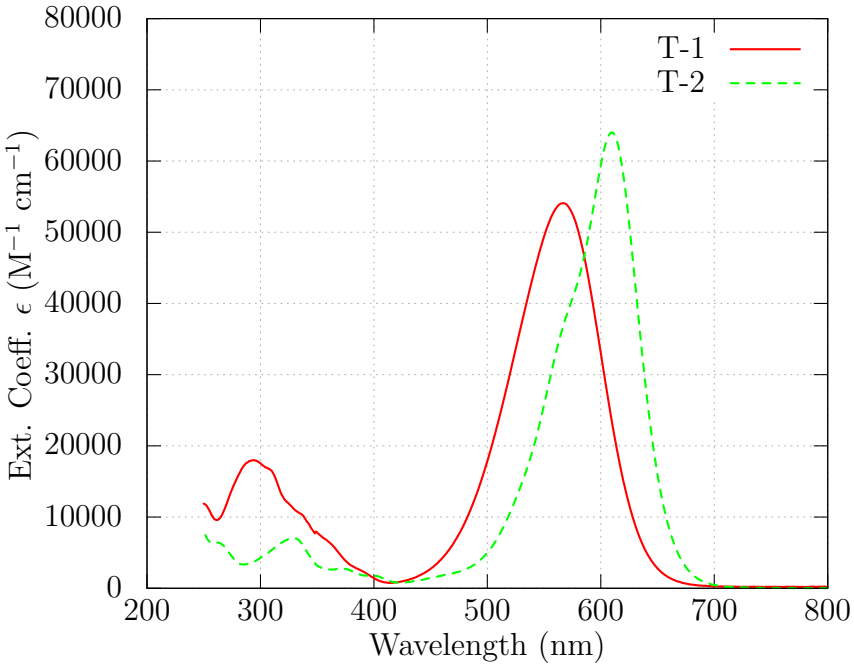

Figure C.1: The extinction coefficients for the T-x molecules.

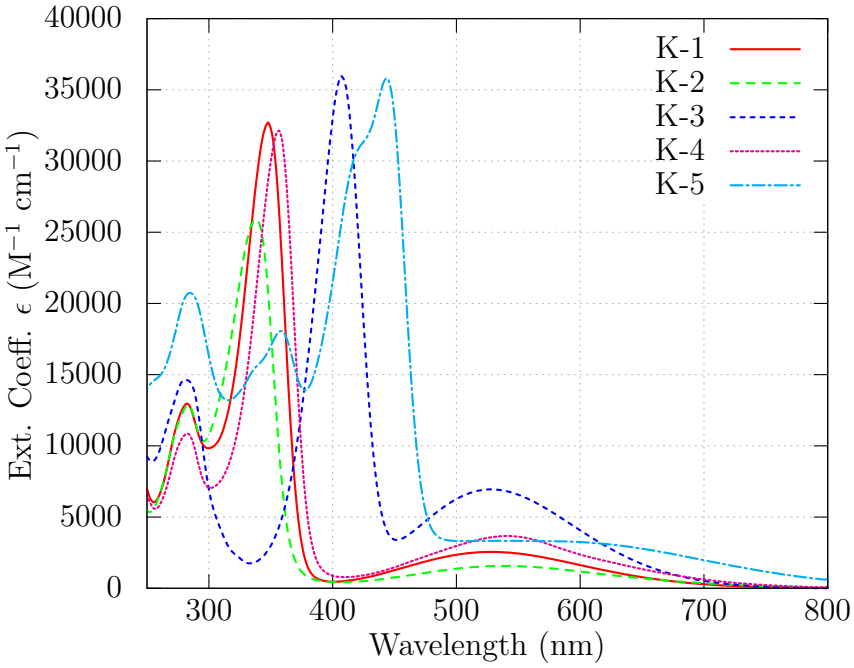

Figure C.2: The extinction coefficients for the K-x molecules.

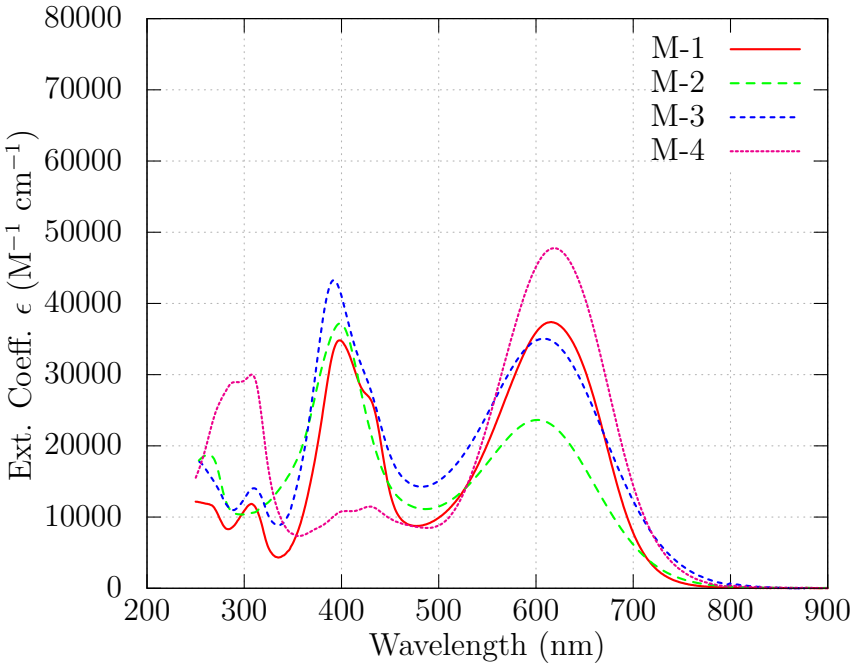

Figure C.3: The extinction coefficients for the C-x molecules.

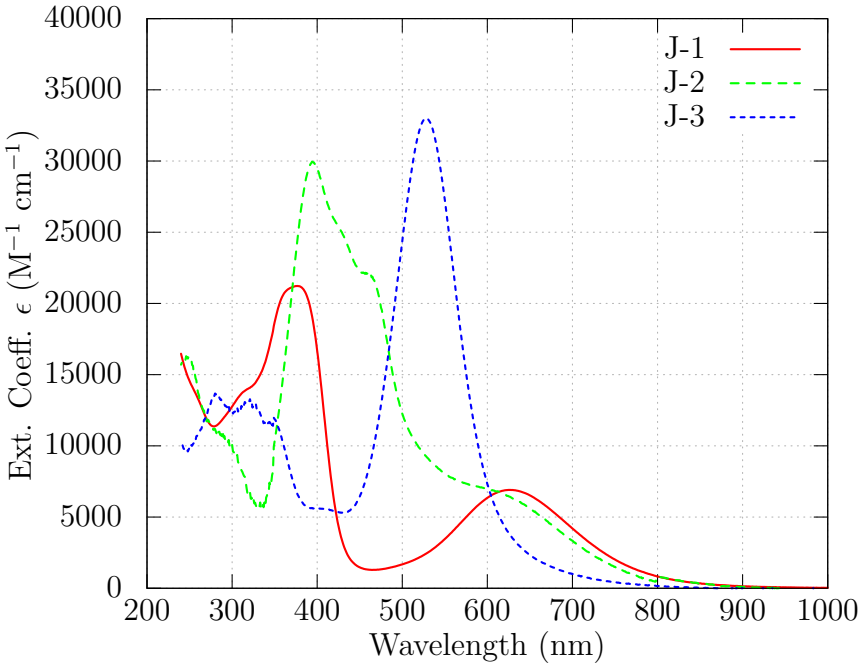

Figure C.4: The extinction coefficients for the J-x molecules.

Appendix D

GAMESS Input Files

An example input header for a geometry optimization is:

```
!   File created by the GAMESS Input Deck Generator Plugin for Avogadro
 $BASIS GBASIS=N31 NGAUSS=6 NDFUNC=1 NPFUNC=1 $END
 $CONTRL SCFTYP=RHF RUNTYP=OPTIMIZE DFTTYP=B3LYP
MOLPLT=.TRUE. maxit=50 $END
 $SYSTEM MWORDS=50 $END
 $STATPT OPTTOL=0.0001 NSTEP=90 $END
 $SCF DIRSCF=.TRUE. $END
 $DATA
DDMEBT-0 Geometry Optimization using starting coordinates
from Marvin Sketch
C1
C     6.0    -1.02017     2.77229    -2.91129
C     6.0    -1.25148     4.00425    -3.53129
C     6.0    -2.32066     4.18193    -4.41839
```

Sample input file for a Finite Field calculation using RHF level of theory

```
 $CONTRL
SCFTYP=RHF
RUNTYP=ffield
MOLPLT=.TRUE.
icut=20
itol=30
maxit=50
```

```
qmttol=1e-6
 $END
 $BASIS
GBASIS=N31
NGAUSS=6
NDFUNC=1
NPFUNC=1
DIFFSP=.TRUE.
DIFFS=.TRUE.
 $END
 $SYSTEM
MWORDS=10
 $END
 $SCF
DIRSCF=.TRUE.
CONV=1d-7
FDIFF=.FALSE.
 $END
 $FFCALC
offdia=.t.
 $END

 $DATA
Finite Field calculation using coordinates from geometry
optimization run.
C1
 C           6.0  -2.9795353282   2.9583579567  -3.0505828786
 C           6.0  -2.9435366255   4.1876120382  -3.6790033797
 C           6.0  -2.0784616593   4.4379760679  -4.7800923537
```

Sample excerpt taken from the output file of a Finite Field calculation

```
                  ----ENERGY BASED RESULTS----
  DIPOLE #         X                   Y                   Z   (A.U.)
 ######################################################################
        #  -4.0205306E+00      2.4305621E+00     -1.5619378E+00

  ALPHA #         X                   Y                   Z   (A.U.)
 ######################################################################
```

```
 X    #   4.6102449E+02      6.9836597E+01     -3.1415531E+01
 Y    #   6.9836597E+01      4.8389535E+02     -5.6060503E+01
 Z    #  -3.1415531E+01     -5.6060503E+01      3.9750307E+02

 BETA  #        X                   Y                   Z   (A.U.)
########################################################################
 XX    #  -4.5449899E+03     -2.0572675E+03      5.8622186E+02
 YY    #  -3.0764522E+02      3.8341891E+03     -2.1696123E+03
 ZZ    #   3.1322838E+02      9.6190706E+02     -1.7505067E+02

 GAMMA #        XX                  YY                  ZZ   (A.U.)
########################################################################
 XX    #   4.5173510E+05      7.3661795E+04      3.7671271E+03
 YY    #   7.3661795E+04      4.0252871E+05      9.8261808E+04
 ZZ    #   3.7671271E+03      9.8261808E+04      6.9117050E+04

                  ----DIPOLE BASED RESULTS----
 DIPOLE #        X                   Y                   Z   (A.U.)
########################################################################
       #  -4.0205263E+00      2.4305592E+00     -1.5619378E+00

 ALPHA #        X                   Y                   Z   (A.U.)
########################################################################
 X    #   4.6102448E+02      6.9836784E+01     -3.1415702E+01
 Y    #   6.9836783E+01      4.8389546E+02     -5.6060659E+01
 Z    #  -3.1415440E+01     -5.6060619E+01      3.9750297E+02

 BETA  #        X                   Y                   Z   (A.U.)
########################################################################
 XX    #  -4.5503062E+03     -2.0609816E+03      5.8792890E+02
 YY    #  -3.0646642E+02      3.8379276E+03     -2.1735348E+03
 ZZ    #   3.1302375E+02      9.6128377E+02     -1.7512002E+02

 GAMMA #        XX                  YY                  ZZ   (A.U.)
########################################################################
 XX    #   4.5171828E+05      7.3645512E+04      3.9026965E+03
 YY    #   7.3645512E+04      4.0237920E+05      9.8566298E+04
 ZZ    #   3.9026965E+03      9.8566298E+04      6.9374701E+04
```

Appendix E

Fitting Scripts

An example fitting script for unconstrained real and imaginary parts of γ, for the Iso-4 molecule which incorporates linear absorption.

```
Closest = 0.02
Fixed = 0.30
Farest = 0.75

file = "Combined.txt"

set fit errorvariables
FIT_LIMIT = 1.e-8

average(one, two) = (one + two)/2.0
Bezy(x,Ay,By,Cy) = average(Ay,By)*(1-x)**2 + 2*(1-x)*x*By +
average(By,Cy)*x**2

#initial parameters
RealKnot1 = 3.43
RealKnot2 = 2.13
RealKnot3 = -12.8
RealKnot4 = -1.6
RealKnot5 = 17.8
RealKnot6 = 41.3
RealKnot7 = 76.6
RealKnot8 = 38.5
RealKnot9 = 34.4
```

```
RealKnot10 = 29.7
RealKnot11 = 34.7
RealKnot12 = 31.1

RealKnot12_err = 1.0

ImagKnot1 = 448.5
ImagKnot2 = 113.2
ImagKnot3 = 103.7
ImagKnot4 = 34.9
ImagKnot5 = 32.9
ImagKnot6 = 17.2
ImagKnot7 = 13.2
ImagKnot8 = 0.91
ImagKnot9 = -0.11
ImagKnot10 = 0.14
ImagKnot11 = -2.6
ImagKnot12 = 0.2

ImagKnot12_err = 1.0

Absorption = 5.07e+06

#array of the relative intensities
Intensities = " 1.809210525E-005 0.0004671053 0.0042516447
0.0079029605 0.0119358553 0.0149884868 0.0202598684
0.0228388158 0.0261792763 0.0267927632 0.0247845395
0.0248273026 0.0307483553 0.0299724107 0.0362763158
0.0410921053 0.0434671053 0.0442648026 0.0472582237
0.0465263158 0.04459375 0.0504391447 0.0542203947
0.0542697368 0.0546628289 0.0586430921 0.0572391739
0.0597138158 0.0605970395 0.0649424342 0.0649819079
0.0671842105 0.0575838816 0.0588817674 0.0616858553
0.0687976974 0.0745411184 0.0563026316 0.0829884868
0.0828338816 0.0746348684 0.0779917763 0.0809490132
0.0791217105 0.0774358553 0.0802697368 0.0755148026
0.0783503289 0.0787730263 0.0790411184 0.07821875
0.079948962 0.0819309211 0.0796708718 0.0794671053
0.0809884868 0.0834731818 0.0847911184 0.094875
0.0918486842 0.0223519737 0.0547845395 0.0695276963
```

```
0.0264358553 "

intensity(n) = word(Intensities,n)

#This is the fitted absorbance at the highest concentration
#as a function of wavelength
A(y) = exp(-(y-956.146)/155.41)+0.0854-0.036

#function returns alpha for a given wavelength, and concentration
alpha(x,y) = 2.303 * A(y) * x / (0.001*1.25)

#Given an index between 0 and 63, this returns the
corresponding wavelength
WL(y) = int(y)%64*10+1050

gamma_R(x) =
     (x < 1105) ? Bezy(((x-1035)/70.0),RealKnot1,RealKnot2,RealKnot3) :
     (x<1175) ? Bezy(((x-1105)/70.0),RealKnot2,RealKnot3,RealKnot4) :
     (x<1245) ? Bezy(((x-1175)/70.0),RealKnot3,RealKnot4,RealKnot5) :
     (x<1315) ? Bezy(((x-1245)/70.0),RealKnot4,RealKnot5,RealKnot6) :
     (x<1385) ? Bezy(((x-1315)/70.0),RealKnot5,RealKnot6,RealKnot7) :
     (x<1455) ? Bezy(((x-1385)/70.0),RealKnot6,RealKnot7,RealKnot8) :
     (x<1525) ? Bezy(((x-1455)/70.0),RealKnot7,RealKnot8,RealKnot9) :
     (x<1595) ? Bezy(((x-1525)/70.0),RealKnot8,RealKnot9,RealKnot10) :
     (x<1665) ? Bezy(((x-1595)/70.0),RealKnot9,RealKnot10,RealKnot11) :
     (x<1735) ? Bezy(((x-1665)/70.0),RealKnot10,RealKnot11,RealKnot12)
: 0

gamma_I(x) =
     (x < 1105) ? Bezy(((x-1035)/70.0),ImagKnot1,ImagKnot2,ImagKnot3) :
     (x<1175) ? Bezy(((x-1105)/70.0),ImagKnot2,ImagKnot3,ImagKnot4) :
     (x<1245) ? Bezy(((x-1175)/70.0),ImagKnot3,ImagKnot4,ImagKnot5) :
     (x<1315) ? Bezy(((x-1245)/70.0),ImagKnot4,ImagKnot5,ImagKnot6) :
     (x<1385) ? Bezy(((x-1315)/70.0),ImagKnot5,ImagKnot6,ImagKnot7) :
     (x<1455) ? Bezy(((x-1385)/70.0),ImagKnot6,ImagKnot7,ImagKnot8) :
     (x<1525) ? Bezy(((x-1455)/70.0),ImagKnot7,ImagKnot8,ImagKnot9) :
     (x<1595) ? Bezy(((x-1525)/70.0),ImagKnot8,ImagKnot9,ImagKnot10) :
     (x<1665) ? Bezy(((x-1595)/70.0),ImagKnot9,ImagKnot10,ImagKnot11) :
     (x<1735) ? Bezy(((x-1665)/70.0),ImagKnot10,ImagKnot11,ImagKnot12)
: 0
```

```
ns=1.42
f=(ns**2 + 2)/3
rho=1.3266
Na=6.022
M=600.75
chi3s=12
terms=10*f**4*rho*Na/M

Tclosest(x,y) = (x>0.01) ? alpha(x,WL(y))/(x*gamma_I(WL(y))*Closest*
     intensity(int(y)%64+1)*Absorption*(exp(alpha(x,WL(y))*0.001)-1.)
     /(WL(y)) + alpha(x,WL(y))*exp(alpha(x,WL(y))*0.001)) : 1.

Tfixed(x,y) = (x>0.01) ? alpha(x,WL(y))/(x*gamma_I(WL(y))*Fixed*
     intensity(int(y)%64+1)*Absorption*(exp(alpha(x,WL(y))*0.001)-1.)
     /(WL(y)) + alpha(x,WL(y))*exp(alpha(x,WL(y))*0.001)) : 1.

Tfarest(x,y) = (x>0.01) ? alpha(x,WL(y))/(x*gamma_I(WL(y))*Farest*
     intensity(int(y)%64+1)*Absorption*(exp(alpha(x,WL(y))*0.001)-1.)
     /(WL(y)) + alpha(x,WL(y))*exp(alpha(x,WL(y))*0.001)) : 1.

Tsignal(x,y) = exp(-alpha(x,WL(y))*0.001)

chi(x,y) = (y<512) ? sqrt((chi3s+terms*gamma_R(WL(y))*x)**2+
     (terms*gamma_I(WL(y))*x)**2)/chi3s*sqrt(Tclosest(x,y)*Tfixed(x,y)*
     Tfarest(x,y)*Tsignal(x,y)) : Tfarest(x,y)


fit chi(x,y) file using 1:0:2:(1) via RealKnot1, RealKnot2, RealKnot3,
     RealKnot4, RealKnot5, RealKnot6, RealKnot7, RealKnot8, RealKnot9,
     RealKnot10, RealKnot11, ImagKnot1, ImagKnot2, ImagKnot3, ImagKnot4,
     ImagKnot5, ImagKnot6, ImagKnot7, ImagKnot8, ImagKnot9, ImagKnot10,
     ImagKnot11, Absorption

set print "gamma_scan.txt"
do for [ i = 0:63] {
     print i*10+1050,gamma_R(i*10+1050),gamma_R(i*10+1050)*0.3,
     gamma_I(i*10+1050),gamma_I(i*10+1050)*0.3+10,Absorption
     *intensity(i+1)
}
```

```
unset print

set print "parameters.txt"
     print 1000, RealKnot1, RealKnot1_err, ImagKnot1, ImagKnot1_err
     print 1070, RealKnot2, RealKnot2_err, ImagKnot2, ImagKnot2_err
     print 1140, RealKnot3, RealKnot3_err, ImagKnot3, ImagKnot3_err
     print 1210, RealKnot4, RealKnot4_err, ImagKnot4, ImagKnot4_err
     print 1280, RealKnot5, RealKnot5_err, ImagKnot5, ImagKnot5_err
     print 1350, RealKnot6, RealKnot6_err, ImagKnot6, ImagKnot6_err
     print 1420, RealKnot7, RealKnot7_err, ImagKnot7, ImagKnot7_err
     print 1490, RealKnot8, RealKnot8_err, ImagKnot8, ImagKnot8_err
     print 1560, RealKnot9, RealKnot9_err, ImagKnot9, ImagKnot9_err
     print 1630, RealKnot10, RealKnot10_err, ImagKnot10, ImagKnot10_err
     print 1700, RealKnot11, RealKnot11_err, ImagKnot11, ImagKnot11_err
     print 1770, RealKnot12, RealKnot12_err, ImagKnot12, ImagKnot12_err
unset print

set grid

set title "ISO-4"
set xlabel "Wavelength (nm)"
plot [1080:1680][-50:140] gamma_R(x) lw 3 title "Real",
     gamma_I(x) lw 3 title "Imaginary",
     'parameters.txt' using 1:2:3 with yerror title "Real Knots",
     '' using 1:4:5 with yerror title "Imaginary Knots"
```

An example fitting script for the imaginary part constrained to be the scaled linear absorbance spectrum, at twice the wavelength.

```
Closest = 0.02
Fixed = 0.30
Farest = 0.75

file = "Combined-err.csv"

set fit errorvariables
FIT_LIMIT = 1.e-8

average(one, two) = (one + two)/2.0
```

```
Bezy(x,Ay,By,Cy) = average(Ay,By)*(1-x)**2 + 2*(1-x)*x*By +
     average(By,Cy)*x**2

RealKnot1 = 3.43
RealKnot2 = 2.13
RealKnot3 = -12.8
RealKnot4 = -1.6
RealKnot5 = 17.8
RealKnot6 = 41.3
RealKnot7 = 76.6
RealKnot8 = 38.5
RealKnot9 = 34.4
RealKnot10 = 29.7
RealKnot11 = 34.7
RealKnot12 = 31.1

RealKnot12_err = 1.0

ImagScale = 0.0012

Absorption = 4.8e06


Intensities = " 1.809210525E-005 0.0004671053 0.0042516447 0.0079029605
0.0119358553 0.0149884868 0.0202598684
0.0228388158 0.0261792763 0.0267927632 0.0247845395
0.0248273026 0.0307483553 0.0299724107 0.0362763158
0.0410921053 0.0434671053 0.0442648026 0.0472582237
0.0465263158 0.04459375 0.0504391447 0.0542203947
0.0542697368 0.0546628289 0.0586430921 0.0572391739
0.0597138158 0.0605970395 0.0649424342 0.0649819079
0.0671842105 0.0575838816 0.0588817674 0.0616858553
0.0687976974 0.0745411184 0.0563026316 0.0829884868
0.0828338816 0.0746348684 0.0779917763 0.0809490132
0.0791217105 0.0774358553 0.0802697368 0.0755148026
0.0783503289 0.0787730263 0.0790411184 0.07821875
0.079948962 0.0819309211 0.0796708718 0.0794671053
0.0809884868 0.0834731818 0.0847911184 0.094875
0.0918486842 0.0223519737 0.0547845395 0.0695276963
0.0264358553 "
```

```
intensity(n) = word(Intensities,n)

LinearData = "13509.02859 12984.87093 12976.98077 13228.71168
13661.59879 14235.49559 14909.00573 15600.07594 16339.77331
17034.99258 17787.38387 18480.74421 19178.88969 19840.28704
20449.48936 21009.58489 21483.65043 21910.12539 22236.48503
22438.69193 22581.51397 22583.70444 22450.19935 22206.19284
21848.27812 21366.41927 20779.71958 20087.29987 19321.79928
18474.62356 17576.73733 16616.56238 15642.24996 14658.78915
13667.8759 12683.44466 11719.03406 10791.85028 9880.587456
9048.211388 8234.835231 7472.686006 6774.891169 6114.727352
5487.589631 4931.871314 4413.813818 3934.185021 3522.715531
3122.933442 2774.744294 2446.549712 2192.798536 1925.96484
1679.16331 1557.746902 1344.836201 1199.433348 1050.052466
912.6404181 791.0843125 686.2136069 590.053678 509.2141219"

Linear(n) = word(LinearData,n)

#This is the fitted absorbance at the highest concentration
# as a function of wavelength
A(y) = exp(-(y-956.146)/155.41)+0.0854-0.036

alpha(x,y) = 2.303 * A(y) * x / (0.001*1.25)

#Given an index between 0 and 63, this returns the
corresponding wavelength
WL(y) = int(y)%64*10+1050

gamma_R(x) =
     (x < 1105) ? Bezy(((x-1035)/70.0),RealKnot1,RealKnot2,RealKnot3) :
     (x<1175) ? Bezy(((x-1105)/70.0),RealKnot2,RealKnot3,RealKnot4) :
     (x<1245) ? Bezy(((x-1175)/70.0),RealKnot3,RealKnot4,RealKnot5) :
     (x<1315) ? Bezy(((x-1245)/70.0),RealKnot4,RealKnot5,RealKnot6) :
     (x<1385) ? Bezy(((x-1315)/70.0),RealKnot5,RealKnot6,RealKnot7) :
     (x<1455) ? Bezy(((x-1385)/70.0),RealKnot6,RealKnot7,RealKnot8) :
     (x<1525) ? Bezy(((x-1455)/70.0),RealKnot7,RealKnot8,RealKnot9) :
     (x<1595) ? Bezy(((x-1525)/70.0),RealKnot8,RealKnot9,RealKnot10) :
     (x<1665) ? Bezy(((x-1595)/70.0),RealKnot9,RealKnot10,RealKnot11) :
     (x<1735) ? Bezy(((x-1665)/70.0),RealKnot10,RealKnot11,RealKnot12)
```

```
: 0

gamma_I(x) = ImagScale * Linear(int((x-1040)/10))

ns=1.42
f=(ns**2 + 2)/3
rho=1.3266
Na=6.022
M=600.75
chi3s=12
terms=10*f**4*rho*Na/M

Tclosest(x,y) = (x>0.01) ? alpha(x,WL(y))/(x*gamma_I(WL(y))*Closest*
     intensity(int(y)%64+1)*Absorption*(exp(alpha(x,WL(y))*0.001)-1.)
     /(WL(y)) + alpha(x,WL(y))*exp(alpha(x,WL(y))*0.001)) : 1.

Tfixed(x,y) = (x>0.01) ? alpha(x,WL(y))/(x*gamma_I(WL(y))*Fixed*
     intensity(int(y)%64+1)*Absorption*(exp(alpha(x,WL(y))*0.001)-1.)
     /(WL(y)) + alpha(x,WL(y))*exp(alpha(x,WL(y))*0.001)) : 1.

Tfarest(x,y) = (x>0.01) ? alpha(x,WL(y))/(x*gamma_I(WL(y))*Farest*
     intensity(int(y)%64+1)*Absorption*(exp(alpha(x,WL(y))*0.001)-1.)
     /(WL(y)) + alpha(x,WL(y))*exp(alpha(x,WL(y))*0.001)) : 1.

Tsignal(x,y) = exp(-alpha(x,WL(y))*0.001)

chi(x,y) = (y<512) ? sqrt((chi3s+terms*gamma_R(WL(y))*x)**2+
     (terms*gamma_I(WL(y))*x)**2)/chi3s*sqrt(Tclosest(x,y)*
     Tfixed(x,y)*Tfarest(x,y)*Tsignal(x,y)) : Tfarest(x,y)


fit chi(x,y) file using 1:0:2:3 via RealKnot1, RealKnot2, RealKnot3,
     RealKnot4, RealKnot5, RealKnot6, RealKnot7, RealKnot8,
     RealKnot9, RealKnot10, RealKnot11, Absorption, ImagScale

set print "gamma_scan.txt"
do for [ i = 0:63] {
     print i*10+1050,gamma_R(i*10+1050),
     gamma_R(i*10+1050)*0.3,gamma_I(i*10+1050),
     gamma_I(i*10+1050)*0.3+10,Absorption*intensity(i+1)
```

```
}
unset print

set print "parameters.txt"
     print 1000, RealKnot1, RealKnot1_err
     print 1070, RealKnot2, RealKnot2_err
     print 1140, RealKnot3, RealKnot3_err
     print 1210, RealKnot4, RealKnot4_err
     print 1280, RealKnot5, RealKnot5_err
     print 1350, RealKnot6, RealKnot6_err
     print 1420, RealKnot7, RealKnot7_err
     print 1490, RealKnot8, RealKnot8_err
     print 1560, RealKnot9, RealKnot9_err
     print 1630, RealKnot10, RealKnot10_err
     print 1700, RealKnot11, RealKnot11_err
     print 1770, RealKnot12, RealKnot12_err
unset print

set grid

set title "ISO-4"
set xlabel "Wavelength (nm)"
plot [1050:1680][-50:140] gamma_R(x) lw 3 title "Real",
gamma_I(x) lw 3 title "Imaginary", 'parameters.txt'
using 1:2:3 with yerror title "Real Knots"
```

The `plots.sh` bash script to successively call `gamma_plot.sh` in order to plot cross-sections of the data at each wavelength point and compare with the fitted function.

```
#!/bin/bash

let "num = 2"
while read line;
do
#     python landscape.py $WL

     WL=$(echo "$line" | cut -d" " -f1)
     a=$(echo "$line" | cut -d" " -f2)
     a_err=$(echo "$line" | cut -d" " -f3)
```

```
     b=$(echo "$line" | cut -d" " -f4)
     b_err=$(echo "$line" | cut -d" " -f5)
     Absorption=$(echo "$line" | cut -d" " -f6)
     ./gamma_plot.sh $WL $a $a_err $b $b_err $num $Absorption
     let "num += 1"

#     bash contour.sh $WL $a $b

done < gamma_scan.txt

#convert -delay 20 -loop -0 plot*.gif animated_plots.gif
#convert -delay 20 -loop -0 *contour.gif animated_contour.gif
```

The gamma.sh script to create the individual plots, with the parameters as passed from the plots.sh file, containing the fits from gammaBez12.p, or gammaBez12F.p

```
#!/bin/sh
gnuplot << EOF

Closest = 0.02
Fixed = 0.30
Farest = 0.75

ns=1.42
f=(ns**2 + 2)/3
rho=1.3266
Na=6.022
M=600.75
chi3s=12
terms=10*f**4*rho*Na/M

A = exp(-($1-956.146)/155.41)+0.0854-0.036

alpha(x) = 2.303*A*x/(0.001*1.25)

Tclosest(x) = (x>0.01) ?
alpha(x)/(x*Closest*$4*$7*(exp(alpha(x)*0.001)-1.)/($1) +
alpha(x)*exp(alpha(x)*0.001)) : 1.

Tfixed(x) = (x>0.01) ?
```

```
alpha(x)/(x*Fixed*$4*$7*(exp(alpha(x)*0.001)-1.)/($1) +
alpha(x)*exp(alpha(x)*0.001)) : 1.

Tfarest(x) = (x>0.01) ?
alpha(x)/(x*Farest*$4*$7*(exp(alpha(x)*0.001)-1.)/($1) +
alpha(x)*exp(alpha(x)*0.001)) : 1.


Tsignal(x) = exp(-alpha(x)*0.001)

chi(x,y) = (y<1) ? sqrt((chi3s+terms*$2*x)**2+(terms*$4*x)**2)/chi3s*
     sqrt(Tclosest(x)*Tfixed(x)*Tfarest(x)*Tsignal(x)) : Tfarest(x)

unset key
set terminal gif
set output "plot$1.gif"
set border
set grid
set multiplot layout 3, 1

set lmargin 7
set tmargin 0.5
set bmargin 1
set bars
set xzeroaxis lt -1
set datafile separator whitespace
set arrow from $1,-50 to $1,140 nohead
set label "ISO-4 Jan 24, 2013" at 1500,80
set label "$1 nm" at 1400,-20
set label "Real: $2" at 1550, -15
set label "Imag: $4" at 1550, -35
unset xlabel
plot [1050:1700] [-50:140] 'gamma_scan.txt' using 1:2:3 axes x1y1
with errorbars, '' using 1:4:5 with errorbars,
'' using 1:2:3 smooth bezier

set bmargin 0
unset xtics
set ytics 0.0,1.0,2.0
set ylabel "Chi3/Chi3_DCM" offset 2
```

```
plot [0:1.5] [-0.5:2.5] 'DFWM.txt' using 1:$6,
     '' using 1:(\$$6-chi(\$1,0)) with impulse lw 3, chi(x,0)

set tmargin 0
set bmargin 2
set xtics
set ylabel "T"
plot [0:1.5] [-0.5:1.2] 'T.txt' using 1:$6,
     '' using 1:(\$$6-chi(\$1,1)) with impulse lw 3, chi(x,1)

EOF
```

The following is a script to fit a power dependence set of data, at 4 or 5 different intensities, and integrate the polarization wave to properly account for different intensities in each of the three incident beams.

```
file = 'power_data4.txt'

set key spacing 1.8

#Closest = 0.02
#Fixed = 0.30
#Farest = 0.75

Closest = 0.1
Fixed = 0.5
Farest = 0.75


distance = 10.0

set fit errorvariables
FIT_LIMIT = 1.e-9
set grid

ns=1.42
f=(ns**2 + 2)/3
rho=1.3266
Na=6.022
M=246.27
```

```
chi3s=12
terms=10*f**4*rho*Na/M

#intensity1 = 2.845
#intensity2 = 3.278
#intensity3 = 4.977
#intensity4 = 7.644
#intensity5 = 8.816

intensity1 = 4.537
intensity2 = 4.845
intensity3 = 8.19
intensity4 = 12.7
intensity5 = 21.4


Scaling = 0.004

# the function integral_f(z) approximates
# the integral of f(z) from 0 to z.
#
# the integral is calculated using Simpsons rule as
#          ( f(z-delta) + 4*f(z-delta/2) + f(z) )*delta/6
# repeated z/delta times (from z down to 0)
delta = 1.0

beta(x)=gamma_I*x*Scaling


############################################################
#intensity1
f1(x,z) = 1/sqrt(1+beta(x)*intensity1*Closest*z) *
1/sqrt(1+beta(x)*intensity1*Fixed*z) *
1/sqrt(1+beta(x)*intensity1*Farest*z)

f2(x,z) = 1/sqrt(1+beta(x)*intensity2*Closest*z) *
1/sqrt(1+beta(x)*intensity2*Fixed*z) *
1/sqrt(1+beta(x)*intensity2*Farest*z)

f3(x,z) = 1/sqrt(1+beta(x)*intensity3*Closest*z) *
```

```
1/sqrt(1+beta(x)*intensity3*Fixed*z) *
1/sqrt(1+beta(x)*intensity3*Farest*z)

f4(x,z) = 1/sqrt(1+beta(x)*intensity4*Closest*z) *
1/sqrt(1+beta(x)*intensity4*Fixed*z) *
1/sqrt(1+beta(x)*intensity4*Farest*z)

f5(x,z) = 1/sqrt(1+beta(x)*intensity5*Closest*z) *
1/sqrt(1+beta(x)*intensity5*Fixed*z) *
1/sqrt(1+beta(x)*intensity5*Farest*z)

############################################################
#integral_f1
integral_f1(x,z) = (z>0)?int1a(x,z,z/ceil(z/delta)):
-int1b(x,z,-z/ceil(-z/delta))
int1a(x,z,d) = (z<=d*.1) ? 0 :
(int1a(x,z-d,d)+(f1(x,z-d)+4*f1(x,z-d*.5)+f1(x,z))*d/6.)
int1b(x,z,d) = (z>=-d*.1) ? 0 :
(int1b(x,z+d,d)+(f1(x,z+d)+4*f1(x,z+d*.5)+f1(x,z))*d/6.)

integral_f2(x,z) = (z>0)?int2a(x,z,z/ceil(z/delta)):
-int2b(x,z,-z/ceil(-z/delta))
int2a(x,z,d) = (z<=d*.1) ? 0 :
(int2a(x,z-d,d)+(f2(x,z-d)+4*f2(x,z-d*.5)+f2(x,z))*d/6.)
int2b(x,z,d) = (z>=-d*.1) ? 0 :
(int2b(x,z+d,d)+(f2(x,z+d)+4*f2(x,z+d*.5)+f2(x,z))*d/6.)

integral_f3(x,z) = (z>0)?int3a(x,z,z/ceil(z/delta)):
-int3b(x,z,-z/ceil(-z/delta))
int3a(x,z,d) = (z<=d*.1) ? 0 :
(int3a(x,z-d,d)+(f3(x,z-d)+4*f3(x,z-d*.5)+f3(x,z))*d/6.)
int3b(x,z,d) = (z>=-d*.1) ? 0 :
(int3b(x,z+d,d)+(f3(x,z+d)+4*f3(x,z+d*.5)+f3(x,z))*d/6.)

integral_f4(x,z) = (z>0)?int4a(x,z,z/ceil(z/delta)):
-int4b(x,z,-z/ceil(-z/delta))
int4a(x,z,d) = (z<=d*.1) ? 0 :
(int4a(x,z-d,d)+(f4(x,z-d)+4*f4(x,z-d*.5)+f4(x,z))*d/6.)
int4b(x,z,d) = (z>=-d*.1) ? 0 :
(int4b(x,z+d,d)+(f4(x,z+d)+4*f4(x,z+d*.5)+f4(x,z))*d/6.)
```

```
integral_f5(x,z) = (z>0)?int5a(x,z,z/ceil(z/delta)):
-int5b(x,z,-z/ceil(-z/delta))
int5a(x,z,d) = (z<=d*.1) ? 0 :
(int5a(x,z-d,d)+(f5(x,z-d)+4*f5(x,z-d*.5)+f5(x,z))*d/6.)
int5b(x,z,d) = (z>=-d*.1) ? 0 :
(int5b(x,z+d,d)+(f5(x,z+d)+4*f5(x,z+d*.5)+f5(x,z))*d/6.)



Term(x,y) = (y<0.5) ? integral_f1(x,distance)/distance :
(y<1.5) ? integral_f2(x,distance)/distance :
(y<2.5) ? integral_f3(x,distance)/distance :
(y<3.5) ? integral_f4(x,distance)/distance :
(y<4.5) ? integral_f5(x,distance)/distance : 1.

chi(x,y) = (sqrt((chi3s+terms*gamma_R*x)**2+
(terms*gamma_I*x)**2)/chi3s)*Term(x,y)

gamma_R=-21.8
gamma_I=31.2

#fit chi(x,y) file using 1:-2:2:(1) via gamma_R,gamma_I,Scaling
fit [x=0.1:3.0] chi(x,y) file using 1:-2:2:3 via
intensity1, intensity2, intensity3,intensity4,
gamma_R, gamma_I

#, gamma_R, gamma_I

set key at 1, 3.5
set bars
set xzeroaxis lt -1
set xlabel "concentration"
set ylabel "Chi3/Chi3DCM"
#set label 1 file at 0.5, 3.2
set label 2 sprintf("Real = %2.1f ",gamma_R) at 1.55,0.8
set label 3 sprintf("Imag = %2.1f ",gamma_I) at 1.55,0.6
plot [0:2.5][0:3.5] '2.845.txt' using 1:2:3 axes x1y1
with errorbars title "Data 1" lt 7 linecolor rgb "red",
chi(x,0) lt 1 linecolor rgb "red" title
```

```
sprintf("%2.2f ",intensity1), '3.278.txt' using 1:2:3
axes x1y1 with errorbars title "Data 2" lt 7
linecolor rgb "blue", chi(x,1) lt 1 linecolor rgb "blue"
title sprintf("%2.2f ",intensity2), '4.977.txt' using 1:2:3
axes x1y1 with errorbars title "Data 3" lt 7
linecolor rgb "green", chi(x,2) lt 1 linecolor rgb "green"
title sprintf("%2.2f ",intensity3), '7.644.txt' using 1:2:3
axes x1y1 with errorbars title "Data 4", chi(x,3) lt 1
linecolor rgb "black" title sprintf("%2.2f ",intensity4)

set output "powerfit_3int4.png"
set terminal pngcairo size 640,480
replot

set output "powerfit_3int4.tex"
set terminal tikz size 4.5in,3.5in
replot

unset output
set terminal wxt
```

Bibliography

[1] Štefko, M. *et al.* Donor-acceptor (d-a)-substituted polyyne chromophores: Modulation of their optoelectronic properties by varying the length of the acetylene spacer. *Chemistry, a European Journal* tbd (to be published 2013).

[2] Frank, B. B. *et al.* Comparison of cc triple and double bonds as spacers in push-pull chromophores. *European Journal of Organic Chemistry* 4307–4317 (2011).

[3] Gubler, U. *et al.* Scaling law for second-order hyperpolarizability in poly(triacetylene) molecular wires. *Opt. Lett.* **24**, 1599–1601 (1999). URL `http://ol.osa.org/abstract.cfm?URI=ol-24-22-1599`.

[4] Slepkov, A. D., Hegmann, F. A., Eisler, S., Elliott, E. & Tykwinski, R. R. The surprising nonlinear optical properties of conjugated polyyne oligomers. *The Journal of Chemical Physics* **120**, 6807–6810 (2004). URL `http://link.aip.org/link/?JCP/120/6807/1`.

[5] Wu, X. *et al.* The use of femto-second lasers to trigger powerful explosions of gold nanorods to destroy cancer cells. *Biomaterials* 6157–62 (2013).

[6] Beels, M. T. *et al.* Compact tcbd based molecules and supramolecular assemblies for third-order nonlinear optics. *Optical Materials Express* **2**, 294 – 303 (2012).

[7] Armstrong, J., Bloembergen, N., Ducuing, J. & Pershan, P. Interactions between light waves in a nonlinear dielectric. *Physical Review* **127**, 1918 (1962).

[8] Orr, B. & Ward, J. Perturbation theory of the non-linear optical polarization of an isolated system. *Molecular Physics* **20**, 513–526 (1971).

[9] Andrews, S. Using rotational averaging to calculate the bulk response of isotropic and anisotropic samples from molecular parameters. *J. Chem. Ed.* **8**, 509–514 (2004).

[10] Peréz-Moreno, J., Clays, K. & Kuzyk, M. G. A new dipole-free sum-over-states expression for the second hyperpolarizability. *The Journal of Chemical Physics* **128** (2008).

[11] Kuzyk, M. G. Fundamental limits of all nonlinear-optical phenomena that are representable by a second-order nonlinear susceptibility. *The Journal of Chemical Physics* **125**, 154108 (2006). URL `http://link.aip.org/link/?JCP/125/154108/1`.

[12] Champagne, B. & Kirtman, B. Comment on "physical limits on electronic nonlinear molecular susceptibilities". *Phys. Rev. Lett.* **95**, 109401 (2005). URL `http://link.aps.org/doi/10.1103/PhysRevLett.95.109401`.

[13] Kuzyk, M. G. Kuzyk replies:. *Phys. Rev. Lett.* **95**, 109402 (2005). URL `http://link.aps.org/doi/10.1103/PhysRevLett.95.109402`.

[14] Kuzyk, M. Fundamental limits on third-order molecular susceptibilities. *Opt. Lett.* **25**, 1183–1185 (2000). URL `http://ol.osa.org/abstract.cfm?URI=ol-25-16-1183`.

[15] Kuzyk, M. G. Fundamental limits on two-photon absorption cross sections. *The Journal of Chemical Physics* **119**, 8327–8334 (2003).

[16] Franken, P. A., Hill, A. E., Peters, C. W. & Weinreich, G. Generation of optical harmonics. *Phys. Rev. Lett.* **7**, 118–119 (1961). URL `http://link.aps.org/doi/10.1103/PhysRevLett.7.118`.

[17] Sheik-Bahae, M., Said, A. A., Wei, T.-H., Hagan, D. J. & Van Stryland, E. W. Sensitive measurement of optical nonlinearities using a single beam. *Quantum Electronics, IEEE Journal of* **26**, 760–769 (1990).

[18] Gubler, U. & Bosshard, C. Optical third-harmonic generation of fused silica in gas atmosphere: Absolute value of the third-order nonlinear optical susceptibility $\chi^{(3)}$. *Phys. Rev. B* **61**, 10702–10710 (2000). URL `http://link.aps.org/doi/10.1103/PhysRevB.61.10702`.

[19] Milam, D. Review and assessment of measured values of the nonlinear refractive-index coefficient of fused silica. *Appl. Opt.* **37**, 546–550 (1998). URL `http://ao.osa.org/abstract.cfm?URI=ao-37-3-546`.

[20] Santran, S., Canioni, L., Sarger, L., Cardinal, T. & Fargin, E. Precise and absolute measurements of the complex third-order optical susceptibility. *J. Opt. Soc. Am. B* **21**, 2180–2190 (2004). URL `http://josab.osa.org/abstract.cfm?URI=josab-21-12-2180`.

[21] Strohkendl, F. P., Dalton, L. R., Hellwarth, R. W., Sarkas, H. W. & Kafafi, Z. H. Phase-mismatched degenerate four-wave mixing: complex third-order susceptibility tensor elements of c60 at 768 nm. *J. Opt. Soc. Am. B* **14**, 92–98 (1997). URL `http://josab.osa.org/abstract.cfm?URI=josab-14-1-92`.

[22] May, J. C. *Origin of the Highly Efficient Third-Order Optical Response in Small Organic Molecules*. Ph.D. thesis, Lehigh University (2007). UMI 3285759.

[23] Kim, O.-K. *et al.* New class of two-photon-absorbing chromophores based on dithienothiophene. *Chemistry of Materials* **12**, 284–286 (2000). URL `http://pubs.acs.org/doi/abs/10.1021/cm990662r`.

[24] May, J. C. *et al.* Highly efficient third-order optical nonlinearities in donor-substituted cyanoethynylethene molecules. *Optics Letters* **30**, 3057 – 3059 (2005).

[25] Zhou, J. & Kuzyk*, M. G. Intrinsic hyperpolarizabilities as a figure of merit for electro-optic molecules. *The Journal of Physical Chemistry C* **112**, 7978–7982 (2008). URL http://pubs.acs.org/doi/abs/10.1021/jp7120824.

[26] Kato, S. *et al.* Homoconjugated pushpull and spiro systems: Intramolecular charge-transfer interactions and third-order optical nonlinearities. *Angewandte Chemie International Edition* **49**, 6207–6211 (2010). URL http://dx.doi.org/10.1002/anie.201002236.

[27] Chiu, M. *et al.* N,n'-dicyanoquinone diimide-derived donor-acceptor chromophores: Conformational analaysis and optoelectronic properties. *Organic Letters* **14**, 54 – 57 (2012).

[28] Tancini, F. *et al.* 1,1-dicyano-4-[4-(diethylamino)phenyl]buta-1,3-dienes: Structureproperty relationships. *European Journal of Organic Chemistry* **2012**, 2756–2765 (2012). URL http://dx.doi.org/10.1002/ejoc.201200111.

[29] Fleischman, M. S. *Small Molecule Assemblies for Third-Order Nonlinear Optics*. Ph.D. thesis, Lehigh University (2010). UMI 3439729.

[30] May, J. C., Biaggio, I., Bures, F. & Diederich, F. Extended conjugation and donor-acceptor substitution to improve the third-order optical nonlinearity of small molecules. *App. Phy. Lett.* **90**, 509–514 (2007).

[31] La Porta, P. R. *On the Third Order Optical Non-linearities of Small Organic Molecules: Investigation, Analysis and Optimization*. Ph.D. thesis, Lehigh University (2011).

[32] Thienpont, H., Rikken, G. L. J. A., Meijer, E. W., ten Hoeve, W. & Wynberg, H. Saturation of the hyperpolarizability of oligothiophenes. *Phys. Rev. Lett.* **65**, 2141–2144 (1990). URL http://link.aps.org/doi/10.1103/PhysRevLett.65.2141.

[33] Lewis, G. N. & Calvin, M. The color of organic substances. *Chemical Reviews* **25**, 273–328 (1939). URL `http://pubs.acs.org/doi/abs/10.1021/cr60081a004`.

[34] Mathy, A. *et al.* Third-harmonic-generation spectroscopy of poly(*p* -phenylenevinylene): A comparison with oligomers and scaling laws for conjugated polymers. *Phys. Rev. B* **53**, 4367–4376 (1996). URL `http://link.aps.org/doi/10.1103/PhysRevB.53.4367`.

[35] Hamada, T. An ab initio molecular orbital study on hyperpolarizabilities of an interacting 2-methyl-4-nitroaniline molecular pair: A molecular study on the oriented-gas approximation. *Journal of Physical Chemistry* 8777–8781 (1996).

[36] Schmidt, M. *et al.* General atomic and molecular electronic structure system. *Journal of Computational Chemistry* **14**, 1347–1363 (1993).

[37] Gordon, M. & Schmidt, M. *Advances in Electronic Structure Theory: GAMESS a Decade Later.* (Elsevier, Amsterdam, 2005).

[38] Moonen, N. N. *Cyanoethynylethenes: A Powerful Class of Modules for Acetylenic Scaffolding and Formation of Novel Charge-Transfer Chromophores.* Ph.D. thesis, Swiss Federal Institute of Technology Zürich (2004). No. 15468.

[39] Avogadro: an open-source molecular builder and visualization tool. version 1.0.3 http://avogadro.openmolecules.net/.

[40] Hanwell, M. D. *et al.* Avogadro: An advanced semantic chemical editor, visualization, and analysis platform. *Journal of Cheminformatics* **4** (2012).

[41] Maroulis, G. Ab initio determination of the electric multipole moments and static (hyper)polarizability of hccx, x = f, cl, br, and i. *Journal of Computational Chemistry* **2003**, 443–452 (2003).

[42] Vila, F. D. *et al.* Basis set effects on the hyperpolarizability of $chcl_3$: Gaussian-type orbitals, numerical basis sets and real-space grids. *arXiv* (2010).

[43] Pluta, T. & Sadlej, A. J. Hypol basis set for high-level-correlated calculations of electric dipole hyperpolarizabilities. *Chemical Physics Letters* 391–401 (1998).

[44] Esembeson, B., Scimeca, M. L., Biaggio, I., Michinobu, T. & Diederich, F. A high optical quality supramolecular assembly for third-order integrated nonlinear optics. *Adv. Mater.* **19**, 4584–4587 (2008).

[45] Michinobu, T. *et al.* A new class of organic donor–acceptor molecules with large third-order optical nonlinearities. *Chem. Commun.* 737–739 (2005).

[46] Michinobu, T. *et al.* Donor-substituted 1,1,4,4-tetracyanobutadienes (tcbds): New chromophores with efficient intramolecular charge-transfer interactions by atom-economic synthesis. *Chem. Eur. J.* **12**, 1889 (2005).

[47] Kivala, M. & Diederich, F. Acetylene-derived strong organic acceptors for planar and nonplanar push-pull chromophores. *Acc. Chem: Res.* **42**, 235–248 (2009).

[48] Koos, C. *et al.* All-optical high-speed signal processing with silicon-organic hybrid slot waveguides. *Nat. Photonics* **3**, 216–219 (2009).

[49] Leuthold, J. *et al.* Silicon organic hybrid technology - a platform for practical nonlinear optics. *Proc. IEEE* **97**, 1304–1316 (2009).

[50] Vallaitis, T. *et al.* Optical properties of highly nonlinear silicon-organic hybrid (soh) waveguide geometries. *Opt. Express* **17**, 17357–17368 (2009). URL `http://www.opticsexpress.org/abstract.cfm?URI=oe-17-20-17357`.

[51] Leuthold, J. *et al.* All-optical fft signal processing of a 10.8 tb/s single channel ofdm signal. *Integrated Photonics Research / Photonics in Switching* (2010).

[52] Vallaitis, T. *et al.* All-optical wavelength conversion of 56 gbit/s nrz-dqpsk signals in silicon-organic hybrid strip waveguides. *Optical Fiber Communication Conference* (2009).

[53] Freude, W. *et al.* Ultrafast silicon-organic hybrid (soh) photonics. In *Conference on Lasers and Electro-Optics*, CThR1 (Optical Society of America, 2010). URL `http://www.opticsinfobase.org/abstract.cfm?URI=CLEO-2010-CThR1`.

Acknowledgements

Special thanks to Professor Biaggio, for his vibrant explanations, interesting discussions, and his willingness to listen.

Thanks to Professor Diederich and the entire organic chemistry group at ETH Zürich for their very fruitful work in this collaboration. A special mention to Dr. Tzirakis for his attention to detail, help in identifying acidity issues in our solvents, and finding an effective solution which made this study possible.

Also, many thanks to Lois and Pam for keeping everything running smoothly.

Thanks to Rich and Wayne for helping me out with the necessary hardware, and digging up those essential pieces.

Thanks to Joe for taking the time to teach me some of the art and science of metal work on the lathe. I hope to be able to make some new turnings in the future.

I appreciate the support and helpful ideas from my committee members.

Thanks to Professor Hickman for his time and input in helping me setup some of the computational chemistry.

I must mention Lamprey Cycling for providing a competitive outlet, helping me keep my sanity, and Lehigh Cycling for sending me to numerous collegiate events.

Vita

Marten Beels
Email: mbeels@fastmail.us

Education PhD in Physics, Lehigh University 2008-2013

Thesis Title: Optimization of Donor-Acceptor Substitution for Large Optical Non-linearities in Small Organic Molecules

Brief Synopsis of Research: Using degenerate four-wave mixing, I am able to determine the wavelength dependence of the real and imaginary parts of the third-order polarizability. This experimental method allows for the spectroscopy of the first two-photon absorption resonance, observation of resonant-enhancement, and estimation of the zero-frequency limit. The experimental results are compared with fundamental limits, and several figure of merits are calculated to assess a molecule's potential for applications, and quantifying the efficiency by which the molecular parameters such as the number of polarizable π-electrons are utilized. Additional computational chemistry, and analysis of the quantum SoS expression support the experimental data and analsysis.

Research Interests: Linear and non-linear optics, spectroscopy, laser research. Developing physical models, and better tools for data analysis.

Awards

GAANN Fellow 2008-2009
Sherman Fairchild Fellowship in Solid State Studies 2011-2013
Yoshida Award 2011

Publications

S. Kato, M.T.R. Beels, P. La Porta, W. B. Schweizer, C. Boudon, J.-P. Gisselbrecht, I. Biaggio, F. Diederich *Homoconjugated Push-Pull and Spiro Systems: Intramolecular Charge-Transfer Interactions and Third-Order Optical Non-linearities.* Angew. Chem. Int. Ed. 49, 6207-6211 (2010)

M. Chiu, B. Juan, M.T.R. Beels, I. Biaggio, J.-P. Gisselbrecht, C. Boudon, W.B. Schweizer, M. Kivala, F. Diederich *N,N'Dicyanoquinone Diimide-Derived Donor-Acceptor Chromophores: Conformational Analysis and Optoelectronic Properties.* Organic Letters 14(1), 54-57 (2012)

F. Tancini, Yi-Lin Wu, W.B. Schweizer, J.-P. Gisselbrecht, C. Boudon, P.D. Jarawowski, M.T. Beels, I. Biaggio, F. Diederich *1,1-Dicyano-4-[4-(diethylamino)phenyl]buta-1,3-dienes: Structure-Property Relationships* European Journal of Organic Chemistry 2756-2765 (2012)

M.T. Beels, M.S. Fleischman, I. Biaggio, B. Breiten, M. Jordan, F. Diederich *Compact TCBD Based Molecules and Supramolecular Assemblies for Third-Order Nonlinear Optics* Optics Materials Express, Vol 2(3), 294-303 (2012)

M. Štefko, M.D. Tzirakis, B. Breiten, M.O. Ebert, O. Dumele, W.B. Schweizer, J.-P. Gisselbrecht, C. Boudon, M.T. Beels, I. Biaggio, F. Diederich *Donor-Acceptor (D-A)-Substituted Polyyne Chromophores: Modulation of their Optoelectronic Properties by Varying the Length of the Acetylene Spacer* Chemistry - A European Journal (accepted)

M.T. Beels, I. Biaggio *Spectroscopy of the First Two-photon Transition in Highly Efficient, Donor-Substituted Organic Molecules* (in progress)

M.T. Beels, I. Biaggio *The Effect of the Size of the Conjugated System on Third-order Nonlinear Optical Properties: A Systematic Study* (in progress)

Presentations

American Institute of Physics (AIP) - Oral session at 2012 March Meeting "A new Series of Donor-Acceptor Substituted Small Organic Molecules with Large Third Order Molecular Polarizability"

Optical Society of American (OSA) - Presented student talk "Non-linear Spectroscopy"

Employment

2007 - 2008 Mauell Corporation: Dillsburg, PA
2006 - 2007 Tyco Electronics, M/A-Com: Harrisburg, PA
2005 Grove School: Madison, CT

Skills

Computer:

LabView, C/C++ programming, bash scripting, data analysis, and non-linear curve fitting

Computational Chemistry using GAMESS

Experimental Lab:

Experience with maintaining and re-aligning pulsed laser systems (Clark-MXR) and optical parametric amplifier systems (Light Conversions TOPAS).

Laboratory equipment such as oscilloscopes, box-car integrators, GPIB computer interfaces, and spectrophotometers.

Using various optical detectors in the visible and IR (Si, InGaAs, Hg, etc), as well as data collection using boxcars, computer interfaces, spectrophotometers, and photo-multiplier tubes.

Molecular beam vapor deposition to create organic thin films of high optical quality in a vacuum, with in-situ control of applied electric fields and substrate temperature.